Modelling dike breach formation due to headcut erosion

Defining the residual strength of dikes during overflow

B. Verbeek

TU Delft

Modelling dike breach formation due to headcut erosion

Defining the residual strength of dikes during overflow

by

Bram Verbeek

to obtain the degree of Master of Science

at the Delft University of Technology,

to be presented publicly on Wednesday November 27th, 2019 at 3:30 PM.

Student ID:	4285719	
Project duration:	February – November, 2019	
Thesis committee:	Prof. dr. ir. S. N. Jonkman,	TU Delft
	Dr. ir. M. van Damme,	TU Delft
	Dr. ir. W. Broere,	TU Delft
	Dr. ir. R. Bisschop,	Arcadis Nederland
	Ir. P. Goessen,	Hoogheemraadschap Hollands Noorderkwartier

Cover photo: Oil painting by Jan Asselijn (ca. 1610-1652), "De doorbraak van de Sint-Anthonisdijk bij Amsterdam", 1651. Photo made available by the Rijksmuseum.

Preface

Before you lies the MSc Thesis "Modelling dike breach formation", which presents the Breach Resistance Analysis Model. This mathematical model calculates the time-to-failure of a dike and is used to assess whether a dike will breach in given overflow conditions or to design a dike to withstand certain conditions. This thesis has been written as a final fulfilment of the graduation requirements of the Master of Science in Civil Engineering of Delft University of Technology (in the track Hydraulic Engineering, specialising in Flood Risk, accompanied by the Integral Design and Management annotation). I was engaged in researching and writing this Thesis from February to November 2019.

The work done to answer the research question was predominantly undertaken at the Rotterdam office of Arcadis Nederland, while the geotechnical lab work was performed at the faculty of Civil Engineering and Geosciences at Delft University of Technology. The research question was formulated in cooperation with my two daily supervisors: Dr. Ir. M. van Damme, who works as a postdoctoral researcher at Delft University of Technology and Dr. Ir. F. Bisschop, a senior geotechnical specialist at Arcadis Nederland. I would like to express my gratitude for their feedback and guidance, which was of great importance to the success of my project.

Furthermore, my thanks go out to Prof. Dr. Ir. S.N. Jonkman and Dr. Ir. W. Broere at Delft University of Technology, whose feedback along the way helped me to not only focus on the theoretical aspects of the project, but also to keep the practical applicability of my findings in mind. The final member of my graduation committee was Ir. P. Goessen, currently occupied as an advisor flood protections at the Water Board Hollands Noorderkwartier. She shared many insights on the management of flood protections and was always able to find interested colleagues to do the same. Her input was greatly appreciated.

In my fulfilment of the graduation guidelines of the Integral Design and Management annotation (preparing students for work in multi-disciplinary projects), I was guided by Dr. Ir. G.A. van Nederveen, whom I would like to thank for feedback on my process and design method during this project. While gathering data on case studies to assess the performance of the model, numerous people, working at various Water Boards throughout the Netherlands came to my aid. Their interest and help was both inspiring and very helpful, and I would like to thank them all. My time working on this MSc Thesis would not have been the same without all the colleagues and graduate students at Arcadis Rotterdam. Thanks for making each day of this project more fun.

A special word of thanks goes to my friends and family, specifically my parents, who were my greatest support during this project and my entire education. You are the best and I would not have come to this point without you.

At the end, thanks to you, reader. If you are reading this line after the others, you at least read one page of my thesis. I hope you find the remaining pages worth your while as well.

Bram Verbeek
Rotterdam, November 2019

Abstract

Dikes constructed of a sand core, clay cover and natural vegetation as (landside) slope protection are common flood defence structures in the Netherlands. The design parameters, such as the crest height of dikes, are determined through risk assessment to reduce the remaining probability of a failure mechanism, such as overflow. Little is known about the exact process leading to failure of the typical Dutch dikes in case the failure conditions actually occur. The most notable floods in the Netherlands have all been caused by dike breaching, where local damage in the dike lead to breach formation.

This research describes the process of breach formation due to overflow and determines what design parameters affect the resistance of a dike against breaching. The proposed model (BRAM, a Breach Resistance Analysis Model) combines existing methods to determine the time-to-failure of the grass and clay cover with a newly developed process-oriented headcut erosion model. The model assesses the total time-to-failure of a dike through sequential failure of its components. The following process is simulated.

Overflow over a dike causes a turbulent flow along the landside slope, resulting in local damage to the grass cover on either a prescribed weak spot or slope transition. The clay cover is subsequently eroded and the granular core material becomes exposed to the flow. A key assumption in the applied method lies in the fact that every newly exposed layer is less resistant to erosion than the layer above, resulting in slope steepening. Therefore, a near-vertical cliff, referred to as a headcut, is formed. When the overflowing water no longer follows the profile of the steep slope, a cascading flow, resembling a waterfall, forms a scour pit.

The turbulent flow in this scour pit also erodes the core material of the dike, allowing horizontal erosion to undercut the slope. The undercutting of the slope causes the headcut to tumble over, moving the headcut and jet impact point to move towards the waterside slope, essentially restarting the scour process. This iterative process continues until the invert height of the dike is lowered to zero and the overflow rate is increased further.

Model validation shows good agreement with test results on both large and small scale, as long as the assumptions regarding the structure of the dike hold (a dike profile consisting of a granular core under a clay layer and grass cover).

When applied to three case studies, the BRAM-model predicts a similar total time-to-failure as the most advanced current model, posed by d'Eliso (2007). The predicted time-to-failure for the grass cover shows a significant difference. The BRAM-model predicts the grass cover to fail significantly faster than the model by d'Eliso (2007). This difference is offset by a longer predicted time-to-failure of the clay cover. Finally, the proposed model predicts a 50% slower headcut migration rate, as compared to the results by D'Eliso. This is a result of the more advanced description of the headcut erosion process. As the time-to-failure of the headcut migration phase is relatively short compared to the total breach formation process (between 10% and 25%), the total predicted time-to-failure is quite similar between both models.

The main advantage of the BRAM-model is its suitability for design testing. The main weakness remains the unpredictable location of headcut initiation, which depends too strongly on spatial variation of the resistance of the dike to be predicted accurately, based on available data.

Design parameters to increase the time-to-breaching have been identified. The most relevant were the steepness of the dike slope and thickness of the clay cover. Sensitivity analysis showed that the steepness and thickness of the clay cover, but also the porosity of the core material can be adapted to increase the time-to-failure of a dike. A breach-resistant dike may be designed for a limited overflow duration. Case studies showed three test dikes to sustain an overflow rate of 100 l/m/s for various hours by the grass and clay cover. As soon as the core material becomes exposed, the breach formation process accelerates significantly. The exact duration depends on the profile and construction material of the dike.

Samenvatting

Dijken opgebouwd uit een kern van zand met daarop een klei- en grasbekleding als bescherming van het talud (aan de landzijde) zijn een veelgebruikte waterkering in Nederland. De ontwerpparameters van deze dijken, zoals de kruinhoogte, worden bepaald door middel van probabilistische ontwerpmethoden. Hiermee wordt de kans op een faalmechanisme, zoals overloop, tot een normwaarde gereduceerd. Er is echter weinig bekend over de processen die leiden tot het falen van deze dijkopbouw, wanneer de ontwerpbelasting optreedt. De grootste overstromingen in Nederland zijn veroorzaakt door dijkdoorbraken.

Dit onderzoek beschrijft bresvorming als gevolg van overloop en bepaalt welke ontwerpparameters de weerstand van een dijk tegen bresvorming beïnvloeden. Het model (BRAM, "a Breach Resistance Analysis Model") combineert bestaande methoden om de duur van het faalproces van de gras- en kleibekleding te bepalen met een nieuw model op basis van kliferosie. Het model berekent de totale duur van de bresvorming aan de hand van de tijd-tot-falen per onderdeel van de dijk. Het gemodelleerde proces kan als volgt worden beschreven.

Overloop over de dijk resulteert in een turbulente stroming langs het talud aan de landzijde, waardoor de grasbekleding lokale schade oploopt op een zwakke plek of op een overgang in het talud. De kleibekleding erodeert en de zandkern wordt blootgesteld aan de stroming. Een belangrijke aanname in de toegepaste methode is dat iedere laag die blootgelegd wordt, erosiegevoeliger is dan de bovenliggende laag, waardoor de taludhelling ter plaatse van de schade steiler wordt.

Wanneer een (bijna) verticale klif is ontstaan, kan de stroming het talud niet meer volgen en ontstaat er een stromingsprofiel dat lijkt op een kleine waterval. Hierdoor onstaat een ontgrondingskuil, waardoor de klif wordt ondergraven. Door de erosie onder de klif verliest deze zijn stabiliteit. Het kliferosieproces verschuift naar de boezemzijde en wordt herstart. Dit iterative proces herhaalt zich totdat de kerende hoogte van de dijk door dit proces tot wordt gereduceerd tot nul en het overloopdebiet toeneemt.

Het model is per fase gevalideerd tegen proeven op dijken met de aangenomen opbouw (een kern van zand onder een klei- en grasbekleding). De voorspellingen van het BRAM-model zijn in vergeleken met het model van D'Eliso, het enige vergelijkbare bresvormingsmodel dat toepasbaar is op heterogene dijkprofielen.

De voorspellingen van de totale duur van het bresvormingsproces door het BRAM-model komen gedeeltelijk overeen met de voorspellingen van het model van d'Eliso (2007). De duur van het faalproces van de grasbekleding wordt significant lager ingeschat. Dit wordt deels gecompenseerd door een hogere schatting van de duur van het faalproces van de kleilaag. Het ontwikkelde model voorspelt tenslotte een 50% langere duur van het kliferosieproces, vergeleken bij het model van D'Eliso. Dit is een gevolg van de verbeterde beschrijving van het kliferosieproces. Aangezien de duur van het kliferosieproces relatief kort is ten opzichte van de totale duur van de bresvorming in de dijk (tussen de 10% en 25%), blijft de voorspelling van de totale duur van het bresvormingsproces vergelijkbaar tussen de twee modellen.

De grootste zwakte ligt in het voorschrijven van de locatie voor de klifvorming. Deze locatie hangt in werkelijkheid sterk af van ruimtelijke variatie van de weerstand van de dijk om dit accuraat te kunnen voorspellen op basis van proefwaarden. Het voornaamste voordeel van het BRAM-model is de toepasbaarheid voor ontwerp.

Uit het model volgen ontwerpparameters om de duur van het bresvormingsproces te vergroten. De meest invloedrijke parameters zijn de steilheid van het binnentalud en de dikte van de kleibekleding. Een gevoeligheidsanalyse van het model toonde aan dat deze parameters, maar ook de porositeit van het materiaal in de kern kunnen worden aangepast om de duur van het bresvormingsproces te vergroten. Een bresbestendige dijk kan worden ontworpen, als de duur van overloop beperkt blijft. Uit de case studies blijkt voor drie testdijken dat een overloopdebiet (per eenheid van breedte) van 100 l/m/s voor enkele uren kan worden weerstaan door de gras- en kleibekleding. Zodra het kernmateriaal blootligt, versnelt het erosieproces aanzienlijk. De exacte duur van bresvorming hangt af van het profiel en de materialen waarin de dijk is opgebouwd.

Contents

List of Symbols

Roman symbols

A	Cross-sectional area of the flow	$[m^2]$
A_p	Surface area of the polder behind a dike	$[m^2]$
A_{shear}	Area of contributing shear surface in shear test sample	$[m^2]$
$\overline{B}$	Average ultimate breach width	$[m]$
b_4	Failure mode coefficient Zhang et al. (2009) model	$[-]$
b_5	Erodibility coefficient Zhang et al. (2009) model	$[-]$
c	Boundary displacement velocity	$[ms^{-1}]$
C	Chézy coefficient	$[m^{1/2}s^{-1}]$
C_1	Vertical flow contraction coefficient	$[-]$
C_2	Horizontal flow contraction coefficient	$[-]$
C_3	Empirical coefficient Zhang et al. (2009) model	$[-]$
C_4	Empirical coefficient Zhang et al. (2009) model	$[-]$
C_5	Empirical coefficient Zhang et al. (2009) model	$[-]$
C_5	Empirical coefficient Zhang et al. (2009) model	$[-]$
c_b	Near-bed sediment concentration	$[kgm^{-3}]$
$C_{\%}$	Clay fraction of the soil	$[-]$
C_c	Cohesion of the clay cover	$[kN/m^2]$
C_d	Weir discharge coefficient	$[-]$
C_f	Friction coefficient	$[-]$
C_g	Grass cover factor	$[-]$
C_h	Headcut coefficient	$[s^{-2/3}]$

C_j	Jet dissipation coefficient	$[-]$
C_l	Lutum fraction	$[-]$
C_{ur}	Unloading-reloading coefficient	$[m^2 s^{-1}]$
C_v	Vertical consolidation coefficient	$[m^2 s^{-1}]$
$C_{v,sw}$	Swell coefficient	$[m^2 s^{-1}]$
d	Depth of flow	$[m]$
D	Grain diameter	$[m]$
D_{10}	10th percentile grain size	$[m]$
D_{50}	Median grain size	$[m]$
D_{50}	Median grain size of sand (core material)	$[m]$
D_{60}	60th percentile grain size	$[m]$
d	Water depth	$[m]$
d_g	Water depth on landside ground level	$[m]$
d_i	Water depth on the landside slope	$[m]$
d_n	Normal depth of flow	$[m]$
D_n	Diameter of impinging jet	$[m]$
dt	Time step of the model	$[s]$
e	Euler's number (2.718)	$[-]$
E	Erosion rate	$[kgm^{-2}s^{-1}]$
ΔE	Dissipated energy of the flow expressed as a height	$[m]$
f	Non-dimensional friction loss	$[-]$
FOS	Factor of safety of headcut stability	$[-]$
Fr	Froude number	$[-]$
Fr_n	Froude number in normal flow	$[-]$
F_{shear}	Shear force	$[N]$
g	Gravitational acceleration	$[ms^{-2}]$

ΔH	Energy head level difference	$[m]$
h_0	Head level on the dike crest	$[m]$
h_b	Final height of the breach	$[m]$
h_{cd}	Height of the dike crest with respect to its base	$[m]$
h_g	Head level on landside ground level	$[m]$
H_h	Headcut height	$[m]$
$H_{h,i}$	Initial headcut height	$[m]$
h_i	Head level on the landside slope	$[m]$
h_{nozzle}	Height of jet nozzle above material	$[m]$
h_r	Reference height of 15 metres used as boundary height between large and small dams	$[m]$
h_s	Depth of sheared soil wedge	$[m]$
h_w	Head level in the bosom	$[m]$
I_b	Bed level gradient)	$[-]$
I_c	Consistency index of soil)	[%]
I_p	Plasticity index of soil)	[%]
J	Energy slope	$[-]$
K	Normal pressure in scour pit due to jet flow	variable
k_e	Erodibility coefficient	variable
k_H	Embankment height factor	$[-]$
k_l	Empirical coefficient by Schuttrumpf and Oumeraci (2005)	$[-]$
k_{sat}	Hydraulic conductivity by Schuttrumpf and Oumeraci (2005)	$[ms^{-1}]$
k_0	Variable coefficient dependant on failure mode	$[-]$
L	Representative length scale	$[m]$
l_d	Drainage path length	$[m]$
l_j	Length of slip plane segment	$[m]$
L_l	Liquid limit of soil	[%]

l_n	Along-slope length until normal flow depth	$[m]$
L_p	Plastic limit of soil	[%]
L_s	Sward length of the grass cover	$[m]$
L_w	Horizontal length of a weir	$[m]$
n	Manning's coefficient	$[sm^{-1/3}]$
n_c	Manning's coefficient of clay cover	$[sm^{-1/3}]$
n_{tot}	Total Manning's coefficient (of the cover)	$[sm^{-1/3}]$
N_{bishop}	Number of iterations applied to Bishop stability criterion	[-]
$N_{bisschop}$	Number of iterations applied to Bisschop erosion formula	[-]
$N_{profile}$	Number of points modelled as the surface of the dike profile	[-]
$N_{scourpit}$	Number of horizontally equidistant grid points in which the scour pit is modelled	[-]
$N_{slipangles}$	Number of different angles tested to determine normative slip plane	[-]
N_{stab}	Number of iterations applied to Riteco stabilising criterion	[-]
$N_{undercut}$	Number of grid points along the undercut at which the erosion is calculated	[-]
P	Wetted perimeter	$[m]$
q	Specific discharge over the dike	$[m^2 s^{-1}]$
q_{avg}	Time-averaged specific discharge past the dike	$[m^2 s^{-1}]$
q_{max}	Maximum specific discharge past the dike	$[m^2 s^{-1}]$
q_{var}	Time-varying specific discharge past the dike	$[m^2 s^{-1}]$
Q_p	Peak flow rate through breach	$[m^3 s^{-1}]$
Q_w	Flow rate through a weir	$[m^3 s^{-1}]$
r	Radial distance coordinate from jet axis	$[m]$
R	Hydraulic radius	$[m]$
R_b	Hydraulic radius of a breach	$[m]$
R_f	Resisting force	$[N]$
s	Coordinate along jet axis	$[m]$

s_s	Coordinate along landside slope	$[m]$
S_f	Solliciting force	$[N]$
S_u	Undrained shear strength	$[Pa]$
T	Total time during which overflow has been present	$[h]$
t_{50}	Time until 50% of settlement	$[s]$
T_b	Mean bursting period	$[s]$
t_f	Time to breach formation	$[s]$
t_{gf}	Time-to-failure of the grass cover	$[s]$
t_r	Unit duration of 1 hr, as described in Froehlich (2016a)	$[h]$
t_{stab}	Scour steps performed between scour pit stabilisations (computational parameter)	[-]
u	velocity of the flow along the boundary	$[ms^{-1}]$
$\overline{u}$	Representative mean flow velocity	$[ms^{-1}]$
u_*	Shear velocity	$[ms^{-1}]$
u_0	Mean flow velocity at the dike crest	$[ms^{-1}]$
u_c	Flow velocity at critical flow	$[ms^{-1}]$
u_g	Flow velocity at failure of the grass cover	$[ms^{-1}]$
u_i	Depth-averaged flow velocity on a point the landside slope	$[ms^{-1}]$
v_e	Erosion velocity	$[ms^{-1}]$
v_s	Shear displacement velocity	$[ms^{-1}]$
v_{e1}	First estimate of erosion velocity	$[ms^{-1}]$
V_s	Volume of water	$[m^3]$
V_w	Volume of water retained by dam	$[m^3]$
$\overline{W}$	Average embankment width	$[m^3]$
W_c	Volumetric water content	$[-]$
W_g	Gravimetric water content	$[-]$
$W_{g,i}$	In-situ gravimetric water content	$[-]$

W_j	Weight slip section	$[-]$
dX	Horizontal headcut migration	$[m]$
x	Horizontal coordinate across dike body	$[m]$
X	Arbitrary example parameter	$[-]$
y	Horizontal coordinate along dike body	$[y]$
z	Vertical coordinate	$[m]$
z_g	Height of ground level with respect to a reference	$[m]$
z_{br}	Bottom level of breach	$[m]$

Greek symbols

α	Bed slope angle in scour pit	$[°]$
β	landside slope steepness	$[-]$
$\beta_{1,2}$	Curvature (slope angle change) of scour pit sections	$[°]$
Δ	Specific gravity	$[-]$
ϵ	Height to width ratio of a weir	$[-]$
ζ	Exponent in erosion equations	$[-]$
η	Porosity	$[-]$
η_c	Porosity clay	$[-]$
η_s	Porosity core material	$[-]$
η_0	In-situ porosity	$[-]$
η_l	Maximum porosity	$[-]$
λ_a	Adaptation length of flow (along slope)	$[m]$
ν	Dynamic viscosity of the flow	$[Nsm^{-2}]$
ξ_c	Pèclet number	$[-]$
ρ_d	Dry density of soil	$[kgm^{-3}]$
ρ_c	Bulk density of clay	$[kgm^{-3}]$
ρ_s	Granular density of sand	$[kgm^{-3}]$

ρ_{sand}	Bulk density of sand	$[kgm^{-3}]$
ρ_w	Density of water	$[kgm^{-3}]$
$\overline{\sigma}$	Total normal stress	$[kgm^{-3}]$
$\overline{\sigma}'$	Effective normal stress	$[kgm^{-3}]$
ϕ	Friction angle of the soil	$[°]$
ϕ_c	Friction angle of clay	$[°]$
ϕ_s	Friction angle of sand	$[°]$
τ_0	Bottom shear stress	$[Pa]$
$\tau_{0,e}$	Effective bottom shear stress	$[Pa]$
τ_b	Bed shear stress	$[Pa]$
τ_c	Critical shear stress	$[Pa]$
Θ	Shields parameter	$[-]$
Θ_c	Critical Shields parameter	$[-]$
χ_{jet}	Angle of incidence of the jet	$[°]$
ψ	Correction factor Bishop stability criterion	$[-]$
ω	Empirical factor in Prooijen and Winterwerp (2010)	$[-]$

1

Introduction

This Chapter introduces the research topic. Section 1.1 describes the global trends on flood risk and the need for accurate modelling of processes contributing to dike failure. The typical structure of a Dutch dike is discussed briefly in Section 1.2. An introduction to modelling dike failure (or breaching) is presented in Section 1.3, after which Sections 1.4 through 1.6 summarise the scope of this research and indicate how this report is structured.

1.1. Relevance of the research - Flood risk and crisis mitigation

This Section discusses the most recent prognosis on global flood risk posed by the Intergovernmental Panel on Climate Change (IPCC) and the ongoing improvements to the flood protection system in the Netherlands.

In 2014, IPCC identified various key hazards of climate change, of which coastal and inland flooding were among the most urgent. Research by Hirabayashi et al. (2013) on global changes in flood risks identified a worrying trend: floods of an equal magnitude as the 20th century once per hundred year flood conditions are becoming more frequent in many locations worldwide. The predicted changes in flood frequency and the consistency of these results across different climate models used is depicted in Figures 1.1a and 1.1b (Field et al., 2014).

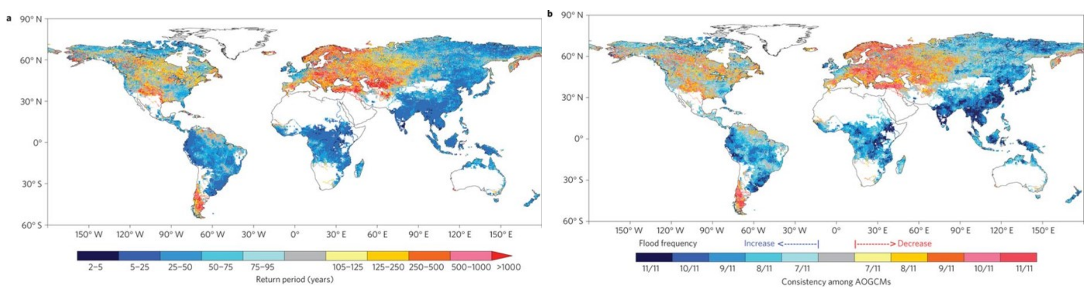

(a) Projected 21st century return period of the 100-year flood of the 20th century

(b) Consistency of predicted increase or decrease of flood probabilities across eleven models

Figure 1.1: Projected changes of flood probabilities in the 21st century (Hirabayashi et al. (2013))

Figure 1.1a indicates an increase in flood risk in Southeast Asia, South America and West-Europe, of which the latter is most consistently predicted (as can be seen in Figure 1.1b. In partial fulfilment of the European Flood Directive, the EU has required all its member states to assess the flood risks of river basins and coastal areas in their territory. Various improvement schemes to flood protections have been ongoing since 2015.

1.1.1. Flood risk management in the Netherlands

Due to its low-lying ground level, the Netherlands has always been prone to flooding. The long-standing experience of the Dutch with flood protection has resulted in a risk-based flood protection method. The Dutch design method is based on a tolerable level of three types or risk: Local Individual Risk, Group Risk and Economical Risk. The first defines a maximum risk to life for any individual or Local Individual Risk (LIR) in the Netherlands of 10^{-5} per year.

To express additional risk aversion against extreme floods, the Dutch have defined a group risk, which sets a stricter maximum flood probability for more densely populated areas in which more lives are at risk. The tolerable group risk is defined as the minimum level of safety for a group of individuals.

The final step in determining the design failure condition of flood protections concerns Economic Risk. A financial optimisation of the investment cost and expected damages results in a financially optimised failure condition. The design failure probability for flood protections then follows from the minimal failure probability between the three aforementioned risks (Mar et al., 1953, van Dantzig, 1956, Veerman et al., 2008).

The Dutch probabilistic design method assumes flooding to be caused by the occurrence of a failure mechanism, during which a certain solicitation (S) exceeds the maximum resistance of the structure. A structure fails if the solicitation exceeds the resistance. Figure 1.2 shows a probabilistic distribution of resistance and solicitation for a dike. Due to the heterogeneity of soil, the spread of the resistance for soil structures such as dikes is typically quite large, resulting in a wide distribution of the resistance. The grey area marks the possible combinations of solicitation and resistance for which the dike fails.

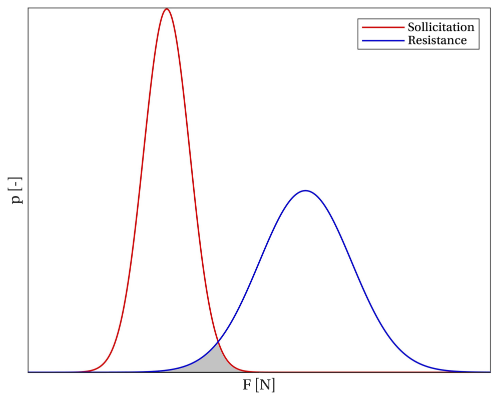

Figure 1.2: Probabilistic distribution of total resistant force R_f and soliciting force S_f

By determining the variation in solicitation and resistance parameters, flood protection structures such as dikes, levees or barriers can be tested and optimised based on the resulting failure probability. Based on the Dutch probabilistic design method, 1100 km of dikes in the Netherlands will be reinforced by 2031 at an expected expense of €7.1 billion (Rijkswaterstaat, 2019).

1.1.2. Opportunities to improve flood risk assessment

Although the assumption of a single failure mechanism leading to failure of a dike is quite suitable for large-scale risk assessment, the actual failure of a dike often results from a sequence of failures; the dike erodes and breaks as a result of the load, over a time of several minutes (brittle failure) up to many hours (ductile failure). The definition of brittle and ductile failure here is chosen relative to the typical length of a storm causing the flood. Relative to the length of a river discharge peak, typically lasting for a few days, the breaching process is a brittle failure.

A failure mechanism such as overflow first leads to a small volume of water entering the polder, but one can hardly think of this as a flood or failure. However, this initial flow causes further entrainment of the dike construction material, resulting in damage to the crest and landside slope of the dike. If the water level remains high, the entrainment of dike construction material leads to a loss of invert level, resulting in an increase in the flow rate through the dike. The higher flow rate in turn causes further entrainment of dike material and instability of soil masses. This process of positive feedback between failure mechanisms leads to a large opening in the dike, which is referred to as a breach.

The most notable floods in the Netherlands were caused by breaches in soil structures. An accurate description of this process can improve the accuracy of flood risk assessments and is vital to scenario analysis for crisis management in case of flooding. Modelling this process as a function of time can provide valuable information on the time available to take emergency measures or evacuate safely.

Section 1.2 introduces the most common type of flood defence in the Netherlands: dikes. Subsequently, Section 1.3 describes the processes considered in modelling the breaching of these dikes. In Sections 2.3 and 2.4 of the literature study, the state-of the-art in dike breach modelling is discussed.

1.2. Dike structure - Common dike profiles considered in this research

The most common structure protecting the Netherlands from flooding is a soil structure commonly referred to as a dike or levee. The cross-sectional layout of dikes varies greatly over space and time of construction. Different types of dikes have been classified based on the body of water retained by the dike (e.g. sea dikes, river dikes, lake dikes), on the function of the dike with respect to flood safety (primary and secondary defences) or on the materials used to construct the dike (e.g. sand dikes, clay dikes or peat dikes). This Section describes the cross-sectional dike profile considered.

This research solely considers dikes constructed out of sand and clay. These materials are commonly used in dike design in the Netherlands and other countries where sand is present in large quantities. Cohesive clay is used as a cover material, enclosing the sand core and protecting it from erosion due to flow or wave attack. Three typical dike profiles are depicted in Figure 1.3.

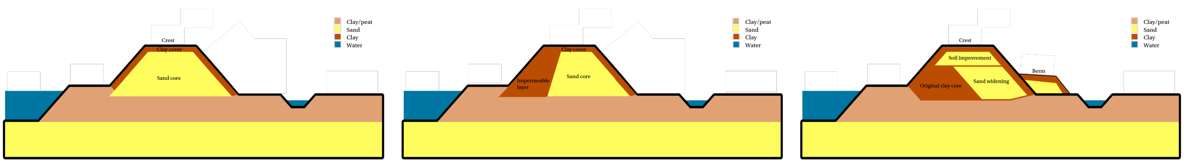

(a) Sand core enclosed by clay cover (b) Poorly permeable waterside slope (c) Phased dike improvement

Figure 1.3: Three forms of sand-clay dikes

Figure 1.3a shows the simplest dike considered, which is the assumed profile in the proposed breach formation model. The dike body consists of a sand core, covered by a poorly erodible clay layer. Figure 1.3b shows a common variant of this dike, which includes a thicker, poorly permeable waterside slope, often used to prevent seepage. Figure 1.3c depicts a dike, which has been reinforced, based on a smaller, traditional clay dike. Note that this dike also includes a berm on the landside slope. This relatively common addition can affect the stability of the landside slope significantly, as the dike is wider, but also shows more transitions in slope steepness, which are often subject to large erosion during overflow (Valk, 2009).

Dikes are normally covered by a hard or soft protective layer to shield the soil from wave attack or flow, preventing erosion. Soft measures, such as grass covers are most common on the landside slope. Hard dike covers are normally used in situations where significant wave attack is expected or where grass cannot grow to sufficient density. An example of such a location is the waterside slope of sea dikes, where the salinity of sea water impedes the growth of a sufficiently sturdy grass cover. The only cover type considered in this research is a grass cover, as this is the most commonly used protection on the landside slope, where initial damages show in overflow conditions (Visser, 1998). The structure and layout of a grass cover, as defined in the TAW is shown in Figure 1.4 (Muis, 1999).

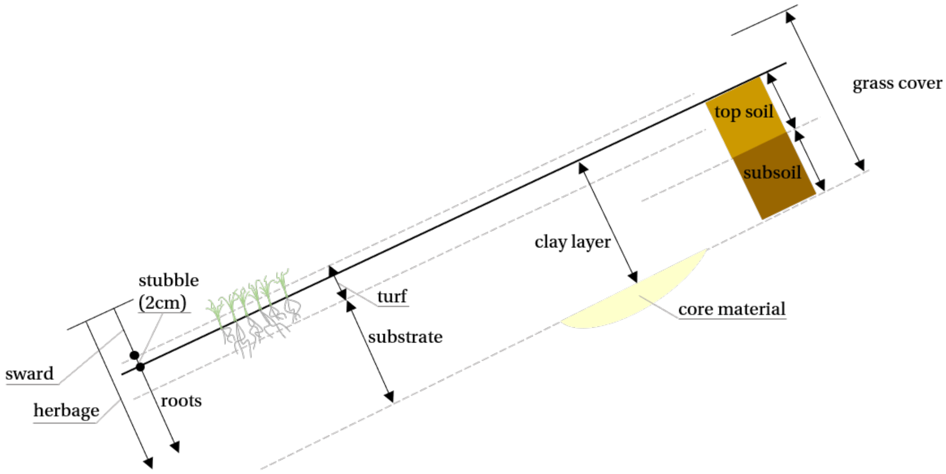

Figure 1.4: Structure and layout of grass covers (after: TAW 1999)

According to the TAW, the cover does not only include grass, but also the turf and clay layer, of which the hydraulic conductivity is influenced by the intrusion of the roots, cracks and weathering. The presence of irregularities or objects without a water-retaining function in the slope of the dike is not considered in this report. The failure of the grass cover, clay layer and subsequently, the erosion of the sand from the dike core leads to breaching of a dike. Section 1.3 gives an overview of the breaching process described by the models.

1.3. Breach modelling - An introduction

Attempts to model the initiation and development of breaches in embankments in various conditions date back over fifty years. Cristofano (1965) already developed a process-based model describing breach formation and growth, based on a weir flow formula and a simplistic derivation of an erosion formula (Courivaud et al., 2018). Since this first attempt, many different models have been developed, of which a number are still relevant to the state-of-the-art of breach modelling at the time of writing (2019). Errors in modelled time-to-breaching, final breach width and peak flow rate are still quite large. Empirical models can easily miscalculate the aforementioned parameters by up to an order of magnitude (Froehlich, 2016a, Zhong et al., 2017). The most advanced process-based models still have a margin of error of approximately 25 percent, rising up to 70 percent in cases where the processes modelled do not correspond with the observed mechanism leading to breaching (d'Eliso, 2007, Froehlich, 2008, Zhong et al., 2017). An more extensive overview of breach models, their mathematical formulations and assumptions is given in Sections 2.3 and 2.4.

A lack of consensus appears throughout the entire modelling process: in the formulation of hydraulic loads, the definition of geotechnical stability and the quantification of erosion rates in horizontal and vertical directions many different formulas are used. Even common phenomena are regularly referenced by different names. The remainder of this Section lists the terms used in the research and visualises the processes included in the breach model.

Flooding: The inflow of a volume of water into the polder equal to the surface area of the polder multiplied by a water depth of 0.20 metres. This definition is based on the Dutch standard definition of flooding, but more generally applicable.
The Dutch standard definition of flooding states: The unplanned presence of an average water depth of 0.20 metres in the hinterland in at least one area of equal four-digit postal code (based on the zones identified by the Dutch Central Bureau for Statistics) (CBS).

Failure mechanism: The loss of the water retaining function of the dike due to a form of loading exceeding the relevant form of resistance.

Breaching: The process consisting of breach initiation, breach formation and lateral breach growth. The term breaching is used in this report to describe the aforementioned steps collectively.

Breach initiation: The increase in hydraulic load on a dike, until first damage to the dike cover.

During overflow, damage is found first on either a slope transition (such as the toe of the dike), or near a local weakness in the cover. Overflow and wave overtopping differ significantly in this sense, as the preferential location of damage observed during wave overtopping lies further up the slope, where the waves crash down on the slope. Figures 1.5a and 1.5b show the typical initial damage during overflow near a local weakness (Bakker and Mom, 2015b).

(a) Existing weak spot in grass cover

(b) Damage after 4 hours of 160 l/m/s overflow)

Figure 1.5: Failure of a grass cover near a weak spot during overflow (after: Bakker and Mom (2015b), see Chapter 3)

Breach formation: The erosion process between initial damage to the dike cover and the presence of a breach, which lowers the invert level of the dike to below the MWL.

The initial damage develops until the clay cover is eroded, after which the erosion of the sandy core leads to a reduced invert level. Figures 1.6a and 1.6b show the erosion of the clay cover (Bakker and Mom, 2015b). The small irregularities at the bottom of test section 8 (in combination with a local weak spot in the clay layer), which can be seen in Figure 1.6a have resulted in a significant local erosion, shown in Figure 1.6b.

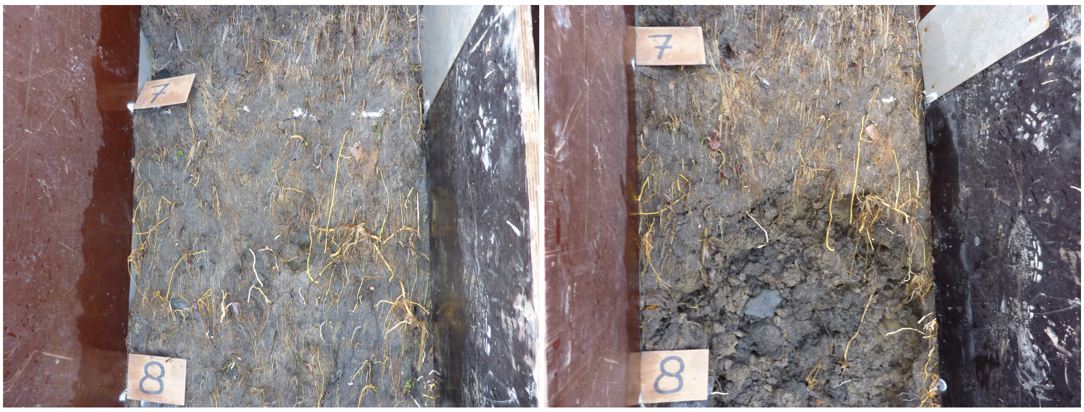

(a) Damage to the clay cover after 15 minutes of overflow

(b) Damage to the clay cover after 49 minutes of overflow)

Figure 1.6: Local erosion of the clay layer due to overflow (after: Bakker and Mom (2015b), see Chapter 3)

As soon as the non-cohesive core material of the dike becomes exposed due to the erosion of the cohesive clay cover, the erosion rate increases locally, resulting in large erosion and the development of a headcut: a steep cliff from which the water cascades down, resulting in a jet of water on the exposed sand downstream. The jet subsequently forms a scour hole in the sand, undercutting the steep cliff, which then tumbles over. This process is shown in Figures 1.7a and 1.7b (Bakker and Mom, 2015b).

(a) A steep headcut during overtopping (top view)

(b) A headcut stability failure during overtopping (top view)

Figure 1.7: Headcut growth due to local sand scouring (after: Bakker and Mom (2015b)), see Chapter 3

This iterative process of erosion and stability failure, further referenced as headcut erosion, leads to an increasing height of the headcut, and to a large loss of dike material. When the headcut migrates through the waterside slope, the invert level is lowered and the rate at which water flows through the breach increases.

Lateral breach growth: The phase following breach formation, in which the breach grows mainly in width.

When the invert level has been lowered to below the MWL, the increased flow through the breach leads to increased shear stresses along the wetted perimeter. Due to the large breach flow velocities, a scour hole below the breach forms. The wall shear stress imposed on the exposed core material on the lateral sides of the breach results in additional erosion, widening the breach. The process of lateral growth is ended when the flow shear stress falls below a critical value. Figures 1.8a and 1.8b show the lateral growth of a man-made relief breach (made to allow water to drain from the flooded area) due to breach flow (USACE, 2011).

(a) Breached levee near the Mississippi river (2011)

(b) Widened breach due to breach flow

Figure 1.8: Lateral breach growth and transition from supercritical to subcritical flow (USACE, 2011)

1.4. Problem definition - Unreliable modelling of the breach formation process

In conclusion, current breach models agree reasonably well on the relevant hydraulic effects and equations used to model breach flow. However, they describe the erosion processes during breaching by simplified equations. Therefore, they fail to accurately capture the sensitivities of the process to input parameters. This makes the existing models unreliable and unsuitable for design.

Differences between models are mostly found in two fields: the included erosion processes (and formulas) and the influence of geotechnical stability of layers on breach formation. Most models use a surface erosion formula, relating the erosion to the critical bed shear stress (τ_c $[N/m^2]$, as given in Equation 1.1, but both the erodibility coefficient k_e (of which the unit depends on the exponent ζ) and the exponent ζ vary greatly between models and flow regimes (Bisschop, 2018, Bisschop et al., 2016).

Another point of criticism on this formula in general is that the shear stress caused by a flow of water is a phenomenon averaged over a much larger scale than the micro-scale on which granular particles experience forces. Finally, no model identifies a clear transition between surface erosion and headcut erosion, requiring some form of expert judgement to determine which process dominates, whereas these erosion processes lead to breaching in a completely different erosion pattern. Figure 1.9a shows a typical surface erosion pattern on a test section, characterised by small variations in erosion depth. The headcut erosion depicted in Figure 1.9b shows local steepening of the slope by shearing of soil masses.

(a) Surface erosion observed during overflow tests on sand (after: Yagisawa (2019a), see Chapter 3

(b) Headcut erosion observed during overtopping tests on a grass-covered dike (after: Bakker and Mom (2015b))

Figure 1.9: Typical appearance of surface erosion and headcut erosion

In both cases, the erosion drives the breaching. Although erosion formulas also vary greatly, the general form of any erosion formula is as shown in Equation 1.1. Note that the erosion rate, defined as the eroded volume of material per unit time can be calculated for both a two-dimensional grid system (in which the main directions are the direction the flow and upwards, perpendicular to the flow) and three-dimensional grid system (in which the third dimension is horizontal and perpendicular to the flow direction), as long as the distribution of the bed shear stress (τ_b) is known in the desired dimensionality.

$$E = k_e \cdot (\tau_b - \tau_c)^{\zeta} \tag{1.1}$$

In which:

- E gives the erosion rate $[m^3 s^{-1}]$;
- k_e is the erodibility coefficient, of which the unit depends on exponent ζ;
- τ_b is the actual shear stress at the dike surface $[Nm^{-2}]$;
- τ_c is the critical shear stress of the exposed soil particles $[Nm^{-2}]$;

- ζ is a unitless exponent, defining whether the dependence of erosion on shear stress is linear or exponential.

Another shortcoming of most models lies in the geotechnical stability, mostly relevant for the slope stability of the breach. As many models use significant simplifications, the effective stress and soil weight calculations used to determine the stability of the slope are unreliable in many cases, since effects such as a varying phreatic surface and unsaturated zones are not modelled. d'Eliso (2007) identified that even non-cohesive core material is stable in near-vertical cliffs during breach formation, although this was not yet included in any breach model. Finally, the presence of vermin infrastructure, small structures such as stairs, walls and roads and the spatial variation of soil strength parameters make it difficult to compare model results (which are almost exclusively based on a simplified dike profile of homogeneous layers without structures) with measured data.

1.5. Research scope - Time-dependent breach formation modelling

This research quantitatively describes overflow-induced breaching as a function of time in dikes consisting of a sand core and a clay cover, based on a process-oriented model. The model describes the observed large-scale erosion phenomena, based on the assumption that headcut erosion (as described in Section 2.2) dominates the erosion process through both the cohesive cover and the non-cohesive core material of a dike. This assumption has not been made in earlier models for the core material, but corresponds well with visual observations on large-scale tests. In various tests, non-cohesive material was observed to remain stable under steeper slopes than commonly assumed (due to partial saturation or the presence of a cohesive cover) (Geisenhainer and Oumeraci, 2009, Trung, 2014, Trung et al., 2015, Zhang et al., 2009, Zhao, 2016, Zhu et al., 2010). The phenomenon of headcut erosion is best described by a combination of a stability criterion for the steep headcut cliff and a pick-up flux to describe the erosion of the non-cohesive core at the bottom of the headcut, as elaborated upon in Section 2.2 (Bisschop, 2018, van Damme, 2019).

The model is applicable as a scenario analysis tool when assessing the flood risk of a dike. The output produced by the model includes the time-to-failure of the grass and clay covers, as well as the time until crest lowering occurs and finally, the formation of a complete breach in the dike, which only grows laterally.

The time-dependency of the model enables the user to determine various characteristic moments in time: The time until various layers in the dike have eroded, the time at which the polder is considered flooded, as well as an ultimate moment in time, until which breach formation can be stopped using emergency measures. Knowing the available time to evacuate or apply mitigative measures ahead of the flood makes it significantly easier to prepare and provide advise The objective of this research is formulated as follows:

To quantitatively assess dike breach formation, based on a headcut erosion model and to determine the relevance to flood risk mitigation.

To arrive at a result, which fulfils the objective, the research scope is structured by posing a research question and various sub-questions. These are listed and detailed below, providing an overview of the scope of this research. A short discussion per question describes the extent of the scope. The general question this research seeks to answer is as follows:

In what way does overflow-induced headcut erosion lead to the formation of a dike breach and subsequently to flooding?

The following sub-questions are posed to structure the research:

What soil parameters are directly relevant to headcut erosion?
The proposed BRAM-model is based on headcut erosion, which has been known to occur in cohesive material, but has not yet been modelled in granular, non-cohesive soils. To describe how headcut erosion is caused in a dike consisting of different materials, the phenomena and soil parameters leading to this effect are discussed. These parameters have been determined through an analysis of the relevant phenomena in the headcut process. The relevant parameters have been quantified by geotechnical lab work for a case study.

What formulas describe headcut erosion accurately?
The model is to accurately describe the breach formation process over time, based on a water level as a load parameter and resistance parameters, related to layers of the dike body. This research question addresses the development of the inner workings of the breach model; the assumptions made in modelling, loads and resistances included and an assessment of the sensitivity of the model outcome to changes of input parameters.

What is the horizontal migration velocity of the headcut?
To assess what the effect of a temporary overflow situation is on the dike, the migration velocity of headcuts in the dike is essential. The migration velocity is the horizontal velocity of the headcut to the waterside slope. A higher velocity of headcut migration results in a shorter duration of breach formation. If the headcut migrates through the waterside slope, the invert level of the dike is lowered, allowing water to flow through the breach even if the bosom water level drops. Therefore, the velocity of headcut migration determines the duration of the extreme loading the dike is able to withstand without breaching.

What observations of damage to the landside slope of a dike can be used as indications to evacuate or to implement mitigative measures?
The time-dependence of the model is used to determine the duration of breach formation stages. Estimates of the time-to-failure of each component of the dike are made. This aids decision-making in case of an eminent breach.

1.6. Research method

This Section describes the process through which the research question and sub questions are answered. The project is separated in various sections, of which the topics are introduced below.

The literature study in Chapter 2 provides the background information against which this research is conducted. The processes of overflow and (headcut) erosion are defined and the state-of-the-art in breach modelling is given.

Chapter 3 discusses various erosion and damage tests, based on which the breach formation model is validated.

In Chapter 4 a new process-oriented model is posed, which describes the breach initiation and breach formation process due to overflow-induced headcut erosion. The chapter also includes the validation of each of the model components and a suggested pre-existing method to describe lateral breach growth. This Section

The breach formation model is applied to a number of case studies in Chapter 5, indicating the estimated time-to-failure, peak flow and final breach width of various dikes due to overflow-induced headcut erosion.

Finally, conclusions on the applicability of the Breach Resistance Assessment Model (BRAM)-model are drawn, and a reflection on the fulfilment of the research objective is presented in Chapter 6. This Chapter also includes further research recommendations on the improvement of breach formation modelling.

2

Literature Study

This Chapter summarises the theoretical research conducted on overflow-induced headcut erosion, leading to the formation of a dike breach. Section 2.1 discusses the flow of water over the levee and the relevant forces transferred to the levee, after which Section 2.2 describes the headcut erosion process, which leads to dike breaching. Finally, Sections 2.3 and 2.4 present the state-of-the-art (2019) in breach modelling and evaluate the merits and opportunities for improvement of the existing models.

2.1. Overflow - Simulated conditions

During overflow, the water level outside the polder exceeds the invert level of a dike, inducing a flow of water over the crest. This results in an increase in static water pressures on the waterside dike slope. As soon as overflow occurs, the dike crest and landside slope are subjected to shear stresses. Due to the larger flow depth, shear stresses acting on the waterside slope are smaller are commonly neglected in case of overflow. Assuming steady flow, the shear stress on the bed (defined as in Equation 2.1a) can be expressed as given in Equation 2.1b (Schiereck and Verhagen, 2016).

$$\tau_b = \mu \cdot \left(\frac{\delta u}{\delta z} + \frac{\delta u}{\delta x} \right) \tag{2.1a}$$

$$\tau_b = \rho_w u_*^2 = c_f \rho_w \overline{u}^2 \tag{2.1b}$$

In which:

- μ is the dynamic viscosity of the flow $[Nsm^{-2}]$;
- u is the velocity of the flow along the boundary $[ms^{-1}]$;
- z is the vertical distance to the boundary $[m]$;
- c_f represents the (nondimensional) friction coefficient;
- ρ_w is the density of water $[kgm^{-3}]$;
- $\overline{u}$ is a representative mean flow speed $[ms^{-1}]$;
- u_* is the shear velocity $[ms^{-1}]$.

Figure 2.1 shows the the shear stress for increasing boundary layer thickness. A more pronounced boundary layer results in a smaller spatial derivative of the flow speed and thus a smaller shear stress. The highest shear stress therefore occurs at the left-most velocity profile in Figure 2.1, decreasing to the right. An unsteady flow leads to flow velocity variations and prevents a boundary layer from developing fully, resulting in larger local shear stresses. During overflow, the flow is assumed to be quasi-steady, which means the flow regime varies quite slowly. In these conditions, the assumption of steady flow is valid and provides an accurate estimation of the shear stresses.

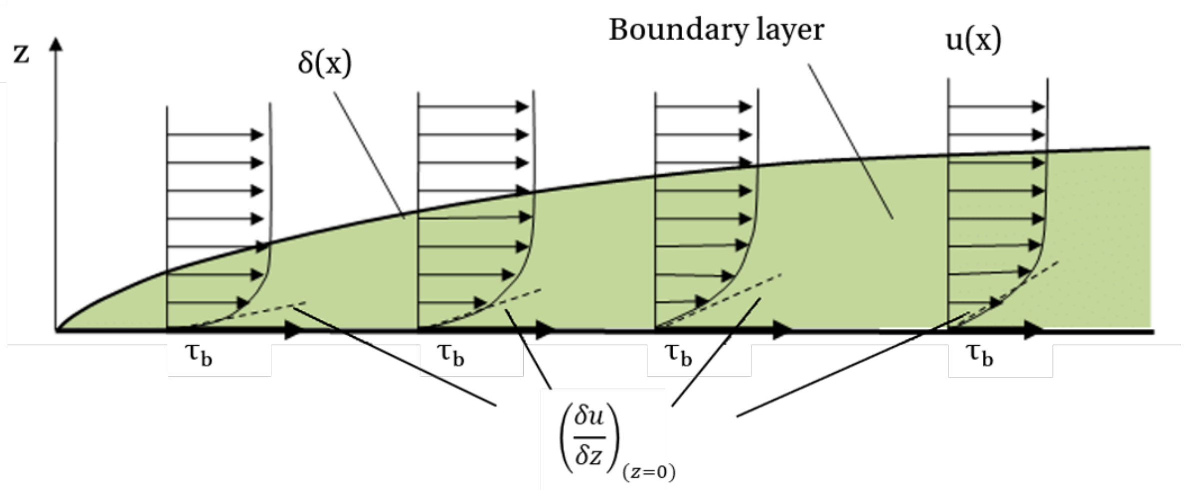

Figure 2.1: Shear stress for varying boundary layer thickness

The friction coefficient in steady, turbulent open water flow can be calculated through the equations of Chézy (1775) or Manning (1889), assuming quasi-steady flow. The equation posed by Chézy (1775) is given in Equation 2.2a and relates the cross-sectional average velocity v to the hydraulic radius R and energy gradient i of the waterway, using the Chézy coefficient C. The Chézy coefficient for a relatively flat bed can be estimated using the White-Colebrook equation, given in Equation 2.2b (Colebrook, 1939, Colebrook and White, 1937).

$$u = C \cdot \sqrt{R \cdot J} \tag{2.2a}$$

$$C = 18 log_{10}\left(\frac{12R}{2D}\right) \tag{2.2b}$$

In which:

- C is the Chézy coefficient $[m^{1/2}s^{-1}]$;
- R is the hydraulic radius $[m]$;
- J is the nondimensional energy slope;
- D is the grain diameter $[m]$.

Manning (1889) posed an alternative to the Chézy equation, specifically for steady, turbulent open water flow, which is given in Equation 2.3a. A similar shape of the equation relates the flow velocity (u) to the hydraulic radius (R, see Equation 2.3b) and the energy gradient of the waterway (J), using Manning's coefficient (n) (Gauckler, 1867, Manning, 1891). The Manning and Chézy roughness along a slope can be expressed as a function of one another using Equation 2.3c.

$$\overline{u} = \frac{1}{n} \cdot R^{2/3} \cdot J^{1/2} \tag{2.3a}$$

$$R = \frac{A}{P} \tag{2.3b}$$

$$C = \frac{1}{n} \cdot R^{1/6} \tag{2.3c}$$

In which:

- A is the cross-sectional area of the flow $[m^2]$;
- P is the wetted perimeter $[m]$;
- n is the Manning-coefficient $[sm^{-1/3}]$.

An alternative empirical expression for friction energy loss was expressed by Prandtl (1925), through his one-seventh power law, presented below in Equation 2.4. This equation describes the friction coefficient C_f and is strictly applicable to turbulent flow.

$$C_f = \frac{0.027}{Re^{\frac{1}{7}}} \tag{2.4}$$

In which

- Re_x is the Reynolds Number

To determine the shear stress on the landside dike slope during overflow, the flow velocity of the water over the dike is an essential parameter. Recent research by Zhong et al. (2017) indicated that the point where flow depth approaches normal flow determines the location of initial damage if the landside slope of the dike is sufficiently long. If the slope length is insufficient for turbulent flow to reach normal depth, first damage shows at the landside toe of the dike or at a local weak spot. The typical length of a landside dike slope in the Netherlands is insufficient for the flow to reach the normal depth, making slope transitions, such as at the toe of the dike, the likely location for initial damage to be found, barring weak spots or structures in the landside slope.

The Bernoulli equation, which Euler later defined in the form as shown in Equation 2.5, can be used to describe flow velocities on different points of the landside slope. The Bernoulli equation provides a simple relation between water level and flow speeds on various locations, based on the conservation of energy and various assumptions: a steady flow of incompressible fluid, in which turbulence is negligible. This final assumption strictly speaking does not hold for overflow over a dike, as the flow becomes turbulent along the landside slope.

$$h_0 + \frac{u_0^2}{2g} = h_i + \frac{u_i^2}{2g} \tag{2.5}$$

In which:

- h_0 is the hydraulic head on the dike crest $[m]$;
- u_0 is the flow velocity at the dike crest $[ms^{-1}]$;
- h_i is the hydraulic head on a point of interest on the landside slope $[m]$;
- u_i is the flow velocity on a point of interest on the landside slope $[ms^{-1}]$;
- g is the gravitational acceleration $[ms^{-2}]$.

Variation in weir flow formula for various breach shapes is most commonly used to determine the flow through a dike breach. The weir flow formula follows from the Bernoulli equation and is thus relies on the same assumptions. All weir equations can be generalised to the following form:

$$Q_w = C_d \cdot A \cdot \sqrt{2g\Delta H} \tag{2.6}$$

In which:

- C_d is a nondimensional weir discharge coefficient;
- Q_w is the flow rate through the weir $[m^3 s^{-1}]$;
- ΔH is the difference in head level over the weir $[m]$.

The flow rate through a breach thus depends on the head level difference over the weir (ΔH), the area through which water flows (A) and includes a discharge coefficient (C_d), which varies for different weir types and can also vary over time during breaching of a the dike, as vertical and horizontal flow contraction only apply in specific flow conditions (van Damme et al., 2012). When this coefficient is varied for discharge conditions, it is often referred to as a 'variable weir coefficient'.

Four types of weirs have been distinguished, based on the ratio of their crest length to the water level. The water level is assumed to exceed the crest level, assuming a continuous overflow of the dike. As usually, the steepness of a dike slope lies between 1 : 2 and 1 : 4, accounting for some crest width, most dikes have been categorised as broad-crested weirs through the categories given below.

- Long-crested weir: $(h_0)/L_w \leq 0.1$
- Broad-crested weir: $0.1 \leq (h_0)/L_w \leq 0.35$
- Narrow-crested weir: $0.35 \leq (h_0)/L_w \leq 1.5$
- Sharp-crested weir: $1.5 \leq (h_0)/L_w$

Bos (1985) proposed an empirical relation to estimate the discharge coefficient, based on his research on broad-crested weirs and long flumes of various shapes. His formula relied on the same height-to-length ratio used to categorise weirs, as shown in Equation 2.7.

$$C_d = 0.93 + 0.1\frac{h_0}{L_w} \tag{2.7}$$

In which:

- h_0 is the head level at the dike or weir crest $[m]$;
- L_w is the horizontal length of the weir $[m]$.

Fritz and Hager (1998) provided a second empirical formula for the discharge coefficient, dependent on the relative crest length, a parameter similar to the height-to-length ratio used by Bos (1985). The empirical relation by Fritz and Hager is given in equations 2.8a and 2.8b.

$$C_d = 0.43 + 0.06 \cdot \sin\big(\pi(\epsilon - 0.55)\big) \tag{2.8a}$$

$$\epsilon = \frac{h_0}{h_0 + L_w} \tag{2.8b}$$

Van Damme et al. (2012) proposed a simple breach stage-varying weir coefficient, based directly on the effects of the breach shape on the flow contraction. This coefficient which was applied in the AREBA model and is given in Equation 2.9.

$$C_d = \begin{cases} C_1 & \text{for crest width} \geq 0, \\ C_1 \cdot C_2 & \text{for crest width} < 0 \text{ and crest height} > 0 \\ C_2 & \text{for crest height} = 0 \end{cases} \tag{2.9}$$

The discharge coefficient presented is composed of two components (C_1 and C_2) respectively representing vertical and horizontal contraction of flow. Its application is tied to the phases of breach formation, during which the flow is contracted horizontally, vertically or both. Although no values are proposed in van Damme et al. (2012), the simple form of the weir coefficient, based on the flow regime is the most elegant solution. Morris (2011) defines a value of C_d between 0.8 and 1.5, of which the former applies to rectangular breaches, quickly increasing to 1.0 for even slightly rounded and 1.5 for completely rounded breach shape.

Finally, when the turbulent overflow reaches the dike toe (or berm, if present), it encounters a sudden transition from the slope to a horizontal ground level. This causes a hydraulic jump. Such a transition often coincides with large local turbulence, resulting in significant erosion due to the local energy dissipation. The ratio between the water depths in this situation follows from the momentum balance and is referred to as the as the Bélanger equation, given as Equation 2.10 dissipated energy (expressed in head level) along a hydraulic jump is given in Equation 2.11.

$$\frac{d_i}{d_g} = \frac{\sqrt{1+8Fr^2}-1}{2} \tag{2.10}$$

$$\Delta E = \frac{(d_g - d_i)^3}{4h_g \cdot h_s} \tag{2.11}$$

In which:

- d_i is the water depth on the landside slope $[m]$;
- d_g is the water depth on the ground level $[m]$;
- Fr is the nondimensional Froude number;
- ΔE is the dissipated energy over the hydraulic jump expressed as a height $[m]$.

2.2. Headcut erosion - A process description

The shear stresses on the dike body posed by the overflowing water are counteracted by the shear resistance in the exposed layer, which is either the grass cover or an underlying soil layer, which becomes exposed due to failure of the layers above. This research assumes that headcut erosion dominates breach formation (See Section 1.5). As opposed to surface erosion, headcut erosion is not caused by water flowing parallel to the slope, but caused by a local loss of material due to an impinging jet. Figures 2.2a through 2.2d show schematically how a headcut develops from initial damage to mass stability failure, according to d'Eliso (2007). As soon as the headcut starts migrating to the waterside, the jet becomes more pronounced, due to the increased height of the headcut.

In Figure 2.2a, a local weakness in the grass cover leads to an initial damage, exposing the clay layer. Figure 2.2b shows how the steep slope leads to local turbulence, eroding the clay layer and increasing the depth of the damage. As soon as the erosion reaches the more erodible sandy core material of the dike (Figure 2.2c), the erosion rapidly increases, undercutting the clay cover, leading to mass stability failures on either side of the scour hole and downstream slip surface failures of the clay cover due to the static pressure of the standing water (Figure 2.2d).

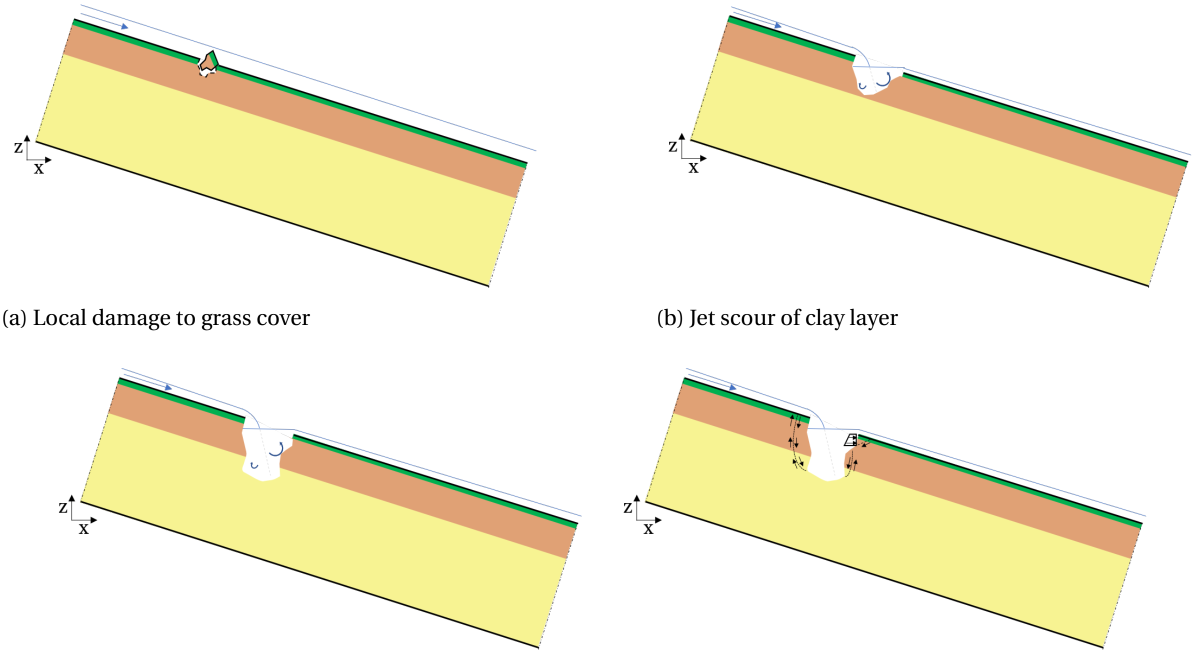

(a) Local damage to grass cover

(b) Jet scour of clay layer

(c) Erosion of sand

(d) Headcut stability loss

Figure 2.2: Headcut erosion

Thus, contrary to its name, headcut erosion does not solely describe soil erosion, but is rather a complex combination of flow regime changes, erosion and stability phenomena, which result in a retrograde failure of an embankment. The water depth in the plunge pool is limited by the backstop of soil downstream. When (a part of) the clay cover is sheared, water spills down and the plunge pool is (partially) drained.

The loss of upstream stability due to headcut erosion in cohesive materials has been modelled by Hanson et al. (2005a), Zhu (2006) and d'Eliso (2007). These models share one major shortcoming for application on a Dutch dike: headcut erosion is assumed not to occur in the non-cohesive material of the dike. Instead, it is assumed that this material is eroded due to surface erosion and only retains a limited slope steepness, which does not correspond to visual observations of large-scale tests. This misrepresentation of the erosion process results in errors estimating the residual strength of a dike, as the flow regime in the headcut plunge pool are clearly different from parallel flow over a constant slope, increasing the erosion rate.

The complex interaction between slope failures and the influence of the failed material on the flow over the dike is often neglected, implicitly assuming the waste to be washed out instantaneously. For small slope stability failures (up to approximately one metre in height), full-scale tests show that this assumption holds well, as the waste material is washed away in a matter of seconds. However, for large slope stability failures, such as slip surfaces running from dike crest to toe, this assumption does not hold. In such a case, the assumption of instant soil wasting results in a small underestimation of the time-to-failure. The following subsections elaborate on the relevant phases of dike breaching in a dike as described in Section 1.3, driven by headcut erosion.

2.2.1. Breach initiation - Grass cover failure

Failure of the grass cover is assumed to determine the onset of breach formation. Current knowledge on the time-dependent failure of grass covers is limited, and the strength of grass covers on different types of subsoil is a key research interest of Rijkswaterstaat (Rijkswaterstaat (RWS)). Some empirical stability criteria have been derived, based on experimental research. These relations do not include the effects of the presence of objects in a grass slope, such as stairs, trees etc. Correction of these formulas for the presence of these objects is commonly done by increasing the local flow speed, although this does not account for the local weakness expected in grass-structure transitions (d'Eliso, 2007, Hewlett et al., 1987, Muis, 1999, van Damme et al., 2012).

The TAW identified wave overtopping as the main failure criterion for a grass cover, thus only describing the time to failure of grass as a function of wave height and quality of the grass cover. Erosion criteria for the grass cover due to overflow shearing are not defined in Dutch design standards (Muis, 1999). The British CIRIA guide R116 by Whitehead et al. (1976) poses a graph from which the flow velocity over a grass cover at failure, based on a distinction in grass covers, can be found. Curve fitting to this graph results in the Equations 2.12a through 2.12c, in which grass Category 1 indicates a cover of good quality and Category 3 refers to covers of poor quality. The following factors make for an ideal grass cover: a large variety of deep-rooted grass species (preferably rhizomatic, meaning that the roots extend away from the plant through the clay layer, rather than on top of the soil (stolonic)), the absence of bare patches or vermin infrastructure, a gradually varying slope profile and the absence of structures interrupting the grass cover. The flow speed required to damage the cover u_g is given as a function of duration of loading T for various grass cover qualities. A graph of these formulas is shown in Figure 4.8.

$$u_{g1} = 2.385 - 0.0167 \cdot \ln\left(T + \frac{5.333}{T}\right) \tag{2.12a}$$

$$u_{g2} = 2.161 - 0.131 \cdot \ln\left(T + \frac{5.551}{T}\right) \tag{2.12b}$$

$$u_{g3} = 1.889 - 0.236 \cdot \ln\left(T + \frac{2.767}{T}\right) \tag{2.12c}$$

In which:

- u_g is the depth-averaged overflow velocity for which the grass cover fails $[ms^{-1}]$;
- T is the time for which overflow has been present $[h]$.

An alternative to describing the failure of grass was presented by Temple and Hanson (1998) and later used as a part of the model presented by D'Eliso 2007 (d'Eliso, 2007, Temple and Hanson, 1998). The criterion for grass failure was defined as a point in time where the cumulative bottom shear stress (integrated with respect to time) exceeded a certain value, which depends on the plasticity index I_p of clay, as given in Equation 2.13b.

The resulting t_{gf} is considered the time of failure of the grass in hours. $\tau_{0,e}$ denotes the effective bottom shear stress, given by Equation 2.13a.

$$\tau_{0,e} = \rho_w g d J (1 - C_f)\left(\frac{n_c}{n_{tot}}\right) \tag{2.13a}$$

$$\int_0^{t_{gf}} \tau_{0,e} dt = 3600 \cdot (9I_p + 50) \tag{2.13b}$$

In which:

- $\tau_{0,e}$ is the effective bottom shear stress $[Nm^{-2}]$;
- n_c is the Manning's roughness of clay $[sm^{-1/3}]$;
- n_{tot} is the total Manning's roughness of grass and clay $[sm^{-1/3}]$;
- t_{gf} is the time of grass failure $[s]$;
- I_p is the plasticity index of the clay [%].

The energy slope J is given as a function of the Manning's roughness n, mean flow velocity $\overline{u}$ and the hydraulic radius of the breach R_b. (Equation 2.14).

$$i = \frac{n^2 \overline{u}^2}{R_b^{4/3}} \tag{2.14}$$

Although the formulas posed by Temple and Whitehead are quite different in form, the processes both models attempt to describe are similar; the quality of the grass cover and plasticity index assign a certain sensitivity of the grass cover to the time-dependent increase in saturation of the grass sod with water. This reduces the remaining shear strength of the cover until the imposed shear stress brings the grass cover to failure trough roll-up or sliding (Ponsioen, 2016). These formulas, often used in 2D-modelling, are representative for the three-dimensional situation, as they are based on experiments in which the grass experienced a shear stress over a small width, allowing the grass cover at each side to contribute to the resistance. A schematic representation of the shear stresses and water flows on a grass sod are shown in Figure 2.3.

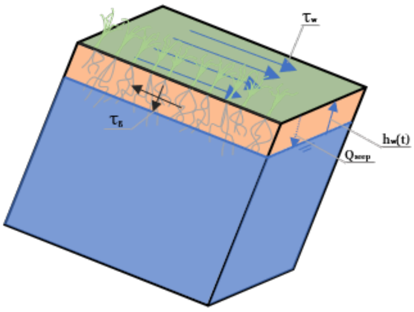

Figure 2.3: Shear forces on a grass sod due to overflow

2.2.2. Clay cover failure

When a grass sod fails, the cohesive cover becomes exposed. As surface erosion in cohesive soils is a relatively slow process, the development of headcut erosion becomes the most relevant erosion process after initial damage. A key assumption here is that damage grass results in a hole deep enough to initiate headcut erosion as a dominant process. Temple defined the minimal headcut height as the critical flow depth, given in Equation 2.15 (Nobel, 2013, Temple and Moore, 1997).

$$d_c = \left(\frac{q^2}{g}\right)^{\frac{1}{3}} \tag{2.15}$$

In which q is the specific discharge over the grass.

For overflow rates up to 100 l/m/s ($q = 0.1 m^2/s$), this equation results in a maximum initial headcut height of 10 centimetres, which can is normally exceeded by the roll-up or sliding failure of a grass sod (as the failure depth is larger than 0.1 metres), making it a reasonable assumption that the failure of the grass cover initiates headcut erosion of the slope (Muis, 1999).

The headcut initially grows primarily in height, rather than width, as the clay at the bottom of the headcut experiences jetting, providing the extra water pressure needed to allow water to infiltrate in between the fine clay particles, eroding clay masses from the bottom, whereas the sides of the headcut only experience shear stresses due to the turbulent flow of water. As surface erosion due to exceedence of a critical shear stress is a drained process and the permeability of clay is various orders of magnitude lower than the timescale of the erosion process, the infiltration of water and thus the erosion of the clay on the lateral slopes of the headcut is negligible. When the depth of the headcut reaches the non-cohesive core of the dike, the next phase is started (Nobel, 2013).

2.2.3. Jetting of the non-cohesive core

The most common material in dike cores in the Netherlands is sand, which normally lacks the cohesive effects of clay, due to the lack of fine particles and absence of electrostatic or other cohesive forces. The erosion of sand is a drained process, described by a critical shear stress formula (of the general form in Equation 1.1. However, during breach formation in a dike with a cohesive cover, two additional modelling steps are needed: a description of the impinging jet flow and the shear stress distribution downstream of the headcut as a result of this jet. A headcut erosion model requires adapted erosion formulas, based on the two following arguments.

First, Bisschop et al. (2016) showed that sand masses are sheared, rather than eroded grain-by-grain when subjected to high flow velocities, such as observed during dike breaching. This is the result of a dilatancy effect of the sand and an inward water head gradient, which increases the undrained shear strength of the sand. The inward water head gradient pulls the grains together, causing macroscopic effect similar to the electromagnetic forces drawing clay particles towards the water, commonly referred to cohesion. When water infiltrates, this effect is lost, and a layer of soil is eroded at once (Bisschop et al., 2016).

Second, due to the presence of a cohesive layer and a grass cover over the granular core material, the headcut has already formed before the sand even becomes exposed to any flow. When the sand finally becomes exposed, it is subjected to jetting and highly turbulent flow, which cannot be described by surface erosion formulas. Bisschop described a pick-up flux formula for higher flow velocities, which suits the erosion of sand in such conditions much better (Bisschop, 2018, Heijmeijer, 2019).

Stability of the clay layer is then lost due to two mechanisms. The first is undercutting due to sand scour, an erosion phenomenon where the more erodible sand is washed out from under the clay layer. D'Eliso (2007) identified three failure conditions for the clay layer due to undercutting. The first is a loss of vertical stability, due to a lack of vertical support. (Figure 2.4a) Both the second and third layer consider a loss of rotational stability, however, D'Eliso separates a bending and overturning failure. Bending failure is caused by a stress cracks at the top of the overhanging clay mass, whereas rotational stability is caused by the development of horizontal tensile forces in the clay. (Figure 2.4b) (d'Eliso, 2007).

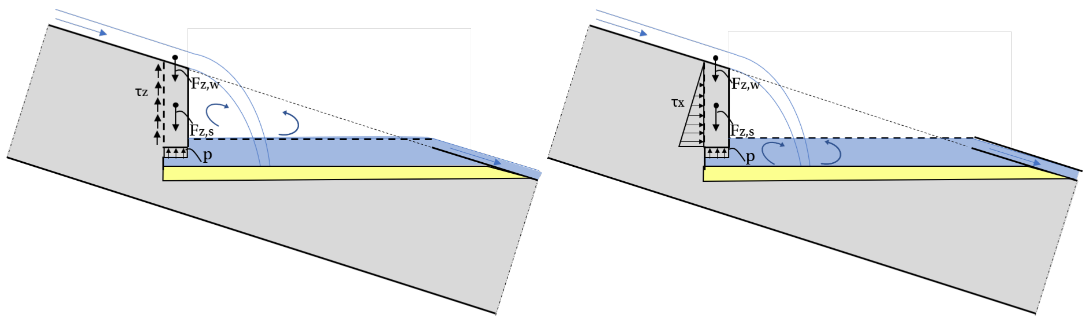

(a) Shear failure of a headcut slope

(b) Bending or overturning failure of a headcut slope

Figure 2.4: Headcut failure mechanisms (after: D'Eliso (2007)

The second effect causing clay cover instability is a slip surface failure, causing large soil mass displacements. When the breaching process takes longer, the phreatic surface in the dike rises due to the increase in water level, resulting in a reduction of effective and shear strength of the soil. As the passive region in normative slip surfaces often lies near the toe of the dike, an initiated headcut reduces the resisting mass of soil. Headcuts are commonly initiated here, assuming: overflow to be the cause of initial damage, no notable weak spots and a turbulent flow along the entire landside slope (Zhong et al., 2017, Zhu, 2006). The loss of material in the passive soil wedge and saturation of the dike can lead to a loss of stability of the headcut. Note that for other causes of headcut initiation, such as local weak spots or overtopping failure, the headcut is initiated higher up the slope and the normative slip surface shifts accordingly.

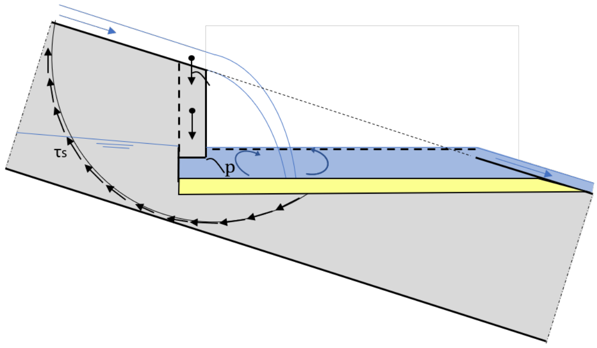

Figure 2.5: A large slip surface through a steep headcut slope

2.2.4. Crest lowering and lateral breach growth

Due to the mechanisms described in the previous subsection, the headcut advances along the landside slope through the crest of the dike. When the headcut migrates through the waterside slope, the invert level of the levee is lowered and the breach flow increases significantly. The growth of the breach becomes mainly lateral. The remaining cross section behaves like a weir and is eroded rapidly due to the high flow velocities. The final part of the cross section is sheared rather than eroded, due to the large water pressure, increased flow shear stress and reduced shear resistance.

The lateral breach growth phase is not considered a part of breach formation, but rather modelled as a secondary process. Breach formation models commonly assess breach width through an assumed ratio of vertical and horizontal breach growth, most commonly 1.4, following from the ratio between shear stresses at the bed and side of the breach (d'Eliso, 2007, Hanson et al., 2005a, van Damme et al., 2012). The implementation of the headcut model through all dike layers renders such an assumption superfluous, as the stability criterion can be used for both breach formation and lateral growth.

The following Sections discuss the most relevant existing breach models and the methods and assumptions used in these models to determine essential parameters, such as the time-to-breaching, final breach width and peak inflow of water into the hinterland.

2.3. Breach models - a state-of-the-art (2019)

To evaluate the current breach models, the models have been categorised, based on the type of applied formulas. The formulas and their assumptions provide an indication of the applicability and predictive qualities of the model. Models can either be process-based, process-oriented or empirical, in descending order of applicability. Process-based models seek to describe phenomena based on the exact physical processes and are often widely applicable. Process-oriented models approximate these physical processes using some fit parameters or crude representation of these processes and are thus somewhat less exact. Empirical models commonly use relations in which observations are connected based on observed correlations, rather than a physically accurate description of processes. Most process-oriented or process-based use some empirically developed formulas, but the models as a whole seek to describe the breaching process step by step, whereas empirical models neglect the actual processes between in- and output.

Empirical models are only to be used in cases, which are strongly similar to the case based on which the relations were derived and where all assumptions in the empirical model still hold. Based on this classification, the empirical models are listed in Table 2.1 and the process-based and process-oriented models are included in Table 2.2 (West et al., 2018).

Another important classification of models is based on dimensionality. Breach flow, the resulting turbulence and erosion are complex processes, imposing loads, which vary both in time as well as in all three spatial dimensions. Modelling these phenomena is commonly done by reducing the spatial dimensionality of the erosion model. The simplest models are zero-dimensional, depending only on time. The first three-dimensional models are currently in development, among which a three-dimensional version of DLBreach, which has been identified as a promising model for future development, although current versions are sensitive to model instabilities and lack information on programmatic errors (West et al., 2018).

Most of the advanced models use a 2d-2d approach, in which erosion first occurs vertically over a predefined horizontal plane (often assumed to be between 1 and 10 metres wide) and is followed by lateral erosion over the complete cross-section of the dike (d'Eliso, 2007, Morris, 2011, Visser, 1998). The initial lateral erosion is related to the vertical erosion through an assumed ratio between horizontal and vertical erosion velocities or is neglected and replaced by an initial breach width. The 2d-2d simplification saves enormous computation effort, and still models the breaching process well for three reasons.

First, local subsidences along the dike attract larger flow rates, limiting the width of the area along which the grass cover fails and making an initial breach width physically explainable as the typical width of such a local weak spot. Second, the lateral erosion of the breach only occurs if a sufficiently deep breach has formed to allow breach flow to exceed the critical shear stress along the side slopes of the eroded area. An increase in breach height therefore results in an increase in lateral growth, making it a reasonable assumption to neglect breach widening during breach formation and considering it a subsequent (separate) process. Finally, as the horizontal erosion through the clay cover much slower than the erosion of the sand, the neglected width increase of the breach is fairly small. An initial breach width is assumed to compensate for this underestimation. The assumptions in the breach morphology column of Table 2.2 indicate the dimensionality of the model used.

Depending on the load case, parameters in the empirical models (Table 2.1) differ. The parameters for a breach initiated by wave overtopping are indicated by OT, whereas breach parameters for piping are followed by P. The erodibility of materials is qualitatively indicated by HE, ME or LE, representing high, medium and low erodibility, respectively.

Table 2.1: State-of-the-art Empirical Breach Models

Parametric model	Time to Breach formation	Average breach width	Side slopes	Peak Outflow	No. case studies	Case types
Froehlich (2008)	$t_f = 0.00176\sqrt{\frac{V_w}{g h_b^2}}$	$\overline{B} = 0.27 k_0 V_w^{\frac{1}{3}}$ Where: $k_0 = \begin{cases} 1.3, & \text{OT} \\ 1.0, & \text{P} \end{cases}$	$z = \begin{cases} 1.0, & \text{OT} \\ 0.7, & \text{P} \end{cases}$	Not included	74	Overtopping, overflow and internal erosion of homogeneous and composite dikes, both natural and man-made breaches
Zhang et al. (2009)	$\frac{t_f}{t_r} = C_5 (\frac{h_{cd}}{h_r})^{0.654} (\frac{V_w^1/3}{h_w})^{1.246}$ Where: $C_5 = b_5$ $b_5 = \begin{cases} 0.038, & \text{HE} \\ 0.066, & \text{ME} \\ 0.205, & \text{LE} \end{cases}$	$\frac{\overline{B}}{h_b} = 5.543 (\frac{V_w^{1/3}}{h_w})^{0.739} e^{C_3}$ Where: $C_3 = b_4 + b_5$ $b_4 = \begin{cases} -1.207, & \text{OT} \\ -1.747, & \text{P} \end{cases}$ $b_5 = \begin{cases} -0.613, & \text{HE} \\ -1.073, & \text{ME} \\ -1.268, & \text{LE} \end{cases}$	Height included in breach width relation	$\frac{Q_p}{\sqrt{g V_w^{5/3}}} = 0.133 (\frac{V_w^{1/3}}{h_w})^{-1.276} e^{C_4}$ Where: $C_4 = b_4 + b_5$ $b_4 = \begin{cases} -0.788, & \text{OT} \\ -1.232, & \text{P} \end{cases}$ $b_5 = \begin{cases} -0.089, & \text{HE} \\ -0.498, & \text{ME} \\ -1.433, & \text{LE} \end{cases}$	75	Overtopping, overflow and internal erosion of homogeneous and composite dikes, both natural and man-made breaches
Froehlich (2016a,b)	$t_f = 60\sqrt{\frac{V_w}{g h_b^2}}$	$\overline{B} = 0.23 k_0 V_w^{\frac{1}{3}}$ Where: $k_0 = \begin{cases} 1.5, & \text{OT} \\ 1.0, & \text{P} \end{cases}$	$z = \begin{cases} 1.0, & \text{OT} \\ 0.6, & \text{P} \end{cases}$	$Q_p = 0.0175 k_0 k_H \sqrt{\frac{g v_w h_w h_b^2}{\overline{w}}}$ Where: $k_0 = \begin{cases} 1.85, & \text{OT} \\ 1.0, & \text{P} \end{cases}$ And: $k_H = \begin{cases} 1, & h_b < 6.1 \\ (h_b/6.1)^{1/8}, & h_b > 6.1 \end{cases}$	2016a: 111 2016b: 41	Overtopping, overflow and internal erosion of homogeneous and composite dikes, both natural and man-made breaches

Table 2.2 describes the assumptions and methods used in the more complex process-based models. Formulas are not directly presented here. Instead, references to the original publications are included and a short summary of various formulations and assumptions is included.

Table 2.2: State-of-the-art Process-Based Breach Models

Process-based model	Breach morphology	Flow over Dike	Transport equation	Geomechanics of breach side-slopes	Limitations	Main publications
BRES	YZ: Trapezoidal XZ: Horizontal channel	Weir formula and Bélanger	Various equations for cohesive and non-cohesive soils	Simple slope stability	Simplified slope stability calculations No effect of waves considered	Visser (1998) Zhu (2006)
AREBA	YZ: Effective shear stress dependent XZ: Exner equation and soil wasting	Variable weir formula	Various equations for cohesive and non-cohesive soils	Simple slope stability	Predefined breach development Does not model seepage flow	van Damme et al. (2012)
FIREBIRD	YZ: Variable trapezoidal XZ: Exner equation	Weir formula	Parametric relations for headcut advance, bottom and lateral erosion	Breach side slope erosion	Predefined breach development	Gyr and Kinzelbach (2003) Wang et al. (2006)
WinDAM	YZ: Headcut development and migration XZ: Rectangular or trapezoidal	Weir formula	Parametric relations for headcut advance, bottom and lateral erosion	Breach side slope erosion	Predefined breach development Does not model seepage flow or slope stability Model needs soil erodability input value Can only model overtopping	Temple et al. (2005) Hanson et al. (2005a,b) Temple et al. (2006)
D'Eliso	YZ: Headcut development and migration XZ: Rectangular to trapezoidal	Wave overtopping and/or overflow – Bernoulli equation	Formulas for erosion rate and headcut advance	Grass cover, clay cover, sand core and breach slope stability	Limited understanding of 2D simplification Instability of non-cohesive soils excluded Assumption on ratio vertical and horizontal erosion rate	d'Eliso (2007)
EMBREA	YZ: Effective shear stress dependent XZ: Exner equation and soil wasting	Variable weir formula and 1D Steady non-uniform flow equations	Various equations for cohesive and non-cohesive soils	Slope and core stablity and zones of variable erodibility	Does not model scour holes or seepage flow	Morris (2011)
DL Breach (3D)	Calculated from resulting bed change from suspended and bed-load equations	3D RANS equations using finite-volume method.	3D non-equilibrium transport equations of suspended-load and bed-load	Not included	Large computational requirements associated with running the model Does not model slope stability Focuses more on flood routing rather than breach development	Marsooli and Wu (2014)
Zhong et Al. (2017)		Weir formula		Limit equilibrium method for slope stability	Only considers headcut erosion	Zhong et al. (2017)

2.4. Discussion of existing model performance

The models described in the previous subsection cover a wide range of approaches to modelling dike breaching. This subsection describes the performance of both the empirical as well as the process-based models on various aspects of the breaching process and identifies the shortcomings in current breach models. Typically desired qualities in a process-based breach model include: an improved prediction over empirical models, applicability on a wider range of situations, short computation time (limited to an hour at most) and little input data required.

Empirical models are evaluated collectively, as these models are not based on physical processes, but rather on data from experiments or case studies, resulting in similar strengths and weaknesses. Empirical models are based on the assumption of a single failure mechanism and return (a confidence interval of) the time to failure and breach size, requiring minimal input data, such as cross-sectional profiles of the dike and a volume of retained water. The main shortcoming in empirical models from a scientific viewpoint is that no parameter sensitivities can be assessed, rendering these models useless for safety optimisation of dike designs. As empirical models only provide reliable output for (strongly) similar cases to the ones they were based on, their reliability for flood scenario analysis is limited.

The most relevant process-based and process-oriented models are evaluated separately, as each of the models includes or excludes processes, resulting in different strengths and weaknesses. Generally, these models require more input data, but are more accurate, suitable for paramater sensitivity analyses and (depending on the formulas used) widely applicable (West et al., 2018).

A relatively simple and fast model is AREBA (van Damme et al., 2012). The simplified inclusion of surface, headcut and internal erosion modules makes it a useful model for flood risk analysis, when many calculations are needed. AREBA is limited to modelling breaching in homogeneous embankments due to overflow and piping and uses an empirical formula for the time-to-failure of a grass cover in overflow. Geotechnical stability is only considered in case internal erosion (piping) is selected as failure mechanism. Input of the model is comparable to the empirical models; the only additional parameter required is the soil erodibility, for which estimates are given in the model publications.

A second, more detailed model is EMBREA, which models the same failure modes as AREBA, but does so in multi-layered embankments, with different soil erodibility characteristics (Morris, 2011). The output options include visualisations and probabilistic distribution of results, making EMBREA useful for sensitivity analysis. The added options included in EMBREA result in larger computational effort and most importantly, require significantly more input data to provide accurate results. During lateral breach growth, slope stability is used alongside surface erosion to determine the speed of breach widening (Morris, 2015, West et al., 2018).

d'Eliso (2007) identified various general shortcomings in breach models, of which the most important are the lack of understanding of the ratio between vertical and lateral erosion during lateral breach growth and the stability of non-cohesive sub-layers during breach formation. The recent DL Breach 3D model is the first model to apply the three-dimensional RANS equations to model breach flow, but does not include three-dimensional erosion yet (Wu, 2016).

2.4.1. Conclusion

Current models predicting breach formation are based on various assumptions and apply different erosion methods (surface erosion, headcut erosion or a combination of the two). All models simplify, omit or empirically assess effects. The most notable shortcomings are listed below, after which the improvements to these processes in the proposed model are given.

Various processes are only described on an oversimplified level, such as the scouring of the sand core during headcut erosion, the ratio between horizontal and vertical erosion velocities and the flow regime in the scour pit. Most attempts to model these effects apply empirical relations, a computationally efficient process-oriented method has not yet been presented.

Three other shortcomings have been identified throughout the process-based models: First, the models are not directly comparable, as various relations between erosion of embankment construction material and the flow velocity are applied. Based on a stress balance or energy balance, the relations either have the form of $E \sim u^2$ or $E \sim u^3$, but the use of dimensional fit parameters and the varying influence of roughness in different flow regimes in this relation makes the applied exponents range between 0.5 and 3. Second, all current models overestimate the erosion of granular material at high flow velocities. Erosion of non-cohesive material through formulations valid for a Shields parameter (Θ) smaller than one (see Equation 2.16) , whereas for most breach flow situations, much larger Shields parameters apply ($\Theta > 3$) and a different erosion formula is more applicable (Bisschop, 2018, van Rhee, 2010). Finally, the stability of headcuts is commonly modelled as a rigid beam, which is an unsuitable method to model soil, especially for non-cohesive core material. These simplifications make these models are not applicable for design, as the representation of physical processes is poor and the sensitivities to input parameters are limited.

$$\Theta = \frac{\tau_b}{gD(\rho_s - \rho_w)} \tag{2.16}$$

The BRAM model developed as a part of this research applies a process-oriented method to describe the erosion of granular core material, based on a calculation of bed shear stresses along the complex scour hole geometry and an erosion formula applicable to the high flow velocity erosion regime. The proposed method adopts a geotechnical slope stability criterion, rather than model the behaviour of the soil as a rigid beam. The stability criterion is used to further specify lateral and vertical breach growth explicitly, rather than specifying vertical growth and an empirical relation between vertical and lateral growth. Recommended values to use as input to the model are posed to apply on cases where limited data has been gathered.

3

Physical Modelling

To verify that the physical processes described in Section 2.2 represent the actual erosion process well and to validate the model equations, outlined presented in Chapter 4, various large-scale tests on the erosion of dikes are considered. One small-scale test is also used to assess the validity of the model on a smaller scale.

Scale effects are quite relevant in breach modelling, as the importance of different erosion processes and thus the applicability of a model on various scales differs: Headcut erosion appears quite similar to surface erosion on a small scale, as the height of a headcut does not scale along with the invert level of the dike, causing only a single-step headcut to form on a small-scale test (see Figure 3.1d), of which the erosion profile seems quite similar to slope steepening as a result of surface erosion (Figure 3.1c. In large-scale tests, headcut erosion is known to form form multi-step headcuts on various weak spots, appearing significantly different to surface erosion, as multiple cascades develop, as shown in Figure 3.1b.

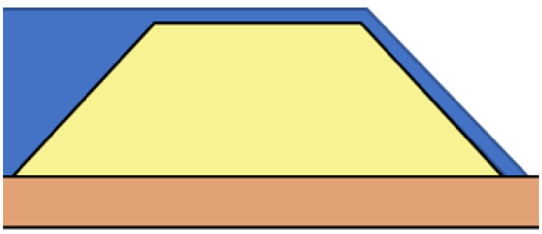

(a) Overflow on initial dike profile

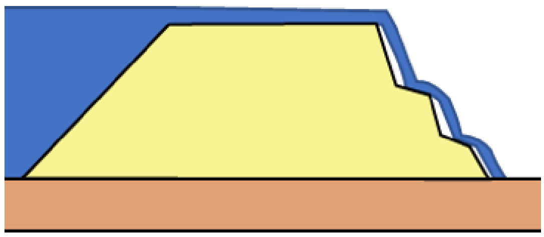

(b) Multi-step headcut formation

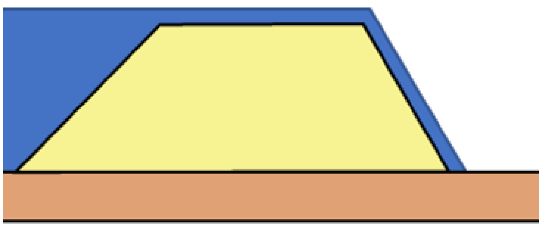

(c) Surface erosion, slope steepening

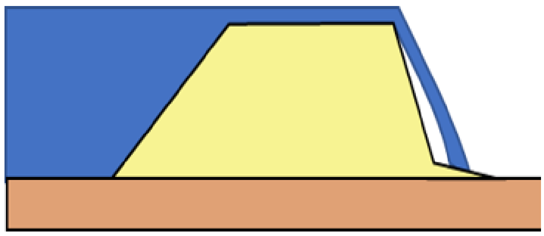

(d) Single-step headcut formation

Figure 3.1: Erosion of land-side slope through various erosion processes

Scaling also poses challenges in representing physical behaviour of the construction material of the dike in small-scale tests. The use of extremely small grain sizes in a scale test to represent sand on a full-scale dike results in cohesion effects in the small-scale model, which are not found in the full-scale granular material. A common solution is to adapt the flow regime, resulting in an equal Shields parameter (Equation 2.16) and Reynolds number (a measure of turbulence in the flow, as shown in Equation 3.1) as observed in the full-scale situation.

$$Re = \frac{uL}{\nu} \tag{3.1}$$

In which:

- u is a representative flow speed
- L is a characteristic length scale, normally assumed to be equal to the hydraulic perimeter P
- ν is the dynamic viscosity of water $(= 10^{-3}) at T = 20°C)$

Section 3.1 describes the overflow tests conducted in Flood Proof Holland, Delft in January 2019. Section 3.2 discusses the overtopping and overflow experiments performed in November 2015 in the Wijmeerspolder, near Schellebelle, Belgium. The third test, discussed in Section 3.3 elaborates upan the breach growth experiment in 't Zwin, on the border of the Netherlands and Belgium in October 1994. The final experiment, discussed in Section 3.4, tests the migration of headcuts in small-scale embankments in a flume setup in the Delft University of Technology hydraulic test facility.

3.1. Flood Proof Holland - Overflow erosion tests

In January 2019, overflow erosion tests were performed in the Flood Proof Holland testing facility of Delft University of Technology. The purpose of the tests was to determine the erodibility of sand, silt and clay. These tests of these tests are used to validate the cover erosion method in Section 4.4.

3.1.1. Test setup

The embankment tested in Flood Proof Holland consists of three sections of different material. The dike body is normally enclosed by a grass cover, with a turf layer of 10 centimetres. For testing, the enclosing layer has been removed. The tested surface therefore consists of the core material and (cohesive) cover, which is visualised in Figure 3.2 and can be described for each section as follows (Yagisawa, 2019a). Note that Table 3.2 provides (amongst other geotechnical data) further specification of the granulometry of the material.

- Section 1: The first section of the tested embankment consists of a fine sand core, covered by a layer of lean clay (Unified Soil Classification System (USCS) class CL) (Dutch erosion class 3: small resistance against erosion) with a thickness of 0.30 metres. On the waterside slope toe of the embankment a toe filter is present. The hydraulic permeability of the toe filter is an order of magnitude larger than the dike core.
- Section 2: The second section of the embankment consists entirely of homogeneous fine sand (USCS) class SP).
- Section 3: The third section of the embankment consists of silt (USCS class ML), which contains approximately 40 percent sand, 40 percent silt and 20 percent clay (by mass, based on grain size).

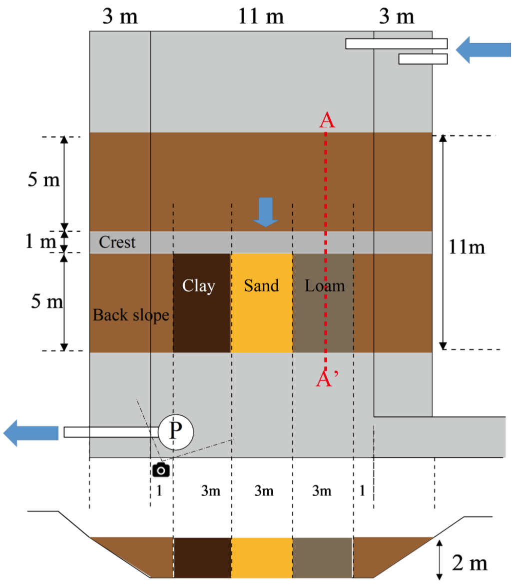

Figure 3.2: Plan view Flood Proof Holland overflow tests

The dike was specifically constructed for this test and its layers are thus fairly homogeneous, although it must be noted that some mixing occurred between the sand core and clay cover in the clay test section.

On each of the test sections, a flume of 1.0 metres in width was created, and overflow was initiated by raising the water level in the pit behind the test section, using the pump system depicted in the top right corner of Figure 3.2. By controlling the water level in this pit using this fixed pump system and an additional pump to achieve higher discharge, the overflow rate and test duration as presented in Table 3.1 were achieved during the tests. Figure 3.3 is a photo of the prepared test sections, taken from the viewpoint marked by [📷] and the dot-dash line in Figure 3.2.

Table 3.1: Results of geotechnical labwork

Test material	**Overflow rate [l/m/s]**	**Maximum flow speed [m/s]**	**Test duration [min]**
Lean Clay (CL)	Initially 40, increased to 70	2.5	130
Silt (ML)	Constant at 70	3.0	60
Fine sand (SP) 1	Constant at 20	1.7	2
Fine sand (SP) 2	Constant at 20	1.7	2

Figure 3.3: Viewpoint Flood Proof Holland overflow test sections

3.1.2. Soil sampling

To appropriately quantify the behaviour of the embankment materials, various soil parameters were determined through lab testing of samples. These samples were taken by removing the turf cover close to the tested sections, pressing hollow tin cans (diameter 7.3 cm, height 10.6cm) into the exposed test material and subsequently excavating the samples.

Due to temporarily raised water levels, disturbances caused by the installation of drainage after the completion of the dike, and researchers walking on the dike after the tests, some of the soil liquefied on the lower end of the slope (approximately 2.0 metres). It was decided to take all soil samples above the disturbed area, between 0.1 and 2.5 metres from the crest. Figure 3.4 shows the locations of all samples. The lengths indicated along the slope represent approximated heart-to-heart distances of the measurements.

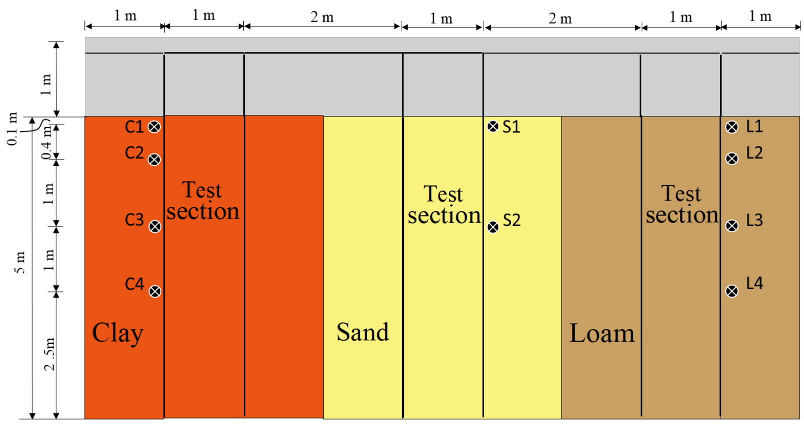

Figure 3.4: Sampling locations Flood Proof Holland overflow tests

3.1.3. Results - Erosion

The flow velocity was measured on four locations along the land-side slope of the levee. The erosion was measured on various locations on the land-side slope, using simple rods, resting on the remaining soil. The observed erosion rates differed strongly between the test sections, ranging from minor damage in the lean clay section after 2 hours and 45 minutes of overflow, to severe erosion of the sand section after only three minutes. In both the silt and sand section, slope steepening was observed. In the sand section, the formation of headcuts was already observed, even at a relatively low overflow rate (20 l/m/s) and short test duration. The resulting vertical erosion on each test section is shown in Figures 3.5a through 3.5c. The vertical coordinates indicate the distance from the crest [cm]. The erosion is shown in the heat maps [cm].

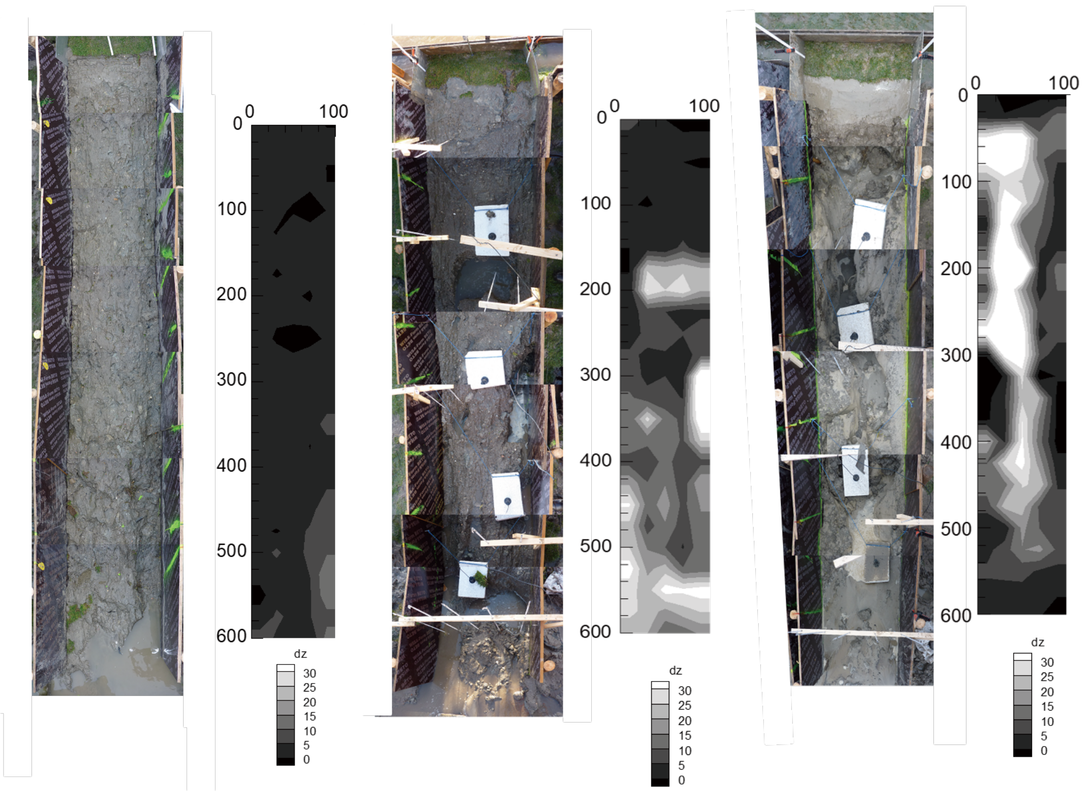

(a) Lean clay test section
($t \approx 2:45$ h, $Q = 50$ l/m/s)

(b) Silt test section
($t \approx 1:00$ h, $Q = 50$ l/m/s)

(c) Sand test section
($t \approx 2$ min, $Q = 20$ l/m/s)

Figure 3.5: Vertical erosion observed after erosion tests in Flood Proof Holland

The erosion is smaller for materials with increasing clay content. Contrary to commonly assumed, especially in the non-cohesive fine sand, headcuts developed. In the silt section, the erosion was somewhat slower, but still, slope steepening and headcut initiation was observed. In the clay section, headcut initiation was not observed in the undisturbed flow region, but some slope steepening was found along the boards restricting the flow.

3.1.4. Results - Geotechnical

Soil samples taken from the test sections were tested in the geotechnical lab of Delft University of Technology. A complete report of the test procedures followed, observations, results and interpretation can be found in Appendix A. Table 3.2 provides an overview of the soil parameters for the three soil types found on the test sections. A short summary highlights the most notable results.

Table 3.2: Results of geotechnical lab work of samples taken from FPH test embankment

Parameter	Unit	Sand	Densified sand	Silt	Lean clay
Grain sizes					
Lutum fraction ($< 2\mu m$)	$[-]$ or $[\frac{g}{g}]$	0	0	0.021	0.034
Fraction $< 63\mu m$	$[-]$ or $[\frac{g}{g}]$	0.0079	0.0079	0.43	0.68
D_{50}	$[\mu m]$	198	198	119	37
D_{10}	$[\mu m]$	108	108	21	7.4
$\frac{D_{60}}{D_{10}}$	$[-]$ or $[\frac{\mu m}{\mu m}]$	2.06	2.06	6.35	7.79
State indicators					
Plastic limit	$[-]$ or $[\frac{g_{water}}{g_{clay}}]$	[N/A]	[N/A]	0.18	0.20
Liquid limit	$[-]$ or $[\frac{g_{water}}{g_{clay}}]$	[N/A]	[N/A]	0.23	0.28
Plasticity index	[%]	[N/A]	[N/A]	5	8
Minimum porosity	$[-]$ or $[\frac{cm^3}{cm^3}]$	0.40	0.40	[N/A]	[N/A]
Maximum porosity	$[-]$ or $[\frac{cm^3}{cm^3}]$	0.52	[N/A]	[N/A]	[N/A]
In situ state					
Mean bulk weight sample	$[\frac{kN}{m^3}]$	12.9	16.1	16.3	16.8
In-situ porosity	$[-]$ or $[\frac{cm^3}{cm^3}]$	0.50	[N/A]	0.42	0.56
In-situ Volumetric water content	$[-]$ or $[\frac{cm^3}{cm^3}]$	0.23	[N/A]	0.31	0.52
In-situ Degree of Saturation S_w	$[-]$ or $[\frac{cm^3}{cm^3}]$	0.47	[N/A]	0.75	0.93
Consistency index	$[-]$	[N/A]	[N/A]	0.8	-0.625
Physical parameters					
Consolidation coefficient C_v	$[\cdot 10^{-8}\frac{m^2}{s}]$	[N/A]	[N/A]	171	4.94
Unloading/reloading C_{ur}	$[\cdot 10^{-8}\frac{m^2}{s}]$	[N/A]	[N/A]	178	77.5
Permeability (undisturbed)	$[\frac{m}{s}]$	[N/A]	$5.05 \cdot 10^{-5}$	10^{-7}	10^{-10}
Permeability (in situ)	$[\frac{m}{s}]$	[N/A]	$5.05 \cdot 10^{-5}$	$1.87 \cdot 10^{-6}$	$2.35 \cdot 10^{-5}$
Internal friction angle	[°]	31.6	34.6	41.3	31.0
Cohesion	$[kPa]$	1.3	1.8	1.8	7.5

Whereas the report provided by the contractor, who constructed the test embankment, referred to the silt and lean clay mixtures as "loam" and "erosion class EC3 clay" respectively, this report refers to these materials as "silt" and "lean clay", following the USCS classification system. The small lutum fraction and relatively large sand content, combined with the relatively low plasticity indices (which are a result of the aforementioned two observations) show that the materials are far more sensitive to changes in their water content than construction quality EC2 or EC1 clay, which have a minimum plasticity index of 18% (Cirkel et al., 2018).

The porosity of the sand is quite high, which is explained by the small coefficient of uniformity ($\frac{D_{60}}{D_{10}}$). For values of this parameter smaller than 4, the sand has is poorly graded, which means there is a lack of variation in particle sizes for small particles to fill pore space, resulting in large porosity.

The in-situ water content varied strongly between the materials. The samples were taken outside the overflow strips, so the water contents were not influenced by the overflow and thus indicate the state of the soil before overflow occurred. Due to precipitation, the loam section was close to a liquid state, whereas large areas on the clay section were already fluid before the test had started (indicated by the negative consistency index).

The consolidation coefficients of the silt and lean clay were somewhat higher than normally expected (in the order of magnitude of 10^{-6} where one would expect 10^{-8} to 10^{-7}). This is the result of measurement inaccuracies at the start of the measurement. If the initial deformation of the sample is relatively large, the time until 50% (t_{50}) of deformation is relatively short, resulting in an overestimation of the C_v. (Further explanation regarding this calculation can be found in Appendix A. The unloading/reloading coefficient for clay was significantly smaller, as one would expect for a poorly permeable soil, whereas the C_{ur} for the silt was somewhat higher. This drainage behaviour of silt therefore seems dominated by the relatively large fraction of coarse (sandy) material.

The tests on all samples appear to have been in drained loading regime (as all values of ξ are below 1.0, see Table A.10). An attempt to test the undrained behaviour of clay resulted in unsatisfactory results, as the applied shear strain rate was too small to achieve undrained conditions.

3.1.5. Conclusions

From the tests performed at the Flood Proof Holland facilities in Delft, the following conclusions are drawn:

Material transitions can initiate headcuts
The most notable observation regarding the erosion during the Flood Proof Holland experiments was the initiation of headcuts in not only the silt, but also the sand section. Analysis of the erosion of the sand as a function of time showed an interesting pattern: whereas headcuts normally migrate towards the dike crest, the multi-step headcut profile, which was observed in both sand erosion tests (although more pronounced in the first test) was initiated at the crest and formed new steps in downward direction. The initiation of a headcut is most commonly defined as the development of a certain height of (near-)vertical cliff. This cliff height was reached at the crest of the dike first, as the grass and clay cover on the crest almost fully prevented erosion, resulting in a near vertical cliff at the beginning of the test section (see Figure 3.6). A similar cliff was found at the dike toe, at the transition from erodible material to concrete floor plates. The sand remained stable in near-vertical cliffs, up to a height of 25 centimetres.

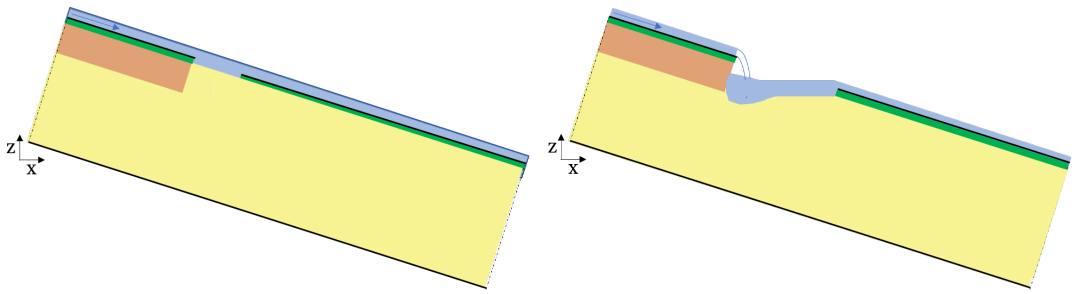

(a) Pre-existing material transition (b) Headcut formation

Figure 3.6: Visualisation of headcut formation due to differential in surface erodibility near dike crest at Flood Proof Holland

If a sufficiently large area of erodible material is exposed, a multi-step headcut develops
In both the silt and sand tests, the formation of a first headcut was followed by the formation of new headcuts downstream of the first. This is the result of the adaptation in flow regime that follows from the first headcut: a reduced hydraulic friction results in higher flow velocities downstream, resulting in flow detachment and locally increased erosion. Subsequently, a new headcut forms and the process is repeated downstream. Note that this phenomenon is more pronounced for a more erodible material and is unlikely to occur at all in a realistic case, where a grass cover is still present downstream, severely limiting the erosion.

Local variation in erosion is significant for both cohesive and non-cohesive soils and increases with increasing erosion depth
Although the test sections were relatively narrow at a width of approximately 1.0 metres, with erosion measurement rods as little as 20 centimetres apart, the measured erosion rates during all tests varied by more than 100% (of the smallest value) between neighbouring measurement points. The variation between measurements increased with an increase in maximum erosion. In the clay section, where the smallest erosion was measured, the variation was relatively small, however, at the dike toe, where the largest clay erosion occurred, the variation was still significant (10 centimetres of depth difference between two measurements). This indicates that eroded areas attract more flow (exhibit a smaller hydraulic friction), resulting in more erosion: a positive feedback mechanism.

3.2. Wijmeer test - Overflow and wave overtopping experiments

In November 2015, a combination of overflow and wave overtopping tests were performed on the levee of the Wijmeerspolder 2, along the Schelde river in Belgium. The primary objectives of the tests were to determine by what hydraulic conditions during overtopping and overflow the grass cover would fail (Bakker and Mom, 2015b). These tests are used to validate the equations used to model grass and clay cover failure in Sections 4.3 and 4.4.

3.2.1. Test setup

The levee in the Wijmeerspolder is a symmetrical dike with a relatively steep slope of 1 : 1.9 (test section III) to 1 : 1.8 (test section I) on both the water and landside Bakker and Mom (2015a). The dike is made up of a sand core, a clay layer (of which the thickness is reported to be 0.6 metres) and a grass cover. A gravel maintenance road is present on the crest of the dike.

Overtopping

The test sections used for the overtopping and breaching tests were 4.0 metres wide, laterally confined by wooden boards, which have been placed on the slope on wooden piles (approximately 1.0 metres in length). A geotextile was placed on the crest, covering the maintenance road, but leaving the grass on the crest and the transition between the crest and the landside slope exposed. For the overtopping experiment, the test section was subdivided by paint markings in sections of a width and length (along the slope) of 1.0 metres to accurately determine the location of damages. Visual inspections were carried out both before and during the test phases, to assess the development of damages.

The tests were performed using an overtopping simulator filled by a frequency adjustable pump. The time-averaged overtopping discharges for the first test section are given in Table 3.3. The second test section was tested at 25 l/m/s, the overtopping rate at which the cover failed for the first test.

Table 3.3: Overflow test phases Wijmeerspolder

Test	Overtopping discharge per unit width [l/m/s]	Test duration [min]	Wave volume [l/m]
OT-01	5.0 (1.0)[1]	24	113
OT-02	5.0	120	349
OT-03	10	120	672
OT-04	25	120	1662
OT-05	50	12	2230

Surf boards and paddle wheels were used to measure local flow depth and flow velocity, respectively. The complete test setup is depicted in Figure 3.7. All indicated overtopping rates are time-averaged. Peak discharges therefore were significantly larger, with a volume of water in an overtopping wave as indicated by Table 3.3.

[1] Due to the low frequency of overtopping waves for an overtopping discharge per unit width of 1.0 l/m/s, this test was performed at an increased overtopping discharge per unit width of 5.0 l/m/s, reducing the duration of the test by the same factor to 24 minutes.

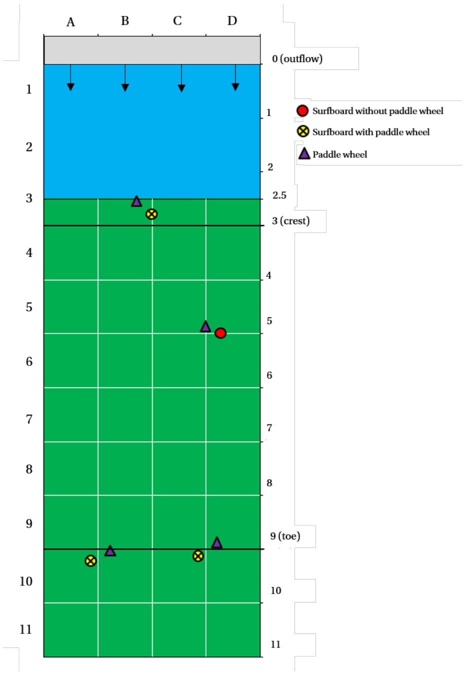

Figure 3.7: Test and measurement setup overtopping test Wijmeerspolder

Overflow

Three overflow tests were performed on test sections with a similar setup as the overtopping experiments, however, the flow was now continuous, rather than varying, to represent overflow instead of wave overtopping. The flow rates were selected, such that the (mean) shear stresses were equal between the overtopping and overflow tests. The test section width was reduced to 2.0 metres, rather than the 4.0 metres used in the overtopping tests to achieve sufficient discharge capacity.[2]

The first test was performed on the unaltered slope with a grass cover, incrementally increasing the flow rate. Table 3.4 shows the flow increments used in the tests.

Table 3.4: Overflow test phases Wijmeerspolder

Test	Overflow discharge per unit width [l/m/s]	Test duration [min]
OF-01	10	120
OF-02	25	120
OF-03	50	120
OF-04	85	120
OF-05	125[2]	60
OF-06	165[2]	60

A second test was performed on a test section where the grass cover was removed, exposing the clay. The overflow rate was fixed at 33 l/m/s. The third test was performed on the slope section with the grass cover still in place, at a constant overflow discharge of 165 l/m/s.

[2]Note that for the test at 125 and 165 l/m/s, the test section width was reduced again, in this case to 1.0 metres, to achieve sufficient overflow discharge, using the available pumping capacity.

3.2.2. Results - Erosion

In this subsection, the resulting damage from the overtopping and overflow tests are described. For each of the tests, a qualitative description of the observed damages is given, supported by various figures of the damage at critical times.

Overtopping

Two wave overtopping tests were performed, during which the flow layer thickness, flow velocity and resulting damages at various overtopping discharges were determined. It was observed that even for relatively small (time-averaged) overtopping discharges, flow detachment occurred, resulting in local jetting pressure on the grass cover, rather than a shear load due to surface-parallel flow.

In both tests, significant local erosion was observed at the location of wave impact on the slope. The following figures show the slope after only minor overtopping (Figure 3.8a) and after failure at 1 hour and 27 minutes of overtopping at an average discharge per unit width of 25 l/m/s (Figure 3.8b). The photos were taken from the test at continuous overtopping discharge.

(a) Overtopping test section before test ($t = 0$, $q_{avg} = 25$ l/m/s)

(b) Overtopping test section after test ($t = 1:27$h, $q_{avg} = 25$ l/m/s)

Figure 3.8: Damage observed after continuous overtopping tests at the Wijmeerspolder

In Figure 3.8a, some irregular sections on the grass cover can be distinguished in the lower centre and top left sections of the slope. The largest erosion was found at the location of wave impact, near the initial weak spot in the top left. A steep headcut erosion downstream of the wave impact location can be observed.

The other overtopping test section, at which the overtopping discharge was incrementally increased, failed at a similar duration of loading with the maximum load, while this test section had at this point already been subjected to a simulated 6 hours of incrementally increasing overtopping discharges. For a full assessment of the development of the damages, the following figures show the second test section before overtopping (Figure 3.9a) and after testing up for a simulated 6 hours and a maximum time-averaged discharge per unit width of 10 l/m/s (3.9b).

(a) Overtopping test section before test ($t = 0$, q_{var})

(b) Overtopping test section after three discharge increments ($t = 6:00$ h, $q_{avg} = 10$ l/m/s)

Figure 3.9: State of the slope during incrementally increasing overtopping tests at the Wijmeerspolder

After these gradually increasing overtopping loads on the test section, the damage quickly developed during the test at 25 l/m/s. The following figures present the damages after approximately 1 hour (Figure 3.10a, marked as the moment of failure) and after the full test duration of 2 hours (Figure 3.10b).

(a) Overtopping test section at failure ($t = 7:00$ h, $q_{avg} = 25$ l/m/s)

(b) Overtopping test section after completion of the discharge increment ($t = 8:00$ h, $q_{avg} = 25$ l/m/s)

Figure 3.10: Damage observed after incrementally increasing overtopping tests at the Wijmeerspolder

Comparing the two tests, specifically Figures 3.8b and 3.10b, it becomes clear that a headcut is initiated near the location of wave impact, both for a slope which has a weak spot here, as for a slope which does not have any visible weak spot in this location. The location of a maximum load is therefore assumed to dominate the location of headcut initiation over the location preexisting weak spots in the slope in case of headcut initiation by overtopping.

Overflow

In the incrementally increasing overflow test, damage was far less significant than in the wave overtopping tests. Some minor erosion was observed where rocks and other material in the slope disturbed the flow. Whereas the overtopping test showed the most damage where the overtopping flow made contact on the slope, the overflow tests showed more significant damages around objects and slope transitions, such as near the toe of the dike. Figures 3.11a and 3.11b show the state of the slope after the 10 and 125 l/m/s overflow tests. The grass cover did not fail due to these overflow tests.

(a) Overflow test section after first test ($t = 2:00$ h, $q_{max} = 10$ l/m/s)

(b) Overflow test section after fifth test ($t = 10:00$ h, $q_{max} = 125$ l/m/s)

Figure 3.11: Damage observed after incrementally increasing overflow tests at the Wijmeerspolder

A second overflow test, using an increased flow rate showed similar results. At an overflow rate of 165 l/m/s (where the flow velocity over the slope exceeded 3.0 m/s), some weak spots around debris in the slope showed minor local erosion. This caused the slope to become somewhat irregular, however, the grass cover did not fail due to this overflow rate. In Figure 3.12b some rubble material can be seen in the middle of the slope (between markers 9 and 10). This became exposed during the overflow test. After two hours, the test was stopped.

(a) Overflow test section after final test ($t = 12:00$ h, $q_{max} = 165$ l/m/s)

(b) Local damage after final overflow test ($t = 12:00$ h, $q_{max} = 165$ l/m/s)

Figure 3.12: Grass cover failure after incrementally increasing overflow tests at the Wijmeerspolder

To assess what the effect of the grass cover on the erosion resistance of the cover was, a third overflow test was performed on an adjacent test section (1.0 metres wide) where the grass cover was removed. This section was subjected to an overflow discharge of 33 l/m/s (a factor 5 less than the maximum overflow rate withstood by the grass cover). Without the grass cover, this overflow rate lead to failure of the clay layer and the formation of a headcut in the middle of the test section after 49 minutes.

As shown in Figure 3.13a, the slope was irregular before the experiment started, leading to significant flow disturbances and local erosion. A steep headcut developed, soon exposing the granular core material. At this time the clay layer was considered to have failed and the test was stopped. Similar to the clay test section in Flood Proof Holland, Delft, the transition at the top, at the first point where erodible material was exposed, (in this case a transition from the grass cover to exposed clay) eroded quite rapidly. The most notable erosion and headcut formation was found at the most irregular part of the slope. Figure 3.13 shows the slope before and after the test.

(a) Clay test section before overflow ($t = 0$, $q = 33$ l/m/s)

(b) Resulting erosion overflow test ($t = 49$ min, $q = 33$ l/m/s)

Figure 3.13: Headcut formation in clay due to constant overflow tests at the Wijmeerspolder

In a final attempt to bring the grass cover to failure due to continuous overflow, the second grass test section was revisited after the clay erosion test. At a discharge of 165 l/m/s, the grass cover again did not fail. However, due to leakage of the overflowing water under the wooden boards, the adjacent exposed clay cover test section was eroded further. The erosion of the exposed clay section expanded to the grass test section after approximately 5 minutes, leading to undermining of the grass cover. The flow rate (a factor 5 larger than the flow rate, which originally brought the clay layer to failure) soon expanded the headcut to a height of over 1.0 metre over the width of both the clay and grass section. Figure 3.14a shows the grass and clay sections before the overflow tests. Figure 3.14a shows the damage after all the tests (in summary: a fist test on the grass cover, a test on the exposed clay cover and a second test on the grass cover). [1]

[1] For a complete picture of the development of the damages during the test in sequence, one should look at Figure 3.14a, then Figure 3.13b and finally Figure 3.14b.

(a) Grass test section before overflow ($t = 0$, $q = 165$ l/m/s)

(b) Resulting erosion overflow test ($t = 2:05$ h, $q = 165$ l/m/s)

Figure 3.14: Headcut formation through grass due to constant overflow tests at the Wijmeerspolder

3.2.3. Results - Geotechnical

Various geotechnical surveys were performed to describe the structural composition of the levee accurately. Using electromagnetic measurements, resistance tomography, radar, sampling and some lab tests, the composition of the dike was assessed.

The first and most important conclusion was that the layer subject to erosion (from ground level to a depth of 0.75 – 1.5 metres) was highly heterogeneous. The dike consisted of a sand core, covered by a relatively thin clay layer, with a strong spatial variation in thickness and sand content. Based on the radar and electric resistivity measurements, a qualitative assessment on the general profile of the dike was made. An example of three cross sectional profile of the electric resistivity measurements is given in Figure 3.15. A low electric resistivity indicates a poorly permeable layer, such as a clay, while a high electric resistivity indicates a relatively permeable layer, such as a sand.

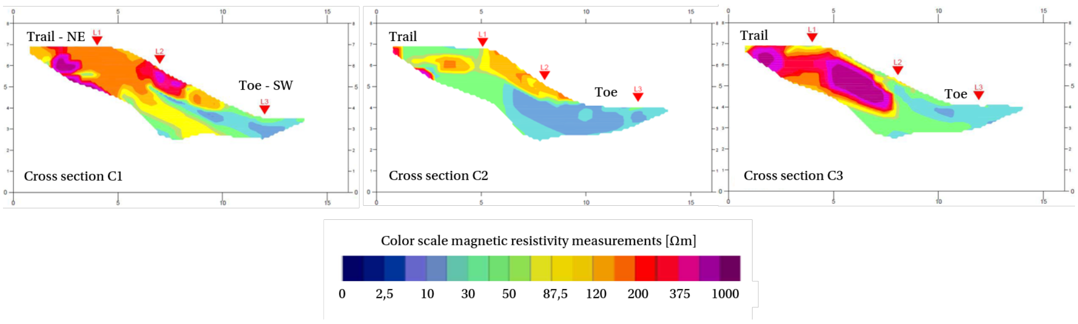

Figure 3.15: Example profiles of the elektromagnetic resistivity throughout three cross sections

Figure 3.15 clearly shows significant spatial variability in the cross sectional profile and a varying thickness of the clay cover. This variability in soil state was found during lab research as well. Table 3.5 provides an overview of the results from geotechnical lab research and in situ JETs (Jet Erosion Tests) performed on various materials.

Table 3.5: Geotechnical data Wijmeerspolder

Parameter	Unit	Top layer Site 1	Core Site 1	Top layer Site 2	Core site 2
Grain sizes					
Lutum fraction ($< 2\mu m$)	$[-]$ or $[\frac{g}{g}]$	0.27	0.04	0.10	0.09
D_{50}	$[\mu m]$	19	29	190	280
D_{10}	$[\mu m]$	1	2	5	52
$\frac{D_{60}}{D_{10}}$	$[-]$ or $[\frac{\mu m}{\mu m}]$	50	30	58	7.7
State indicators					
Plastic limit	$[-]$ or $[\frac{g_{water}}{g_{clay}}]$	[N/A]	[N/A]	0.18	0.20
Liquid limit	$[-]$ or $[\frac{g_{water}}{g_{clay}}]$	[N/A]	[N/A]	0.23	0.28
Plasticity index	[%]	[N/A]	[N/A]	5	8
JET					
Dry weight sample	$[\frac{kN}{m^3}]$	14.1	14.8	12.4	13.5
Wet (bulk) weight sample	$[\frac{kN}{m^3}]$	18.5	16.5	16.2	17.0
Volumetric water content	$[-]$ or $[\frac{cm^3}{cm^3}]$	0.31	0.108	0.311	0.254
Saturation	$[-]$ or $[\frac{cm^3}{cm^3}]$	0.95	0.35	0.74	0.72
Porosity	$[-]$ or $[\frac{cm^3}{cm^3}]$	0.47	0.46	0.53	0.49
Critical shear stress	$[Pa]$	$20.2 - 22.4$	$16.8 - 19.7$	$0 - 11$	$58 - 71.1$
Erodibility coefficient K_d	$[\frac{cm^3}{sN}]$	$27.9 - 28.5$	$2.6 - 3.4$	$0 - 0.1$	$0.6 - 0.9$

3.2.4. Conclusions

From the tests performed in the Wijmeerspolder, Belgium the following conclusions are drawn:

Grass covers significantly improve erosion resistance
The erosion resistance of the exposed turf at the Wijmeerspolder test proved to be smaller than the lean clay test section in Flood Proof Holland, as the maximum local erosion in both cases was around 30 cm, whereas the test duration in the Flood Proof Holland test was almost four times larger (2 hours and 45 minutes in Flood Proof Holland compared to 49 minutes in the Wijmeerspolder tests) during similar overflow rates. However, the tests on a grass cover showed an increased erosion resistance of the slope compared to exposed clay, allowing the overflow discharge to be increased by a factor 5 (from 35 l/m/s to a maximum of 165 l/m/s), which still did not bring the grass cover to failure. The grass cover thus increases both the maximum load and duration at which this load was sustained.

Grass cover failure leads to jetting downstream of local failure and can thus be assumed as headcut initiation criterion
When the grass cover fails (as observed due to undermining of the grass cover in the final test), the sod is typically displaced down the slope, exposing the turf and resulting in a vertical drop with a height ranging from the sward length to the depth of the turf layer, depending on the depth of the failed grass sod. Although the resulting flow seems to overshoot the exposed turf, a small, turbulent plunge pool develops on the grass sod downstream, similar to jetting observed in cohesive embankments without cover.

In case of overtopping, the location of wave impact determines headcut location, regardless of the state of the cover
Whereas the three overflow tests showed various locations for the initiation of damage, the first observations of damage in both overtopping tests were made at the location of wave impact. This is the result of high local pressures, caused by the crashing wave. The high-intensity loading of this specific location leads to a headcut much sooner than variability in cover resistance.

In case of overflow, location of grass cover failure is determined by weak spots
The location of initial cover failure varied during the tests, coinciding with preexisting damage to the grass cover, steeper parts of the slope, and (presumably) more erodible patches in the heterogeneous soil material. The location of cover failure varied between all tests, making it impossible to define a normative failure location. Therefore it is assumed that the variability of the resistance of the slope determines the initial location of cover failure, rather than the variability in the shear stresses imposed by the overflow.

In a typical storm, where a combination of overtopping and overflow is present, overtopping is the dominant failure mechanism
It was observed that even for relatively small overflow discharges, the grass bent over, partially shielding the underlying clay cover from the flow. The average overflow discharges at failure were significantly larger than the time-averaged overtopping discharges at failure. This difference is attributed to two effects: Firstly, the continuous overflow keeps the grass pushed down, covering the clay particles and increasing the protection it provides to the clay cover. Secondly, the larger flow velocities during overtopping result in flow reattachment at the landside slope, where the flow not only applies a shear stress, but also a normal stress on the slope, similar to a jetting regime. This additional stress decreases the time-to-failure of the cover.

The test discharges during the Wijmeerspolder tests were designed such that the excess shear stresses ($\tau - \tau_c$) were equal. The different flow regimes (as described above) still resulted in a shorter time-to-failure for overtopping than for overflow at equal time-averaged discharge, making it likely that in a combination of wave overtopping and overflow, overtopping initiates the erosion of the landside slope, as it occurs first (for water levels lower than the crest level) and leads to larger failure for similar time-averaged discharge.

3.3. Zwin '94 - Breach growth experiments

In the Southwest of the Netherlands, on the border with Belgium, lies nature reserve 't Zwin . This area is subject to significant sedimentation and is dredged every few years as part of the preservation of the natural habitat for local species. In 1989, a breach test was conducted here, using the sediment from regular dredging works. In October 1994, a second, more closely monitored test was performed, again using sediment from the regular dredging works to construct the test dam.

3.3.1. Test setup

By depositing approximately 6000 m^3 of dredged sand, a dam of 50 metres long was formed, with a 1 : 3 slope on both the water and landside and a crest width of 8 metres. A small trapezoidal breach was made at the crest of the dike, to facilitate initial breach flow. The resulting cross-sectional profile of the dike, overhanging measurement rig and the size and shape of the initial breach are presented in Figure 3.16.

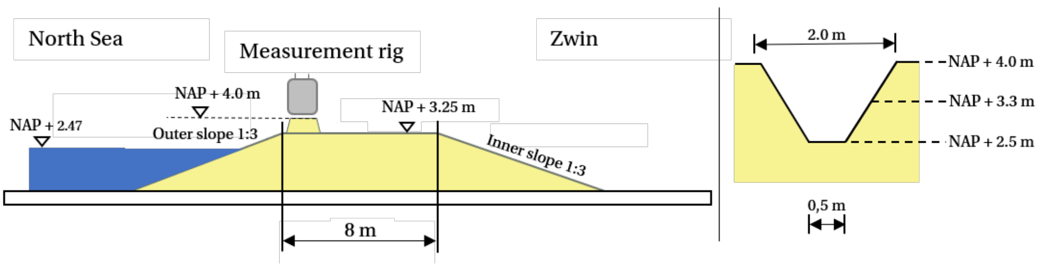

Figure 3.16: Test setup for the breaching experiment on October 6th

After the test, some repairs were made to be able to test a slightly modified profile in a second test, a day later. The measurement rig was not used for the second test, due to logistic difficulties. The adapted dike profile in this test had a steeper, 1 : 1.5 slope on the water side and is shown in Figure 3.17. This steeper profile, combined with a wider initial breach was thought to facilitate a larger final breach width, as a smaller volume of sediment would need to be removed.

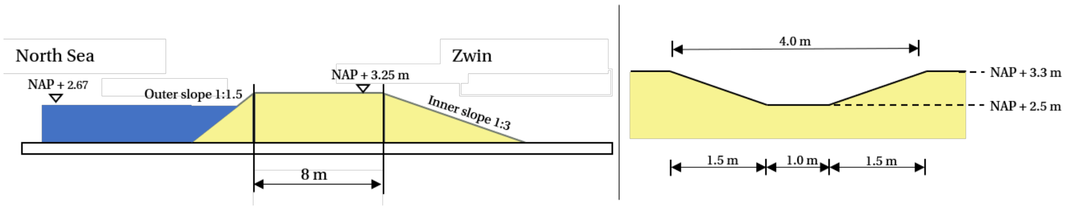

Figure 3.17: Test setup for the breaching experiment on October 7th

The test was set to start at natural high tide. The depth of the trapezoidal indentations was chosen such that the expected high tide would initiate overflow. Using sandbags, a depth of 20 centimetres over the crest was retained, after which the bags would be removed to initiate breach flow. As the high tide on the first experiment was lower than expected (NAP+2.24 m when overflow finally occurred), some additional excavation was needed to initiate breach flow, and the resulting breach flow velocities were lower than anticipated. During the second experiment, larger flow rates were achieved, due to a more accurate estimate of actual tidal level shortly before the test (NAP+2.69). The flow velocities, water depths and erosion velocities were measured using pressure gauges, velocity measurement buoys and so-called "trillos". These were installed in the dam and bed of 't Zwin (downstream) at various depths up to 3.0 metres, qualitatively indicating vibrations by sending electric signals. The reasoning behind the trillo was that it would pick up on significantly larger vibrations when it became exposed to soil, indicating when a certain erosion depth would be achieved.

3.3.2. Results - Erosion

The water depths, flow velocities and breach growth for both tests is presented in this subsection. A short factual description of each experiment is presented with the data.

October 6th

During the first experiment on October 6th, the high water level was significantly lower than expected, resulting in low breach flow velocities. The observed breach flow had a maximum flow velocity of 0.64 m/s and remained below 0.35 m/s for most of the duration of the experiment. The width of the breach at water level and at the crest of the dike was observed during the experiment. Results of these observations are plotted in Figure 3.18. No scour development downstream of the breach was measured, as the trillos were installed at a minimum depth of 0.75 metres and none of them became exposed to flow.

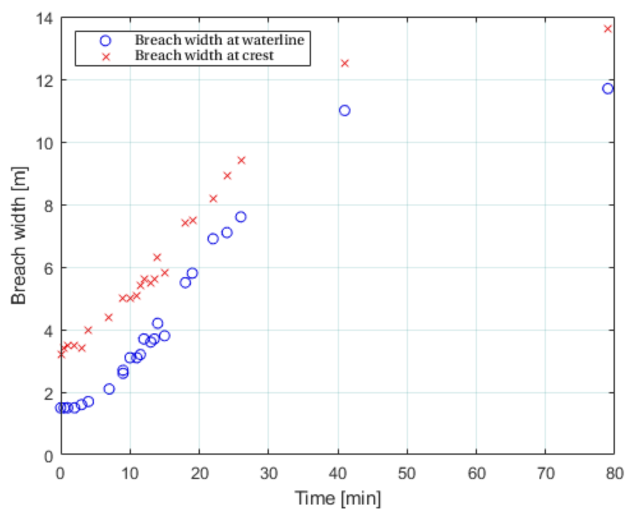

Figure 3.18: Breach width increase during the breaching test in 't Zwin, October 6th 1996

October 7th

During the second breaching experiment on October 7th, the flow velocities during the test were significantly increased. At various points in time, measurements were taken in the breach to assess the breach flow velocity. From these measurements and photo/video material of the tests, flow velocities elsewhere during the test were estimated. The measured and estimated flow velocities at the breach are plotted in Figure 3.19.

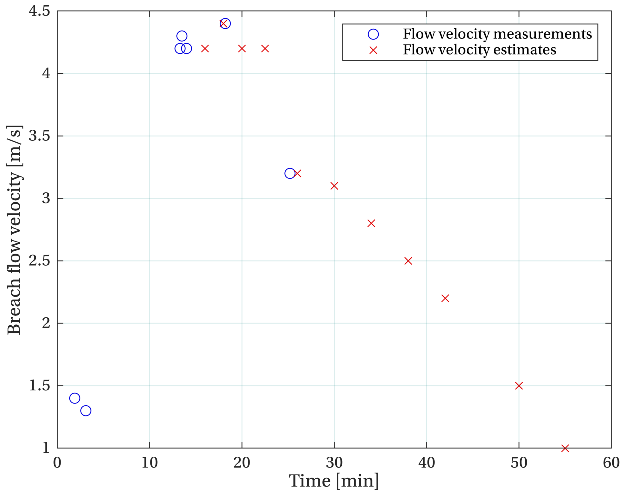

Figure 3.19: Measured and estimated breach flow velocities at 't Zwin test on October 7th 1996

As a result of the significant increase in flow velocity through the breach, the growth of the breach was much larger than during the first test. The development of the breach width has been measured in left and right direction separately, showing an asymmetric development of the breach. Figure 3.20a shows the development of the breach in both directions separately over time, while Figure 3.20b shows the overall breach width development.

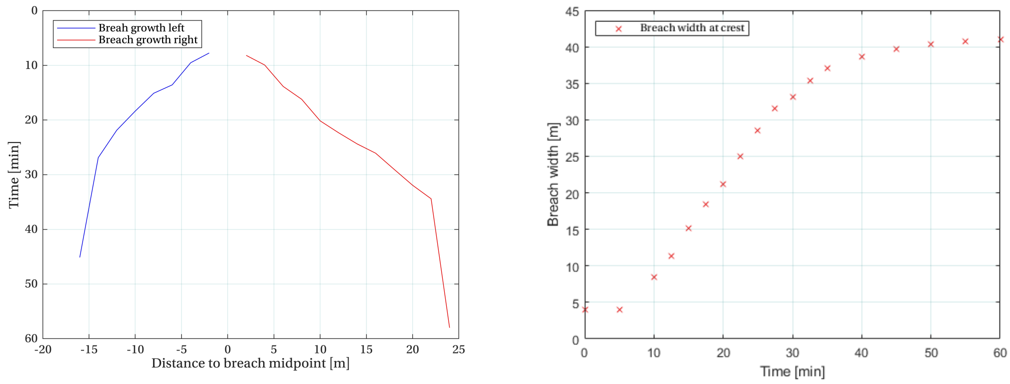

(a) Development of breach width over time (b) Total breach width as a function of time

Figure 3.20: Breach width increase during the breaching test in 't Zwin, October 7th 1996

3.3.3. Results - Geotechnical

Relatively little geotechnical data was gathered from 't Zwin experiment, as the models the test served to validate, were not based on extensive geotechnical formulations, but rather on sediment transport formulas, which only require limit data, thanks to their simplicity. The dam was constructed in the locally available sediment, which was a mixture of two sands of different origin: a fine sand with some silty deposits, natural to the area and a courser sand, containing some shell particles and sand particles which were glued together, even after oven-drying. This courser sand was used in sand nourishment on the Belgian coast, after which it washed into 't Zwin by the (net) northward directed alongshore sediment transport from the Belgian coast. Table 3.6 shows the relevant grain sizes for the two sands.

Table 3.6: Geotechnical data Wijmeerspolder

Grain size	Unit	Zwin sand	Dredged sand
D_{90}	$[\mu m]$	285	215
D_{50}	$[\mu m]$	185	315
D_{10}	$[\mu m]$	155	600

3.3.4. Conclusions

Breaching tests in large and small scale erosion show strong similarities
The model by Visser (1998) was originally developed, based on sand erosion tests on smaller embankments in flume tests. The tests in 't Zwin showed that for a homogeneous sand dike, the erosion processes and phasing of dike breaching in a homogeneous sand dike still apply. It remains interesting to see whether the applied erosion formulas are appropriate for the flow regime, or if an erosion formula suitable for larger Shields parameters is more applicable (Bisschop, 2018, van Rhee, 2010).

The course of breach widening in sand is independent of the flow velocity
Although the two tests resulted in a significantly different final breach width, the profiles in Figures 3.18 and 3.20b show strong similarities. The phases identified by Visser therefore seem to occur for both high and low flow velocities.

3.4. Zhao tests - small-scale headcut migration tests

A final set of headcut migration tests in a small-scale flume setup was chosen to validate the headcut migration process in the model and to assess the applicability of the model as a whole on a smaller scale. This validation is presented in Sections 4.5 through 4.7.

3.4.1. Test setup

The selected tests were conducted by Zhao (2013) to assess the headcut migration rate trough a homogeneous embankment constructed in three sand-clay mixtures of increasing clay content. The water level downstream of the embankment was varied, as well as the erodibility of the underlying soil layers. All embankments had an equal cross-sectional profile, with a 1 : 2 upstream slope and a vertical cliff downstream. The height of the embankment and the flume width were 0.80 metres in all cases. Figure 3.21 shows the profile under consideration, for the non-erodible tests (top) and including an erodible bed, protected by a revetment up- and downstream (bottom).

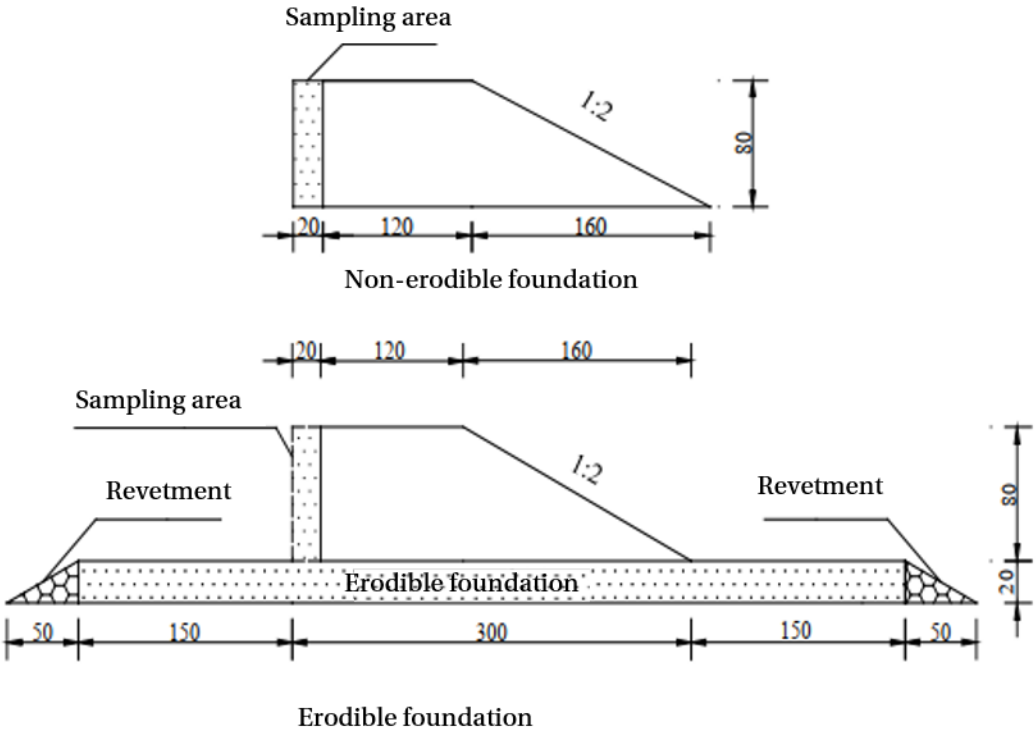

Figure 3.21: Headcut erosion test setup used by Zhao

The embankments were constructed in layers, which were densified by hand-rolling each layer until sufficiently compacted. A vertical wall in cross-stream direction was built at an appropriate height to retain a water level between 0 and 25 centimetres downstream. Water was recirculated by the pump system via the storage basin. Table 3.7 gives an overview of the tests performed by Zhao (2013).

Table 3.7: Overview of flume tests performed by Zhao (2013)

No.	Series	Soil material	Foundation	Tailwater depth (cm)
1	T_{s1}	Pure fine sand	Non-erodible	0
2	T_{s2}	Pure fine sand	Non-erodible	10
3	T_{s3}	Pure fine sand	Non-erodible	25
4	T_{s4}	Pure fine sand	Erodible	0
5	T_{s5}	Pure fine sand	Erodible	10
6	T_{s6}	Pure fine sand	Erodible	25
7	T_{l1}	Mixture fine sand and little clay	Non-erodible	0
8	T_{l2}	Mixture fine sand and little clay	Non-erodible	10
9	T_{l3}	Mixture fine sand and little clay	Non-erodible	25
10	T_{l4}	Mixture fine sand and little clay	Erodible	0
11	T_{l5}	Mixture fine sand and little clay	Erodible	10
12	T_{l6}	Mixture fine sand and little clay	Erodible	25
13	T_{m1}	Mixture fine sand with more clay	Non-erodible	0
14	T_{m2}	Mixture fine sand with more clay	Non-erodible	10
15	T_{m3}	Mixture fine sand with more clay	Non-erodible	25
16	T_{m4}	Mixture fine sand with more clay	Erodible	0
17	T_{m5}	Mixture fine sand with more clay	Erodible	10
18	T_{m6}	Mixture fine sand with more clay	Erodible	25

3.4.2. Results - Erosion

The residual profiles three of the erosion tests are given in Figure 3.22. No erosion rates have been measured, however, these can be derived from the profile changes over time.

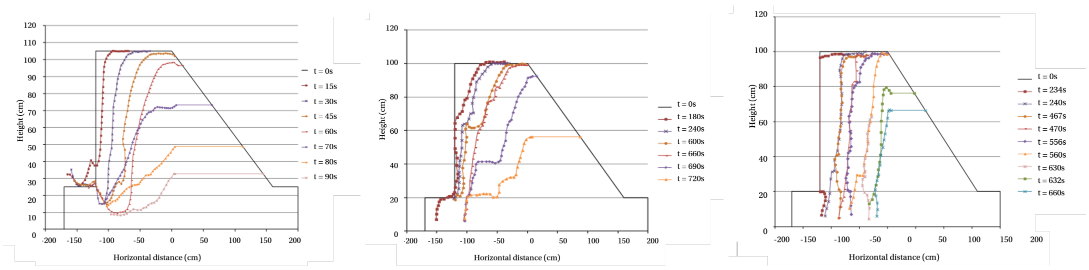

(a) Headcut migration test T_{s4} (b) Headcut migration test T_{l1} (c) Headcut migration test T_{m6}

Figure 3.22: Residual profile measurements of headcut migration tests in various materials (fltr: fine sand, fine sand with little clay, fine sand with more clay

3.4.3. Results - Geotechnical

As the soil mixtures have been mixed specifically for the erosion tests and various geotechnical experiments have been conducted, quite a reasonable dataset on the material is available. Table 3.8 list the parameters gathered on the soil mixtures. The soil mixtures used by Zhao are most comparable to the three different soils tested in Flood Proof Holland, as all mixtures have a fairly high sand content and some (varying) cohesive matter.

Table 3.8: Geotechnical data Wijmeerspolder

Parameter	Unit	Fine sand	Fine sand with some clay	Fine sand with more clay
Grain sizes				
Lutum fraction ($< 2\mu m$)	$[-]$ or $[\frac{g}{g}]$	0	0.05[1]	0.12
D_{50}	$[\mu m]$	200	410	170
D_{10}	$[\mu m]$	180	12	2
$\frac{D_{60}}{D_{10}}$	$[-]$ or $[\frac{\mu m}{\mu m}]$	1.06	39.2	150
Weights				
Dry weight	$[\frac{kN}{m^3}]$	14.1	14.8	12.4
Saturated weight	$[\frac{kN}{m^3}]$	15.7	16.8	20.3
Volumetric water content	$[-]$ or $[\frac{cm^3}{cm^3}]$	0.113	0.096	0.131
Strenght parameters				
Unsaturated direct shear cohesion (C_q)	$[kPa]$	N/A[2]	16.9	18.4
Unsaturated direct shear friction angle (ϕ_q)	[°]	N/A	26.3	24.6
Unsaturated-unconsolidated-undrained triaxial shear cohesion (C_u)	$[kPa]$	N/A	16.9	18.4
Unsaturated-unconsolidated-undrained triaxial shear friction angle (ϕ_u)	[°]	N/A	26.3	24.6
Erodibility coefficient K_d	$[\frac{cm^3}{sN}]$	N/A	2.2	0.012

3.4.4. Conclusions

Headcuts are subject to a combination of surface erosion and scour-stability failure
The erosion of the tested sand dikes was dominated by crest lowering through surface erosion. Headcut stability failure rarely occurred. In cohesive materials, stability failures were more common, but still surface erosion was observed, due to the relatively large fraction of coarse materials.

The ratio of surface erosion on the crest and scour erosion at the toe of the headcut determines whether headcut or surface erosion dominates the process
As long as the surface erosion on the crest was larger than the scour erosion at the toe of the dike, the headcut

[1] Extrapolated from grain distribution.
[2] The non-cohesive sand was assumed not to contribute to headcut stability, therefore no tests on strength parameters were performed.

height lowers, making headcut stability failure less likely, making surface erosion the dominant mechanism. When downstream scour erosion is larger than the surface erosion on the crest, the fall height of the water increases, increasing the downstream erosion, making headcut stability failure the dominant erosion mechanism.

Erodible base layers lead to increased headcut migration speed
The presence of an erodible base layer lead to a higher horizontal migration speed of the headcut, as downstream scour was able to undercut the dike material more easily. It should be noted that the material in the erodible base was in all cases more erodible than the dike material.

Increased tailwater depth leads to a reduced erosion rate for erodible dike core material
Increased tailwater depth reduces the stresses posed on the base downstream of the headcut, as the stresses dissipate once the jet hits the water surface. For erodible (poorly cohesive) materials, this directly leads to a reduced erosion rate. For more cohesive samples, this effect was not observed. This is most likely a result of the drained failure the cohesive material needs to undergo to be eroded. As the infiltration of water takes time, the permeability of the soil becomes the normative factor in the erosion rate, rather than the stresses on clay. As the stresses do not exceed the undrained shear strength of the soil, the soil still fails in a drained manner.

4
Model Verification

This Chapter presents and compares various equations for each stage of the breach formation process. The most suitable equations are selected, based on a validation against the experiments, of which the most extensive are described in Chapter 3. Section 4.1 summarises the modelled phases. Thereafter, the remaining Sections discuss the existing and adopted mathematical formulations of each phase.

4.1. Breach formation phases - An overview of modelled processes

As stated in Section 1.3, not only the applied equations, but also the modelled erosion and failure processes vary widely between breach formation and breach growth models. As this research aims to quantitatively describe contribution of different components of the dike to its time-to-failure, the phasing is based on the sequential failure of the different layers. This method allows calculation and sensitivity analysis of the failure of each layer independently.

The breaching process is modelled as four sequential phases, based on the failure of various structural elements of the dike: failure of the grass cover, erosion of the clay cover, headcut migration through the non-cohesive core and (after a breach has been formed) lateral breach growth. This phasing is based on the process description by d'Eliso (2007).

4.1.1. Grass cover failure

The first phase describes the failure of the grass cover, starting as soon as the landside slope becomes subjected to overflow. The flow is assumed to be surface-parallel during this phase, leading to shear stresses on the grass cover. The flow is assumed to shear a sod of grass, exposing the clay cover, initiating the next phase of the breach formation model. Figure 4.1 schematically shows the initial and final situation during the grass cover failure phase. Section 4.3 discusses the model used to simulate grass cover failure.

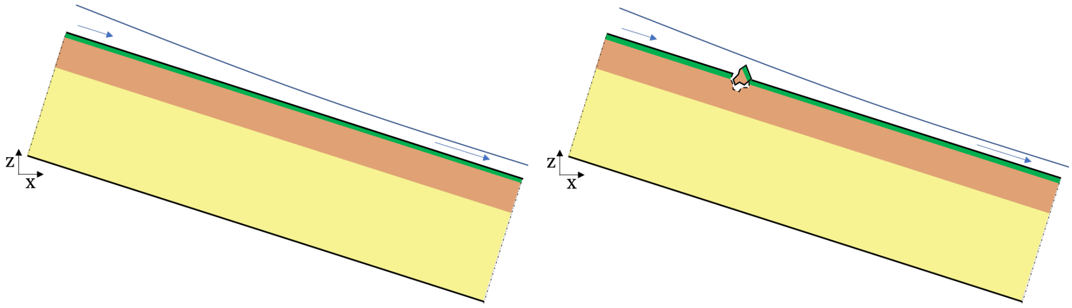

(a) Overflow along the landside dike slope (b) Grass cover failure

Figure 4.1: Visualisation of localised grass cover failure

4.1.2. Clay cover failure

As soon as the grass cover has failed, the clay cover becomes exposed to loading. The transition from grass cover failure to the loading of the clay cover is assumed to lead to a transition in flow regime from surface-parallel flow to impinging jet flow. The validity of this assumption is discussed in Subsection 4.5.2. Figure 4.2 shows the initial and final state of the landside slope for the clay cover failure process. Section 4.4 describes the mathematical model used in this phase of breach formation.

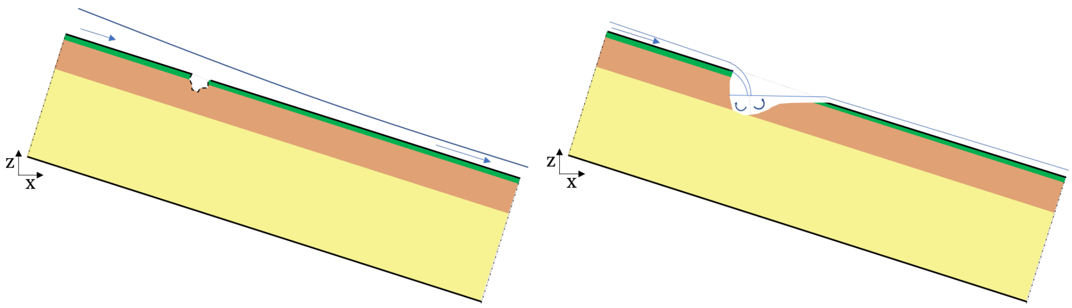

(a) Clay cover is exposed to flow (b) Clay cover is eroded, sand bed is exposed

Figure 4.2: Clay cover failure process by impinging jet flow

4.1.3. Headcut migration

Once the clay cover has been eroded completely on any location on the landside slope, the non-cohesive core material becomes exposed to the jet flow in the (now deepening) turbulent scour pit. As the non-cohesive core material is far more erodible than the cohesive cover, the scour pit deepens and widens, undercutting the clay cover. The soil section shears, moving the top of the headcut cliff horizontally. This shifts the jet impact point in the direction of the water, restarting the scouring process. Figure 4.3 shows the development of a scour hole and subsequent slip plain over which the headcut slides. The equations used to model headcut migration process are presented in Sections 4.5 through 4.7.

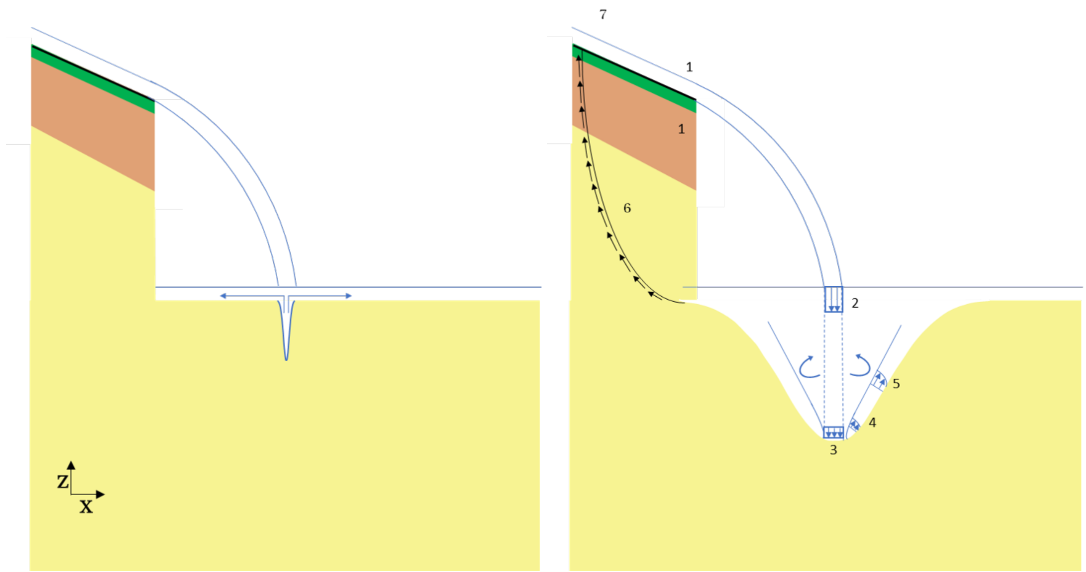

(a) Jet scour starts (b) Developed scour hole with unstable headcut

Figure 4.3: The development of a scour hole and the slip stability of a headcut

This iterative scour-stability process leads to a horizontal migration of the headcut, until it moves through the waterside slope, at which point the flow rate increases dramatically. This completes the breach formation process. The increasing flow still leads to erosion, predominantly in lateral direction. The residual material below the breach is assumed to be removed instantly due to the increased overflow rate over the headcut. Section 4.6 provides a more extensive description of this process, using the numbers indicated in Figure 4.3b.

4.1.4. Lateral breach growth

Once a breach has formed and the invert level of the dike is lowered, breach formation is considered complete. The BRAM-model runs up to this point, however, the lateral breach growth can be modelled by existing methods.

The increased discharge of the breach flow (due to the water level difference between the waterside and landside) erodes the remaining cross-section of the dike. The final part of the cross-section is not eroded, but is pushed away by the water pressure. This phase transition is assumed to be instantaneous. In reality, this will take up to several minutes (based on the model prediction of erosion rates in the order of 10^{-3} to 10^{-2} seconds) and shear resistance of the cross-section. This simplifies the model, but also yields a slight underestimation of the duration of the breach formation process.

Once the breach has formed over the complete granular core material on the lateral sides of the breach. This results in widening of the breach, or lateral breach growth, until the water level in the polder has risen, the breach flow is slowed and shear stresses are reduced. The granular core material erodes laterally (and initially vertically down to a non-erodible bottom), after which the cover material shears, similar to the headcut migration phase. Figure 4.4 shows the widening of the breach (seen from the landside, rather than in cross-sectional view, as for the previous phases). The model presented by van Damme (2019) was adopted to model lateral breach growth. This model is discussed in Section 4.6.

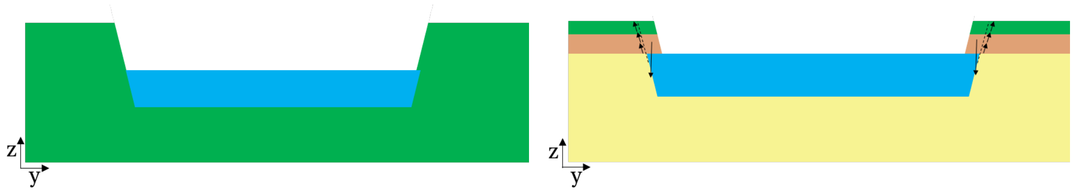

(a) A (trapezoidal) breach has formed (b) Lateral erosion and cover undercutting

Figure 4.4: Lateral breach growth as a result of undercut erosion

Table 4.1 summarises the phases, flow regime and equations applicable to each of the described breaching phases.

Table 4.1: Model structure

Model phase	**Flow regime**	**Shear stress definition**	**Erosion relation**	**Stop criterion**
1. Grass cover failure	Surface-parallel flow	Bed shear stress as in van Damme et al. (2012)	N/A	Failure grass cover and turf layer
2. Clay cover failure	Surface-parallel and jet flow	Bed shear stress as in van Damme et al. (2012) and Riteco (2017)	Winterwerp and van Kesteren (2004)	Exposure of the sand core to flow
3. Headcut erosion	Impinging jet	Equation 2.1b, C_f as fitted by Riteco (2017)	Bisschop (2018)	Invert height lowered, initiating weir flow
4. Lateral growth	Weir flow	Equation 2.1b, C_f calculated through Equation 2.4	van Damme (2019)	Breach flow velocity reduction

4.2. Flow regime overflow

Most process-based breach models apply a 2d-2d dimensional simplification of the situation. This model applies such a system as well. This means the flow is initially simulated in a plane with (x,z) Cartesian coordinate system in a cross-sectional plane through the dike. The dike serves as a weir, behind which initially, the water level lies on or below the invert level. Modelling the flow over the dike has been done through various methods, summarised in the overview of process-based models in Table 2.2. Figure 4.5a shows the situation described by the flow regime: The water initially flows over the grass cover, exposing it to shear stresses. Figure 4.5b shows the occurrence of an initial damage of the cover.

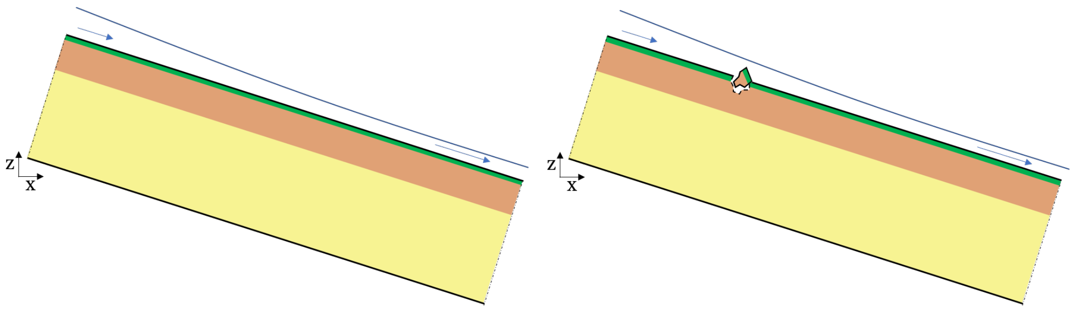

(a) Overflow along the landside dike slope (b) Initial damage to the slope

Figure 4.5: Visualisation of localised grass cover failure

In an idealised overflow situation, the water level exceeds the crest of the dike equally along the entire length of the dike for a certain duration. In reality, this is not the case. On a large scale (up to hundreds of kilometres), the flood water level (for example: the local height of a flood wave along a river) varies and on a smaller scale (metres) local variation in subsidence of the dike results in non-uniform retaining heights. For sea and lake dikes, curvature in the dike and wind setup causes a local maximum in the water level. In any case, the rising water first causes a smaller overflow rate, increasing to a peak value, after which it decreases again, resulting in slow variation of the overflow rate, which can then be modelled as quasi-steady flow. All these effects lead to a local normative section, where the overflow rate per unit width (q) is highest and a duration of overflow, based on the hydraulic conditions.

The flow over the dike (assumed constant or varying as described before) becomes turbulent along the land-side slope of the dike. Different approaches to modelling the turbulent flow include the Bélanger equation, the Bernoulli equation, expanded to various forms or weir formulas and in some recent breach models even the RANS equation. Due to the high computational effort required to apply this model, it is excluded from validation in this research. The alternatives considered are the flow modules used by Visser (1998), van Damme et al. (2012) and the preliminary model of d'Eliso (2007), originally presented for application on wave overtopping in Schuttrumpf and Oumeraci (2005). As only the AREBA-model posed by van Damme et al. (2012) presents a direct description of the bed shear stress along the landside slope as a result of the flow velocity and flow depth, this definition is applied to all of the models. The definition of water depth and flow velocities as a function of the water level is varied between the models and can be compared directly. The models are compared on the dike profile as tested in Flood Proof Holland, with one major difference: the simulated case assumes a grass cover to be present, increasing the roughness of the bed.

4.2.1. BRES-Visser method

Visser (1998) identified the flow on the landside slope of the dike to be supercritical and marked the resemblance of the overflow over the dike to the flow over a broad-crested weir. The flow through the (assumed trapezoidal) breach is described by the weir formula given in Equation 4.1. Note that this equation is equivalent to Equation 2.6, but specified for a trapezoidal breach shape.

$$Q_{br} = m\frac{2}{3}\sqrt{g}B(h_0 - Z_{br})^{3/2} \tag{4.1}$$

To define the flow depth and velocity on any point on the slope, (an adapted form of) the Bélanger equation is applied, in which an adaptation length (l_n, see Equation 4.2) is defined as the length over which the flow gradually varies from the critical flow depth to (nearly) the normal flow depth. At a distance along the slope of $2.5 \cdot \lambda_a$, the depth was experimentally found to be equal to 99.3% of the normal depth on a sand bed. For simplification, the complete normal flow depth was assumed to have been reached here, therefore a simplification error is implicitly accepted. Strictly speaking, the Bélanger equation asymptotically approaches the normal depth of flow, never reaching the exact value.

$$l_n = 2.5 \cdot \lambda_a = \frac{2.5(Fr_n^2 - 1)d_n}{\tan\beta} \tag{4.2}$$

The definition of flow depth is then reduced to a boundary value problem of the Bélanger equation, applying continuity of the flow per unit width to define the mean flow velocity on each point along the slope, as shown in Equations 4.3a and 4.3b.

$$d_i = d_n + (d_c - d_n) \cdot e^{(\frac{-5x}{l_n})} \tag{4.3a}$$

$$u_i = q/d_i \tag{4.3b}$$

4.2.2. Schüttrumpf-Oumeraci method

Based on wave overtopping tests, Schuttrumpf and Oumeraci (2005) developed an empirical description of the flow regime, which is more applicable to a time-varying discharge than the formulas by Visser (1998). Although originally calibrated for water overtopping and combined flow (a combination of wave overtopping and overflow), the formulas can be applied to overflow (as was done in the preliminary model posed by d'Eliso (2007), although little validation of the empirical factors for this case is presented in either publication).

The formulas form an implicit system, which describe the flow over the waterside dike slope, dike crest and landside dike slope in three iterative steps. The method requires an initial estimate of either the flow depth or flow velocity at the waterside to iterate to a flow depth and velocity profile along the landside slope. As this research focuses only on overflow and critical flow on the transition from dike crest to the landside slope is assumed, only the flow profile on the landside slope is needed. The system of equations used by Schuttrumpf and Oumeraci (2005) for this part of the dike is given in Equations 4.4a through 4.4e. In these equations, s is the location along the landside slope and f is a non-dimensional friction loss, which according to the calibration by Schüttrumpf is equal to 0.02.

$$s = \frac{x}{\cos(\beta)} \tag{4.4a}$$

$$d_0 = d_0 \tag{4.4b}$$

$$k_l(s) = \sqrt{\frac{2fg\sin(\beta)}{h_i(s)}} \tag{4.4c}$$

$$u_i(s) = -\frac{u_c + \frac{k_l(s)h_i(s)}{f}\tanh(\frac{k_l(s)t}{2})}{1+\frac{fu_c}{h_i(s)k_l(s)\tanh\frac{k_l(s)t}{2}}} \tag{4.4d}$$

$$t \approx -\frac{u_c}{g\sin(\beta)} + \sqrt{\frac{u_i(s)^2}{g^2\sin(\beta)^2} + \frac{2s}{g\sin(\beta)}} \tag{4.4e}$$

4.2.3. AREBA method

The AREBA breach model applies an approach that is similar to that of Visser (1998), however, it eliminates some empirical approximation of parameters and aims to describe the flow profile through a more extensive list of physically-based parameters. Again, the model makes use of an adaptation length of the flow, however, the definition of this length is different. The adaptation length used in the AREBA model is the length over which the depth along the slope has reduced by a factor $\frac{d_c - d_n}{e}$. Manning's roughness coefficient is used to represent the friction of the slope, making it applicable to a wider range of bed types than the formulation by Visser (1998), which was empirically fitted to results on sand slopes. The resulting definition of the adaptation length is presented in Equation 4.5.

$$\lambda_a = \left(\frac{1}{3i_b} - \frac{d_n^{1/3}}{3gn^2}\right)\cdot d_n \tag{4.5}$$

The change in adaptation length yields a slight change to the exponent in the Bélanger equation, as compared to the one used by Visser (1998), resulting in the expression of the depth of flow along the landside slope of the dike given in Equation 4.6. Note that the empirical factor of −5 has been removed from the exponent.

$$d_i = d_n + (d_c - d_n)\cdot e^{\frac{x}{\lambda_a}} \tag{4.6}$$

AREBA also includes a direct definition of the bed shear stresses as a function of the flow velocity, location, bed roughness and normal depth of flow. The imposed bed shear stress due to parallel flow (applied in the surface erosion module) is presented in Equation 4.7. By filling in the flow velocities for each of not only this model, but also the BRES-model and empirical method by Schüttrumpf and Oumeraci, the methods can be compared. Equation 4.7 is based on the assumption of steady flow (see Section 2.1). The principle of continuity is still applied to define the flow velocity (u_i is therefore still defined as in Equation 4.3b.)

$$\tau_b = \rho_w u_i^2 \frac{n^2 g}{d_n^{1/3}} \tag{4.7}$$

4.2.4. Adopted flow regime description

A comparison of these three methods, describing the imposed bed shear stress during overflow (surface-parallel flow) over the landside slope of a dike, yields the results presented in Figures 4.6a through 4.6c.

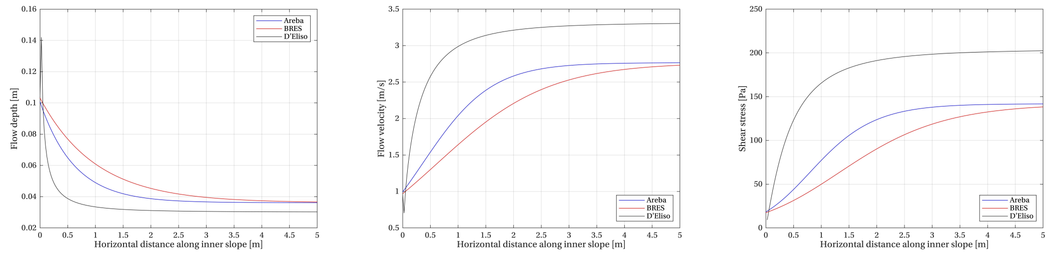

(a) Flow depth (b) Flow velocity (c) Overflow shear stresses

Figure 4.6: Comparison of the BRES, AREBA and Schüttrumpf-Oumeraci methods describing the flow regime along the landside dike slope during overflow

The comparison between the methods indicates that the empirical method by Schüttrumpf and Oumeraci estimates far smaller flow depths and (as continuity applies) a flow speed which is up to 80% higher than the other two methods. This is to be expected, as this method was originally developed for the non-stationary flow found during wave overtopping, rather than continuous overflow. Typically, wave overtopping leads to a shorter time-to-failure and can thus be expected to be modelled by higher representative flow velocities (and thus a higher shear stress and shorter time-to-failure). As the ratio of the shear stress and the flow velocity is determined by the friction factor, a re-calibration of the Schüttrumpf and Oumeraci method, applying a corrected friction factor f (using 0.035 instead of the originally advised value of 0.02) was made.

The friction factor was deemed the most promising parameter for calibration based on differences in response of grass between overflow and overtopping (see Subsection 4.3.1), but the method by Schüttrumpf and Oumeraci still yielded unsatisfactory results, as the flow adaptation length remained extremely low compared to other methods and visual observations from experiments. Figures 4.7a and 4.7b show the flow depth and shear stress functions again, compared against the calibrated Schüttrumpf-Oumeraci method, where the friction factor was increased to 0.035.

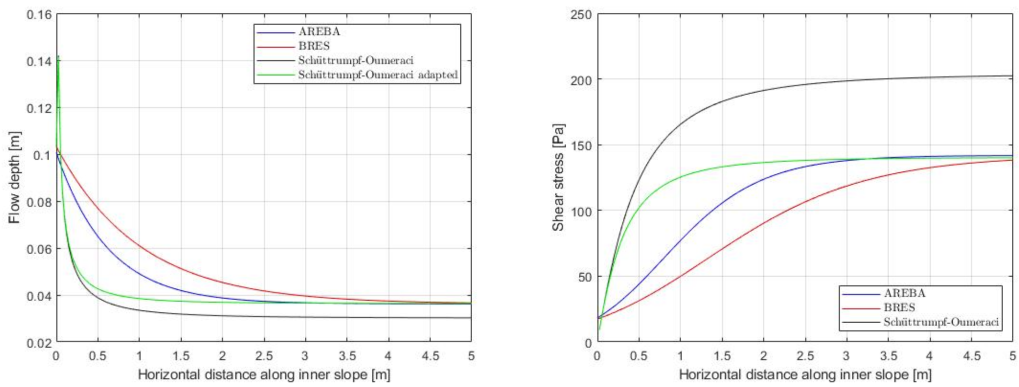

(a) Flow depth along the landside dike slope (b) Resulting overflow shear stress

Figure 4.7: Comparison of overflow methods including the Schüttrumpf-Oumeraci calibrated for overflow

The the BRES and AREBA models yield similar results, although the definition of the flow depth differs (Visser (1998) defining the adaptation length as the length where the water depth is 99.7% of the normal flow depth, whereas van Damme et al. (2012) defines the adaptation length as the location where the flow is the critical depth divided by *e*).

The advantage of the AREBA flow module over the BRES formulas lies in the included parameters: the inclusion of Manning's roughness coefficient in AREBA makes it possible to include the effect of bed roughness, which given the test case (a grass cover, providing a relatively high bed roughness) should have a significant influence on the flow, whereas the (empirical) coefficients of the BRES model only apply to a sand slope. Therefore, the AREBA flow module is applied in the proposed model in this research.

4.3. Grass cover failure

Initially, the turbulent flow over the landside slope of the dike results in stresses on the grass cover, which fails on the location where the largest shear stresses are predicted (the dike toe) or at a local weak spot (as observed in most experiments, see Figure 4.5a). In this Section, three pre-existing equations to determine the time-to-failure of the grass cover are compared and one method is selected for application in the model. The compared methods are the empirical relationship posed by Whitehead et al. (1976), based on a range of overflow experiments; the process-oriented equation posed by Temple et al. (1987) and the reformulation of this method as a shear-stress based method by d'Eliso (2007).

4.3.1. Whitehead method

The empirical relations posed by Whitehead, and presented in Equations 2.12a through 2.12c and plotted in Figure 4.8 are based on British overflow experiments in which common grass species on mostly small slopes (1:33.3 to 1:16.6) and a few on steeper slopes (up to 1:4.16). The length of grass in the CIRIA tests varied between 0.05 and 0.9 metres and showed a variance of Manning's roughness coefficient n for varying water depth: values as high as 0.2 to 0.3 until the water depth approached grass height, and as low as 0.03 to 0.05 on fully submerged grass on steeper slopes, where the grass leaves lay over and provide an almost smooth surface to the flow. The resulting time from these formulas is the time at which a dangerous erosion has occurred, at which the stability of the slope is at risk.

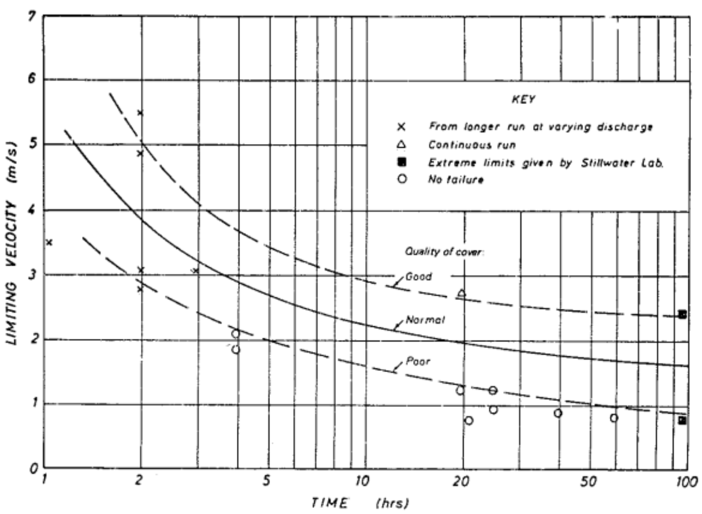

Figure 4.8: Graphs estimating the time-to-failure of grass covers as posed by Whitehead et al. (1976)

Due to the significant differences in conditions between overflow over a dike and the tested slopes by Whitehead (which had a significantly smaller slope and lower ratio of water level to grass height), these equations are not considered suitable to be applied in this breach formation model. The applied criterion in Whitehead et al. (1976) of time-to-failure also makes it hard to define the damage at this point in time, as no further description is given for when the stability of the slope is considered to be at risk. Whitehead et al. (1976) recommended further research into the aforementioned effects, as well as the size of damaged patches in the grass cover compared to the sward height, which was considered to influence the protective capabilities of the grass.

4.3.2. Temple and Hanson method

A process-oriented method relating the time-to-failure of a grass cover to various resistance parameters of the soil through a shear stress balance was posed by Temple and Hanson (1994). Through two key assumptions: the assumption of a normal depth and the assumption that the imposed flow shear stress exceeds the critical shear stress of the bed material, Equation 4.8a is derived, which under the assumption of quasi-steady flow regime reduces to Equation 4.8b.

$$\int_0^{t_{gf}} \rho_w d_n i_b (1 - C_f) \left(\frac{n_c}{n_{tot}} \right)^2 dt = 0.2 I_p + 1 \tag{4.8a}$$

$$t_{gf} = \frac{(0.2 I_p + 1)}{(\rho_w d_n i_b (1 - C_f) (\frac{n_c}{n_{tot}})^2} \tag{4.8b}$$

In which:

- t_{gf} denotes the time to failure of the grass $[h]$;
- C_f is a nondimensional grass cover factor, representing the quality of the grass cover;
- i_b denotes the nondimensional bed slope;
- n_c represents Manning's roughness coefficient of only the bed material $[s/m^{\frac{1}{3}}]$;
- n_{tot} represents Manning's roughness coefficient of the grass cover as a whole $[s/m^{\frac{1}{3}}]$.

The assumption of exceeding a critical shear stress implies the assumption of grain-by-grain pickup, which is not a dominant erosion mechanism for clay. However, the inclusion of the plasticity index I_p in this formula does include the water sensitivity of clay, commonly related to the saturation and swelling, which clay undergoes before eroding (in drained loading regime). Combined with the assumption of a normal flow depth, this method gives a crude representation of the relevant (hydraulic) load and (soil) resistance at play during erosion of the grass cover, as it has been shown in Section 4.2 that the flow depth varies and is only equal to the normal depth of flow at the toe of the dike. In Temple and Hanson (1994), no direct calculation of the erosion depth after grass cover failure is presented. Instead, an assumed erosion depth of half a foot (≈ 0.1524 m) is assumed. The resulting time indicates when the clay layer is no longer fully protected by the grass cover.

4.3.3. D'Eliso method

In d'Eliso (2007) an adapted version of the model posed by Temple and Hanson (1994) is presented. The assumption of normal depth of flow is no longer applied, as D'Eliso uses a separate module to define flow depth, leaving the assumption of the imposed shear stress exceeding the critical shear stress as the only assumption on which the method is based. The adaptations by D'Eliso aim to determine the time-to-failure of the grass cover in a shear stress-based manner, rather than in an assumed normal flow. This makes the method more suitable for application along steep dike slopes, as normal flow is only approached at the toe of the dike, but is never reached (see Section 4.2. The set of equations used by D'Eliso is presented in Equations 4.9a through

4.9d. The resulting time indicates when the clay layer is no longer fully protected by the grass cover.

$$\tau_0 = \rho_w g d J \tag{4.9a}$$

$$\tau_{0,e} = \tau_0 (1 - C_f) \left(\frac{n_c}{n_{tot}} \right)^2 \tag{4.9b}$$

$$\int_0^{t_{gf}} \tau_{0,e} dt = 9I_p + 50 \tag{4.9c}$$

$$t_{gf} = \frac{9I_p + 50}{\tau_{0,e}} \tag{4.9d}$$

In which:

- J denotes the nondimensional energy slope, expressed as energy head loss over horizontal distance;
- τ_0 is the bottom shear stress $[N/m^2]$;
- $\tau_{0,e}$ is the effective bottom shear stress $[N/m^2]$.

As opposed to the method posed by Temple and Hanson (1994) (which guesstimates Manning's coefficients directly), d'Eliso (2007) uses empirical expressions to estimate Manning's coefficients. The equation posed by Lane (1955) is used to express the roughness of clay and Diáz's formulae are used to express the total roughness of the cover, as posed by Díaz (2005). The corresponding formulas are posed in Equation 4.10a and Equations 4.10b and 4.10c, respectively. (Due to the slope criterion, Equation 4.10b applies to most dike slopes in the Netherlands.) It should be noted that although using these relations eliminate the estimation of the roughness directly, the empirical nature of these formulas does not necessarily improve accuracy compared to a direct estimate, especially for Diaz's formulas, which were derived in subcritical flow regime only, strictly making it a poor fit for the supercritical flow on the landside slope of a breach. D'Eliso argues that the trend of roughness approaching zero for larger Froude numbers provided by Diaz's equations is correct, due to the grass laying over, smoothening the bed.

$$n_c = \frac{D_{75,c}^{1/6}}{14.23} \tag{4.10a}$$

$$n_{tot} = 0.00682 Fr^{-0.9579} \quad \text{for} \quad \beta \leq 20° \tag{4.10b}$$

$$n_{tot} = 0.00994 Fr^{-1.0085} \quad \text{for} \quad \beta \geq 20° \tag{4.10c}$$

D'Eliso poses two methods to find the initial erosion depth after grass cover failure. First, the depth of failure is defined as a function of the rooting depth (estimated to be 90% of the stem length of the grass as presented in Equation 4.11a). No data is provided or referenced to support this relation, however, experiments found the influence of the grass cover to be present until the complete rooting depth, as the roots stabilise the soil, even when the foliage had been damaged. This is likely to be caused by stabilisation of the relatively open top layer of soil by the roots, which penetrate down to the denser part of the cover (see Figure 4.9). The second method used to estimate the grass cover failure depth, is by assuming it to be equal to the normal depth of flow (Equation 4.11b.)

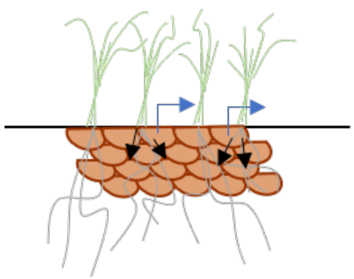

Figure 4.9: The stabilising effect of grass roots on the cover material

$$\Delta z_g = 0.9 L_s \tag{4.11a}$$

$$\Delta z_g = d_n = \frac{q^2 n^2}{i_b}^{0}.3 \tag{4.11b}$$

4.3.4. Sensitivity analysis

To determine which of the methods is most suitable, the methods are compared based on the input/output parameters; quality of description of the physical processes and the sensitivity of output values to input parameters.

Table 4.2 shows for three models what the relative change of the time-to-failure of a grass cover is, given a certain increase or decrease in all input parameters. The change of parameter is an increase or decrease of five or ten percent, with respect to the mean input values indicated at the top of the middle column. These means are based on parameters gathered at the full-scale tests, as discussed in Chapter 3. All changes in time-to-failure are calculated relative to the time-to-failure indicated in the second column from the right, through equation 4.12. Finally, the criteria for the depth of the damage at grass cover failure are presented in the rightmost column of the table. As all three models define rather than calculate this depth, the sensitivities do not apply to the depth of failure.

$$\Delta_X = \frac{X_{new} - X_{mean}}{X_{mean}} \tag{4.12}$$

Table 4.2: Sensitivity analyis of grass cover failure time to various parameters

Method	Parameter input	Mean input values for various parameters								Mean output values	
		$\rho_w[\frac{kg}{m^3}]$	$g[\frac{m}{s^2}]$	$q[\frac{m^2}{s}]$	$I_p[\%]$	$C_f[-]$	i_b or $J[-]$	$n_c[\frac{s}{m^{\frac{1}{3}}}]$	$n[\frac{s}{m^{\frac{1}{3}}}]$	t_{gf}	Δz_g [m]
		1000	9.81	0.1	9	0.6	0.33	0.02	0.025		
Temple et al. (1987)	Effect −10%	+11%	−3.5%	+7.3%	−7.8%	−9.1%	+4.1%	+23%	−19%	5044s	0.15 (fixed)
	Effect −5%	+5.3%	−1.7%	+3.5%	−3.9%	−4.8%	+2.0%	+11%	−9.8%		
	Mean										
	Effect +5%	−4.8%	+1.6%	−3.2%	+3.9%	+5.3%	−1.8%	−9.3%	+10%		
	Effect +10%	−9.1%	+3.2%	−6.2%	+7.8%	+11%	−3.5%	−17%	+21%		
d'Eliso (2007)	Effect −10%	+11%	+7.3%	+7.3%	−7.8%	−9.1%	+4.1%	+23%	−19%	4850s	$0.9L_s$ (fixed)
	Effect −5%	+5.3%	+3.5%	+3.5%	−3.9%	−4.8%	+2.0%	+11%	−9.8%		
	Mean										
	Effect +5%	−4.8%	−3.2%	−3.2%	+3.9%	+5.3%	−1.8%	−9.3%	+10%		
	Effect +10%	−9.1%	−6.2%	−6.2%	+7.8%	+11%	−3.5%	−17%	+21%		
Whitehead et al. (1976) u_{g3}	Effect −10%		+17%	+17%						60h	Not defined
	Effect −5%		+8.3%	+8.3%							
	Mean										
	Effect +5%		−8.3%	−8.3%							
	Effect +10%		−17%	−17%							

Table 4.2 shows that the Whitehead equations estimate a far larger time-to-failure (strictly even assuming a weaker grass cover than the other two methods in this test case, as u_{g3} in Equation 2.12c represents a poor grass cover, whereas $C_f = 0.6$ represents a moderately good grass cover in Equation 4.9b. This illustrates the differences between the experiments on which the method was calibrated and the flow regime on a dike slope: the larger steepness of the slope of a dike results in a more turbulent flow and variability in materials used in the dike cover, such as the water-sensitivity of the clay is not accounted for. This makes the Whitehead equations a inflexible estimation tool for grass cover failure during overflow of a dike.

The relations of Temple et al. (1987) and d'Eliso (2007) are extremely similar, thus resulting in similar results. Both models are quite sensitive to Manning's roughness (n and n_c), of which ratio basically determines how much of the flow shear load is transferred to the grass foliage and clay in the cover. The methods are also sensitive to changes in the grass cover factor C_f and water density ρ_w, as a more exposed clay layer and larger flow density logically leads to more erosion. In practice, this means the clay erodes faster when dike material has already been brought into the flow further upstream. This effect is not included in the current study or the model posed in this research.

Further testing revealed that the sensitivity to grass cover factor increases when this factor is higher. In practice this means that the difference between a good and moderate quality of a grass cover has a larger influence on the time-to-failure than the difference between a moderate and a poor grass cover. Due to natural variability, it is nearly impossible to maintain a good cover quality over the entire dike, therefore one must estimate the cover factor C_f conservatively.

The D'Eliso and Temple model differ in their sensitivities to gravitational acceleration g, where Temple states that the time-to-failure increases for higher gravitational acceleration, whereas D'Eliso predicts a decrease in time-to-failure for larger gravitational accelerations. This is a result of the adaptations D'Eliso made by adding a shear-stress based stability criterion. Temple only includes gravity in the normal depth of flow (and thus in the hydraulic load), whereas D'Eliso also includes it as a stabilising force on the bed particles.

4.3.5. Validation against data

The models were also compared against measurements on grass cover erosion (Bakker and Mom, 2015b, Cantre et al., 2017, Jong, 1970), see also Section 3.2. These tests were performed at representative overflow rates. The lab tests presented in Jong (1970) however are different from the situation of interest, as the test section was subjected to horizontal flow, rather than (more turbulent) flow along a dike slope. No large damage was observed during the tests discussed in these publications, but erosion measurements were made and (qualitatively) described. The erosion rates vary between 0.7cm/h (at flow velocity 3.0m/s) to 5 – 10cm/h for high mean flow velocity ($\overline{v}$ = 4.1m/s) and locally concentrated flow (Jong, 1970). Table 4.3 shows the parameters (and estimated parameters, based on qualitative description, indicated by (*)), based on which the strength of the grass has been calculated.

Table 4.3: Input parameters grass cover tests

Test	**Plasticity index I_p**	**Overflow rate q**	**Depth of flow d**	**Bed slope (i_b**	**Manning's roughness soil n_c**	**Mannings' roughness cover n**	**Normative diameter of soil $D_{75,c}$**
Jong (1970)	18*	0.16*	0.10	1/100	0.0130*	0.0235	$56 \cdot 10^{-6}$
Bakker and Mom (2015b)	18	0.16	0.15	1/1.7	0.0137	0.0235	$1 \cdot 10^{-3}$

Using Equation 4.9d and 4.11a, the time-to-failure of the grass cover can be assessed from both the measurements and the model. Results are presented in Table 4.4.

Table 4.4: Verification of accuracy of grass cover failure methods (Indicated time-to-failure ranges as a result of varying input parameters)

Test case	Description	C_f	d_{turf}	Reported $\overline{u}$ [m/s] or $q[m^2/s]$	Reported v_e	Resulting T_{gf}	Temple Hanson T_{gf}	D'Eliso T_{gf}[1]
Jong (1970) Test 1 sample 1	Flat surface, small irregularities, small bare patches	0.6	0.045 – 0.135	$\overline{u} = 3.0 - 4.1$	1.25 cm/h	3.6 – 10.8 h	3.0 – 6.0 h	3.0 – 15 h
Jong (1970) Test 3 sample 3	Flat surface, scattered bare patches, irregular grass sods	0.25	0.045 – 0.135	$\overline{u} = 3.0 - 4.1$	0.7 cm/h	6.4 – 19.3 h	1.6 – 3.0 h	1.6 – 8.0 h
Jong (1970) Test 4 sample 3	Flat surface, small irregularities, pipe placed in slope	0.6	0.045 – 0.135	$\overline{u} = 2.0 - 5.0$	1.5 cm/h	3.0 – 10.0 h	2.0 – 14.0 h	1.8 – 125h
Jong (1970) Test 5 sample 3	Removed top 6 cm, exposed sandy, gravely clay with roots	0.0	0.045 – 0.135	$\overline{u} = 2.0 - 4.1$	1.5 cm/h	3.0 – 9.0 h	1.2 – 5.6 h	1.2 – 50.1h
Cantre et al. (2017) Test 2 sample 2	Berm material, some grass has died, length 5 – 15cm	0.6	0.045 – 0.135	$\overline{u} = 3.0$	20 cm/h	15 – 40 min	6.0 h	15.0 h
Bakker and Mom (2015b) Overflow test 1	Overflow over 1:1.9 dike slope, long grass with debris	0.6	0.045 – 0.135	$q = 0.025 - 0.160$	N/A	7h[2]	0.5 – 1.8 h	2.6 – 8.8 h
Bakker and Mom (2015b) Overflow test 2	Overflow over 1:1.8 dike slope, long grass with debris	0.6	0.045 – 0.135	$q = 0.160$	N/A	2.1 h	0.5 h	2.6 h
Bakker and Mom (2015b) Overflow test 3	Overflow over 1:1.8 dike slope, exposed clay with roots	0.0	0.045 – 0.135	$q = 0.040$	N/A	49 min	28 min	21 min

[1] All time-to-failure ranges indicated represent the minimum to maximum time-to-failure for all possible combinations of input values for which a range of values is given

[2] The flow load was incrementally increased, of the total time-to-failure, the maximum overflow rate of 160 l/m/s was only present for 1h

4.3.6. Adopted grass failure method

Table 4.4 shows that for the lab tests, the method proposed by Temple and Hanson works best, whereas for the large-scale tests, the method by D'Eliso is more accurate. This is no result of scale effects, but is caused by the fact that the method by Temple and Hanson was developed for spillways, which behave similar to the small slopes tested on the small scale ($i_b \leq 0.01$), whereas D'Eliso assesses steeper slopes, such as tested in tests described in Bakker and Mom (2015b).

Therefore, the grass failure model posed by D'Eliso is adopted as the most suitable method to determine the time-to-failure of the grass cover. Although more suitable than the other options, some remarks must be made with regard to the grass models in general. First, the determination of parameters through empirical relations (for example, the expression presented in Equation 4.10b) on experiments in subcritical flow only, makes extrapolation to a supercritical, highly turbulent flow regime inaccurate. Second, the assumption that the depth is equal to the normal depth (only applicable to Temple et al. (1987) holds poorly, looking at the description of the flow regime in Section 4.2. Third, the assumption that the protection of grass cover C_f can be assessed from visual observations seems to hold rather poorly, as in the experiments described in Jong (1970), Test 3 showed the most visual irregularity and damage to the cover, but eroded rather slowly, as the root system of the grass sods was found to be very dense, stabilising the soil.

4.4. Clay cover erosion

Once the grass cover is damaged, the underlying clay cover becomes exposed to the flow. Generally, a differentiation is made between two types of erosion in cohesive materials: drained and undrained erosion. At low shear stresses, the infiltration of water (a drainage process) is needed for the erosion of the clay. If the undrained shear strength of the soil (typically 5 – 20 kPa for a soft soil with little to no confining pressure) is exceeded, the clay erodes in undrained manner, where the infiltration of water is no longer necessary for the erosion of clay particles, but the clay is rather sheared from the soil in strips. Figure 4.10 shows the erosion process described in this Section.

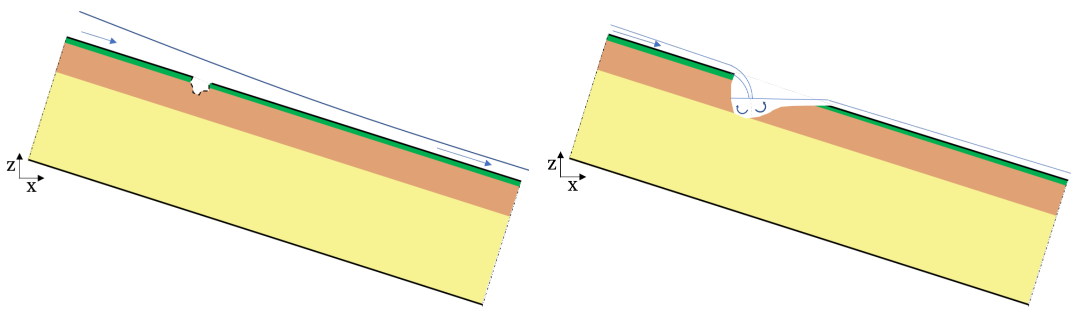

(a) Clay cover is exposed to flow

(b) Clay cover is eroded until sand bed is exposed

Figure 4.10: Development of damage in the clay cover, initiation of headcut

Nobel (2013) identified various regimes of clay erosion as a result of jetting at high pressures observed in dredging processes. During breach formation in dikes, the clay is either subjected to parallel flow with shear stresses smaller than 1 kPa (flow velocities smaller than 5 m/s) or to jet flows from small headcut heights (up to a maximum height equal to the clay cover thickness, which normally are around 0.5 metres). In both these cases the undrained shear strength of the soil is not exceeded by the imposed shear load. Therefore, the erosion of the clay is considered a drained process throughout this model.

During headcut jetting, it is worth considering what headcut height gives sufficient shear stress to result in undrained failure, to validate the assumption of drained erosion. For a minimum value approach, it is assumed that no flow energy is lost in the transition from impinging jet to bed-parallel flow. This makes it possible to use the flow velocity of the impinging jet to determine the shear stress on the bed. The following balance between the dynamic pressure of the flow and the undrained strength (expressed as a function of the undrained cohesion of the soil) is used. Assuming a low-end value of the undrained cohesion of $1kPa$ to find a normative value for the required flow velocity, the following derivation of the required flow velocity to lead to undrained erosion is found (Vardanega and Haigh, 2014).

$$q_u > S_u \tag{4.13a}$$
$$0.5\rho_w u^2 > 9C_u \tag{4.13b}$$
$$u > \sqrt{\frac{18C_u}{\rho_w}} \tag{4.13c}$$
$$u > 4.2m/s \tag{4.13d}$$

A flow velocity of $1m/s$ is assumed at the top of the headcut (corresponding to an outside water level approximately $0.10m$ above the crest of the dike and an overflow rate of $100l/m/s$). Conservation of kinetic and potential energy then yields the required headcut height to cause undrained erosion of clay. Subscript 1 here indicates the situation of the flow at the top of the headcut, whereas subscript 2 indicates the situation at the bottom of the headcut.

$$E_{k,1} + E_{p,1} = E_{k,2} + E_{p,2} \tag{4.14a}$$
$$0.5mu_1^2 + mgh_1 = 0.5mu_2^2 + h_2 \tag{4.14b}$$
$$u_2 = \sqrt{u_1^2 + g(\Delta h)} \tag{4.14c}$$
$$u_2 > 4.2m/s \tag{4.14d}$$
$$\Delta h > 1.7m \tag{4.14e}$$

The headcut height required to lead to undrained erosion of the clay layer in this case thus is 1.7 metres, which is larger than conventional clay cover thickness, neglecting the effects of any energy loss in the jet, which most notably occur in as turbulent losses in the plunge pool and have been estimated to be near 40% for vertical jet (Nobel, 2013). The inclusion of losses would lead to an even higher required headcut height to lead to undrained failure. As no accurate description of the turbulence losses in a plunge pool is available, these losses have been neglected. This results in an overestimation of the erosion rate and a conservative estimate of the time-to-failure during headcut migration.

The required headcut height for undrained erosion can thus only be achieved in high dikes with either an extremely thick cover, or a landside slope constructed completely in clay. This makes the assumption of drained erosion valid for the dike profiles considered in this research. Note that for homogeneous clay dikes, in which no sand core is present, the headcut height grows large enough to cause undrained erosion and soil wasting, making this model overestimate the time-to-failure of such a dike.

4.4.1. Winterwerp and Van Kesteren

Winterwerp and van Kesteren (2004) posed a method presented in Equation 4.15a, which relates the erosion velocity of cohesive material to the swell coefficient due to water infiltration. The influence of drainage on the erosion velocity is captured in the vertical consolidation coefficient for swell ($c_{v,sw}$). The clay layer is assumed to swell due to water infiltration, after which the increase in volume is counteracted by a pick-up flux (eroding the clay layer down to its original height, although now some of the space is taken by pore water instead of clay particles). Figure 4.11 schematises the erosion process described.

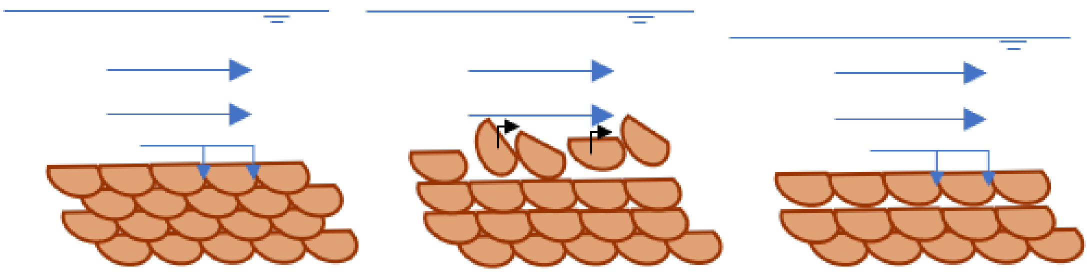

(a) Flow over a clay bed, infiltration (b) Erosion of swollen clay layer (c) Eroded bottom, process restarts

Figure 4.11: Schematic representation of drained erosion of clay

$$E = M_e \cdot (\tau_b - \tau_c) \tag{4.15a}$$

$$M_e = \frac{c_{v,sw}\phi\rho_{dry}}{10 D_{50} S_u} \tag{4.15b}$$

$$v_e = E/\rho_{dry} \tag{4.15c}$$

In which:

- $c_{v,sw}$ is the vertical consolidation coefficient for swell $[m^2/s]$;
- ρ_{dry} is the dry density of the soil $[kg/m^3]$;
- S_u is the undrained shear strength of the soil $[N/m^2]$.

Equation 4.15a assumes the erosion to be linearly dependant on the excess shear stress and the soil erodibility, which is one of two common assumptions for the erosion of cohesive material (Nobel, 2013), the alternative being a square root dependency of the erosion rate on the excess shear stress. The value of M_e is defined by the assumption that the drained erosion of the clay is limited by the infiltration of the water needed for drained erosion behaviour.

4.4.2. Van Prooijen and Winterwerp

Van Prooijen and Winterwerp (2010) elaborated on the drained erosion of clay, identifying three different stages of drained erosion of cohesive soil, still based on the excess shear stress on the soil. The stages are presented through Equation 4.16. When the mean bed shear stress lower than the critical value ($\tau_b < 0.52\tau_c$), no erosion occurs. However, instead of assuming erosion to occur when the bed shear stress exceeds critical shear stress, a floc erosion regime is defined for relatively low bed shear stresses ($0.52\tau_c < \tau_b < 1.7\tau_c$). In this erosion regime, flocs of clay particles are eroded from bottom, most notably from irregular sections, where the local shear stress deviates from the calculated mean shear stress, while the surface erosion process has not started yet. The resulting implicit relation has been simplified to a parametric form, fitting the data of floc erosion tests and smoothly coinciding with the equation by Winterwerp and van Kesteren (2004) for larger shear stresses. The resulting formula is presented in Equation 4.16 and uses the following empirical parameters: $\omega_1 = -0.144, \omega_2 = 0.904, \omega_3 = -0.823, \omega_4 = 0.204$.

$$\frac{E}{M_E \tau_c} = \left\{ \begin{array}{ll} 0, & \text{for } \frac{\overline{\tau_b}}{\tau_c} < 0.52 \\ \omega_1 \cdot \left(\frac{\overline{\tau_b}}{\tau_c}\right)^3 + \omega_2 \cdot \left(\frac{\overline{\tau_b}}{\tau_c}\right)^2 + \omega_3 \cdot \frac{\overline{\tau_b}}{\tau_c} + \omega_4, & \text{for } 0.52 < \frac{\overline{\tau_b}}{\tau_c} < 1.7 \\ \frac{\overline{\tau_b}}{\tau_c} - 1, & \text{for } \frac{\overline{\tau_b}}{\tau_c} > 1.7 \end{array} \right\} \tag{4.16}$$

4.4.3. Important input parameters

The difficulty in many erosion formulas is twofold: First, as stated in Subsection 4.4.1 the exact form of the relation between the erosion rate and the excess shear stress is subject to significant discussion. Furthermore, the input parameters of this equation, such as the erodibility coefficient (M_e, see Equation 4.15a) and the critical shear stress τ_c are difficult to determine, as they depend on many geotechnical parameters, such as the water content, drainage of the soil, particle density and type and quantity of clay minerals(Nobel, 2013).

The critical shear stress is an important parameter in defining the erosion of soils. Equations 4.17a and 4.17b pose two empirical methods to determine the critical shear stress of soils, based on other soil parameters. Equation 4.17a was posed by Smerdon and Beasley (1959) and is applicable to soft clays with a relatively low undrained shear strength ($S_u < 10$ kPa). Equation 4.17b was developed by Whitehouse et al. (2000) for erosion of steep clay slopes, in similar overflow conditions as applicable in the breach formation model presented in this research.

$$\tau_c = 0.163 \cdot I_p^{0.84} \tag{4.17a}$$

$$\tau_c = 0.015(\rho_s - \rho_w)^{0.73} \tag{4.17b}$$

4.4.4. Comparison and selection

The methods above provide four alternatives to calculate the erosion of clay, by combining one of the two erosion formulas with one of either two critical shear stress formulations. Due to the order of magnitude of the expected shear stresses ($\mathcal{O}(10^2)$Pa) compared to the critical shear stresses posed by Whitehouse et al. (2000) and Smerdon and Beasley (1959) (($\mathcal{O}(1)$ Pa), the influence of the critical shear stress is quite small. Consequently, the difference between choosing either formula is small. It is opted to use the formula posed by Whitehouse et al. (2000), simply because this formula was deduced from tests on slopes with a similar steepness to the dike slopes, whereas the equation posed by Smerdon and Beasley (1959) was not.

The influence of the addition of the floc erosion regime (included in the method posed by Prooijen and Winterwerp (2010)) is in most cases negligible, as the shear stresses during any significant overflow rates (> 30 l/m/s) are greater than the shear stresses in the floc erosion regime ($0.53\tau_c < \tau < 1.7\tau_c$). Using Equations 4.17a and 4.17b and input values corresponding to a erosion-resistant clay ($\rho_s = 2650$, $I_p \geq 18$), the floc erosion regime holds for bed shear stresses smaller than $3.4Pa$, whereas typical overflow shear stresses are one to two orders of magnitude larger. The influence of floc erosion therefore is neglected, as far larger overflow rates are needed to damage the grass cover and subsequently expose the clay. Comparison against other erosion methods yielded no viable alternatives, as many methods require an empirical estimation of the erodibility of the soil, reducing accuracy and applicability.

Comparison of this formula against the erosion observed on the clay test section in the Flood Proof Holland test (see Section 3.1) shows promising results. Figure 4.12 shows the measured erosion on two sections of the clay slope and the predicted erosion by the formula posed in Winterwerp and van Kesteren (2004).

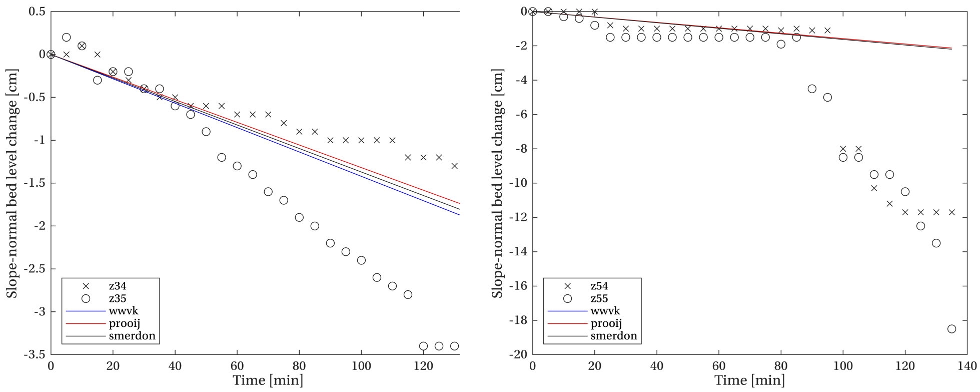

(a) Erosion of clay amidst the slope

(b) Erosion of clay near the toe

Figure 4.12: Overflow-induced erosion of clay on the landside slope of a dike: a comparison of data (Yagisawa, 2019a) and erosion models

4.4.5. Adopted clay erosion method

The method posed by Winterwerp and van Kesteren (2004) seems to provide a lower-limit estimate for the observed erosion during the experiments. This is quite reasonable, as this method was designed to be used for soil with a plasticity index higher than 7, whereas the geotechnical research showed that the soil used in Flood Proof Holland had a somewhat lower plasticity index. In dikes constructed in accordance with Dutch design standards, the plasticity index easily exceeds this value (Technische Adviescommissie voor de Waterkeringen, 1996). Varying clay content and sand lenses are the most likely causes of local deviations in erosion depth, such as observed in figure 4.12b. Especially on the lower end of the test section, the soil was highly heterogeneous and sandy, leading to an underestimation of its erodibility.

Therefore the clay erosion formula posed by Winterwerp and van Kesteren (2004) is adopted, as it is both accurate and simple in its application. It is noted that the estimation or experimental determination of the undrained shear strength of the soil is important to accurately assess the erosion. If no shear strength test results on locally sampled materials are available, it is recommended to use a value in accordance with the undrained cohesion in Dutch standards "NEN-EN 1997 Table 2B: Characteristic values soil properties", preferably selecting a categorisation of the soil based on granulometry and/or other established parameters of which range values are given in this table.

4.5. Headcut initiation and adapted flow regime

As discussed in Section 2.2, a new flow regime develops during erosion of the cover, due to local bed level variation and the localised failure of the grass cover (see Figure 4.10b). The most common criterion for the initiation of headcut erosion is a certain vertical headcut height. Hanson et al. (2005a) defined an initial height of approximately 15 centimetres, d'Eliso (2007) provided a choice between a fixed height equal to 90% of the sward length ($H_{h,i} > 0.9 \cdot L_s$) or the normal depth of flow at the provided overflow rate, but a process-based criterion transition criterion between surface and headcut erosion has not yet been posed. In this study, headcut erosion is assumed to start when the headcut height exceeds the critical depth of flow. This section presents various alternatives to describe the flow regime on an initiated headcut.

The flow is no longer parallel along the surface, but detaches at the top of a headcut, downstream of which a jet of water lands in a turbulent plunge pool, where the bed at point of impact of the jet experiences high jet pressure and the surrounding area is subjected to shear stresses. The complex iterative erosion-stability process, which determines the horizontal migration rate of headcut erosion is often simplified as a function of overflow rate, headcut height and an empirical coefficient. An example of such a formula was presented by Temple et al. (2005) and is shown in Equation 4.18.

$$\frac{dX}{dt} = C_h \cdot (qH_h)^{1/3} \tag{4.18}$$

In which:

- $\frac{dX}{dt}$ is the time-averaged horizontal migration rate of the headcut face $[m/s]$;
- C_h is a headcut coefficient $[s^{-2/3}]$;
- q is the overflow rater per unit width $[m^2/s]$;
- H_h represents the height of the headcut $[m]$.

4.5.1. Existing headcut jet models

Due to the simplified procedure often used to describe the headcut migration rate and the complex turbulence which actually occurs, most models apply an empirical description of the flow in the turbulent plunge pool downstream of a headcut. The BRES-Zhu model (2006) (Zhu, 2006), was the first to include a description of the flow in the plunge pool, including two variants for either an erodible or fixed bottom, depicted in Figures 4.13a and 4.13b respectively. The flow is modelled as a jet with a horizontal initial speed, accelerated vertically through gravity. As the dike is eroded horizontally, the headcut height is at all times assumed equal to the original profile height at the face of the headcut. The stability of the side slopes and headcut face is determined through a momentum balance, and a trapezoidal block is assumed to rotate away from the headcut when stability is lost. The angle of the undercutting face of this block is assumed to be 45° with respect to the horizontal.

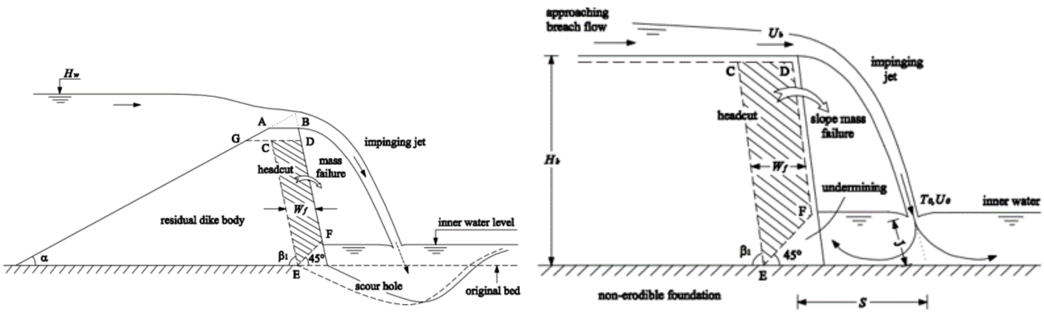

(a) Headcut stability for erodible foundations (b) Headcut stability for non-erodible foundations

Figure 4.13: Schematic drawings of the two-dimensional rotational stability of a headcut as proposed by Zhu (2006)

A simplified process-oriented model was posed by Zhong et al. (2017) for homogenous dikes. The headcut migration rate was described as a function of the headcut coefficient by Temple et al. (2005), as presented in Equation 4.18. The model assumes a horizontal migration of the bottom of the headcut from a predefined starting location and models the process as a horizontal, continuous erosion, rather than a stability failure. The inflow of water is again assumed to be horizontal, neglecting the original profile of the dike, instead assuming the dike to be eroded on the waterside to a flat surface just below water level (see Figure 4.14).

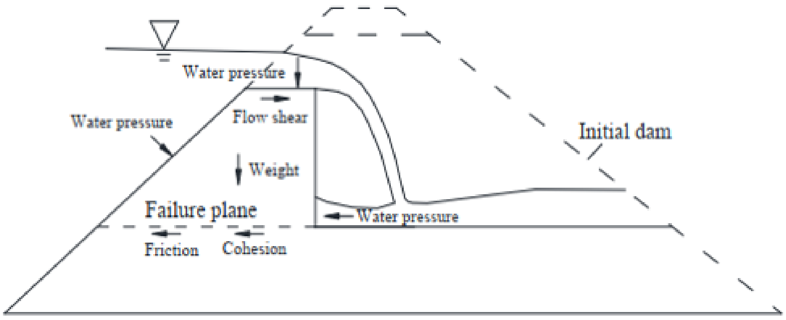

Figure 4.14: Headcut erosion schematised according to Zhong et al. (2017)

The interaction between erosion and headcut stability has been modelled by d'Eliso (2007), as the detailed model presented here includes a definition of the jet, scour downstream of a headcut and various methods to assess the stability of the headcut face. Whereas the schematics indicate the consideration of a sloped surface upstream of the headcut, the flow formulas have not been adapted, when comparing them to Zhu (2006), implying that the effect of the slope angle on flow regime is not mathematically accounted for. The turbulence again is not modelled, but rather, a mean bed shear stress is assumed and variations are described trough the erosion formulas rather than defining a spatial distribution of bed shear stress. Equation 4.19 defines the jet angle as posed by d'Eliso (2007). Figures 2.2a and 2.2b show the stability concepts of the headcut according to D'Eliso.

$$\chi_{D'Eliso} = \tan^{-1}\left(2g \cdot \frac{H_h + h_u/2 - h_b}{v_u}\right) \tag{4.19}$$

4.5.2. Proposed flow regime description - jet impact

The jet flow model applied in this model consists of an adapted description of the jet angle, including the effects of the slope of the dike. on this angle. The formula has been derived from the description of motion of a water particle moving in the jet with an initial velocity along the slope of the dike, which is then vertically accelerated by gravity as it becomes airborne. Equations 4.20a and 4.20b describe the motion of such a particle. Equations 4.20c and 4.20d respectively describe the horizontal distance of the impact point of the jet measured from the face of the headcut and the time the particle travels through the jet to the water surface in the scour hole.

$$z_p(t) = \sin(\beta)\, v_u \cdot t + 0.5 g t^2 \tag{4.20a}$$

$$x_p(t) = \cos(\beta)\, v_u \cdot t \tag{4.20b}$$

$$x_{jet} = \cos(\beta)\, v_u \cdot t_{jet} \tag{4.20c}$$

$$t_{jet} = \frac{-v_u \sin(\beta) + \sqrt{v_u^2 \cdot \sin(\beta)^2 + 2g\left(H_h + 0.5 \cdot h_u - h_b\right)}}{g} \tag{4.20d}$$

As the trajectory of the jet is described through Equations 4.20a and 4.20b, the steepness of the trajectory at the impact point can be used to determine the impact angle of the jet. Equation 4.21 gives the discrete form used to determine the jet angle (χ) in the computational model. The derivative is approximated using the backward Euler numerical scheme.

$$\chi_{jet} = \tan^{-1}\left(\frac{\delta z_p(t_{jet})}{\delta x_p(t_{jet})}\right) = \tan^{-1}\left(\frac{z_p(t_{jet}) - z_p(t_{jet} - \Delta t)}{x_p(t_{jet}) - x_p(t_{jet} - \Delta t)}\right) \tag{4.21}$$

The difference in angles resulting from Equations 4.21 and 4.19 is shown in Figures 4.15a and 4.15b. It becomes clear that the Equation posed by Zhu (2006) and adopted by d'Eliso (2007) in its unadapted form allows for angles of jet impingement smaller than the angle of the dike slope, which is physically impossible. The dike slope angle is indicated in the Figures below by the black horizontal line. It can clearly be seen that (especially for low headcut heights), the method posed by D'Eliso results in significantly lower jet angles than physically possible, as the angle of the dike slope is not included in the equation. Therefore, the adapted jet angle is adopted in the model.

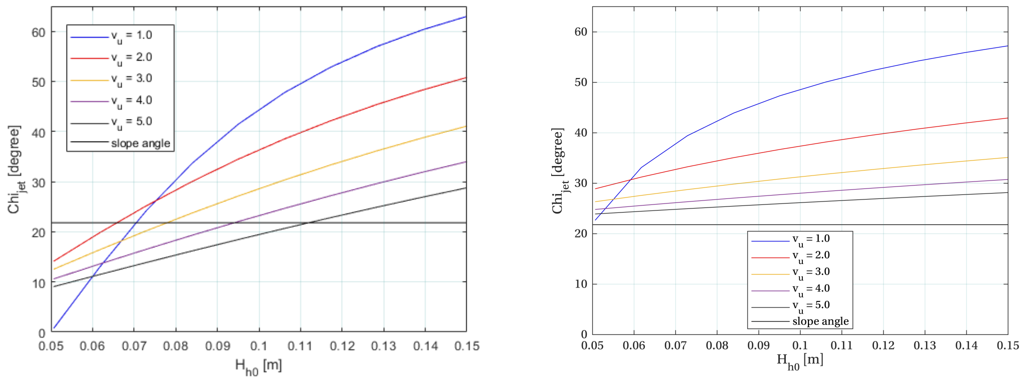

(a) Jet angle according to d'Eliso (2007)

(b) BRAM-model definition of jet angle

Figure 4.15: Jet angle as a function of headcut height and flow speed: a comparison of methods

The trajectories of the jet over a slope with a 1 : 2.5 steepness are plotted for various flow velocities in Figure 4.16. It is observed that for high flow velocities ($u > 2$ m/s and small initial headcut heights (for the cases plotted in Figure 4.16: $H_h = 0.15$m), the jet trajectory barely deviates from the dike slope. This poses an interesting case, as high flow velocities lead to a shorter time-to-failure of the grass cover (see Section 4.3), but due to such a high velocity, the clay layer, which becomes exposed through the local failure of the grass, is not subjected to the jet, as it travels over the exposed grass section. This corresponds well with visual observations in large scale tests, as many irregularities and small damages have often formed before a headcut develops (Bakker and Mom, 2015b). As the exact flow regime here cannot be modelled in the 2d-2d approach chosen in this research, the trajectory of the jet is used to further describe the stress distribution downstream of an initiated headcut. The jetting of a point further downstream causes local erosion, explaining the multi-step headcut profile originally described by Zhu (2006).

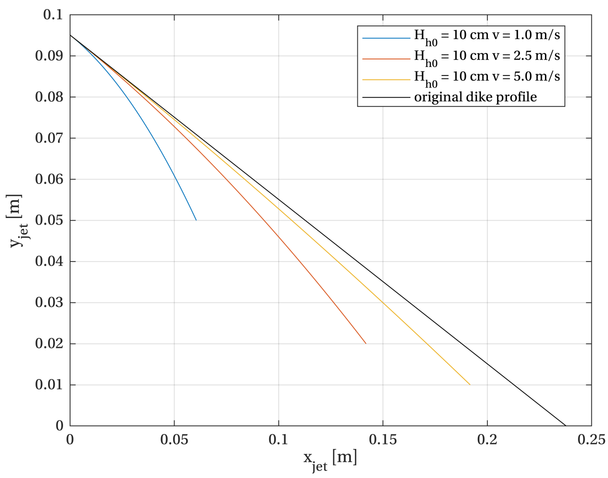

Figure 4.16: Trajectories of cascading headcut flow for various flow velocities over a 15-centimetre high headcut

4.5.3. Proposed flow regime description - jet shear stress

Once the clay cover has failed, the more erodible sand becomes exposed to the jet flow, resulting in a deeper scour hole profile. The position of jet impact can be used to define the shear stress along the bed at the bottom of the headcut face. This distribution is normally assumed to be normally distributed around a mean value underneath the jet (Mazurek, 2001, Nobel, 2013, Rajaratnam, 1976). Strictly speaking, the shear stress is not defined at the heart of the jet flow, as there is no surface-parallel momentum in the centre of the jet. The flow regime during this phase of the breaching process is shown in Figure 4.17.

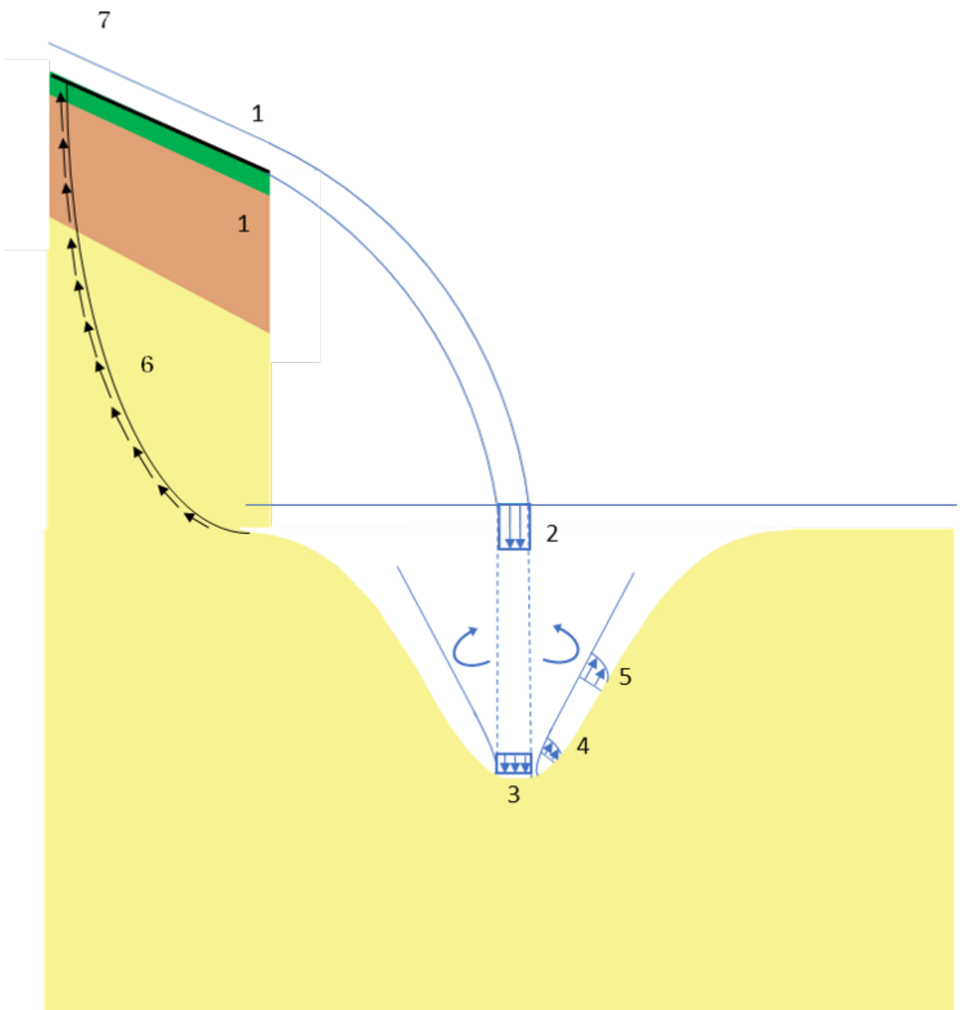

Figure 4.17: Flow regime during scour of the sand

The overflowing water (marked by 1 in Figure 4.17) becomes a turbulent vertical jet penetrating the surface of the water (2). The entrainment of the stationary water in the scour pit causes the jet to widen and the velocity to reduce, until it reaches the bottom of the scour pit (No. 3 in 4.17). At the bottom of the scour hole, the jet is separated in two flows along the bed. It is assumed that: no momentum is lost and the jet enters nearly vertically, and thus the flow velocities at the start of the bottom-parallel flow in either direction are equal to the flow velocity of the jet at its base. As core material is subjected to jetting when the clay layer has been fully eroded, the minimal headcut height is equal to the thickness of the cohesive cover (typically at least 0.5 metres), resulting (through equation 4.21) in a minimum angle of incidence of the jet of 75° (for a relatively high overflow velocity of 3.0 m/s, increasing to up to 85° for a flow velocity of 1.0 m/s). The steepness of this slope shows the assumption of a near-vertical impinging jet is valid. Once the jet reaches the bottom of the scour hole (No. 4 in Figure 4.17), it separates into two equal but opposite surface-parallel flows, as shown before in Figure 2.1. Applying the conservation of momentum, a boundary layer with increasing thickness and decreasing flow velocity is formed along the bottom of the scour pit. No. 5 indicates the development of a logarithmic velocity profile over the boundary layer, leading to a decrease of shear stress on the bed with distance from the axis of the jet. Once the headcut shears along the shear plane (6), the new headcut face lies at the location marked by (7), restarting the process, shifting towards the waterside slope.

The general form of the normally distributed shear stress as a function of the location with respect to the impingement point of the jet is presented in Equation 4.22. To assess the flow velocity and the corresponding bed shear stress, a new Cartesian coordinate system is defined, which follows the jet angle as main coordinate s, and includes a radial distance from the centre of the jet r. Note that the r is a radial distance, and is therefore positive in either direction. The r in equation 4.22 can therefore formally be read as an $|r|$. Figure 4.18 shows the (r,s) coordinate system, which is redefined in the model for adapting jet angle χ_{jet}, keeping the orientation of the s-axis aligned with the direction of the jet.

$$u_{jet}(r,s) = \frac{\sqrt{\frac{C_j}{2}} u_0 D_n}{s} \cdot e^{-C_j \frac{|r|}{s}} \tag{4.22}$$

In which:

- $u_{jet}(r,s)$ is the velocity of flow of the jet on the (r,s)-coordinate system $[m]$;
- C_j is a nondimensional jet dissipation constant, of which the value is discussed below;
- u_0 is the centre velocity of the jet at zero distance in $[m/s]$;
- D_n is the nozzle diameter of the jet (thickness of the flow layer at the jet entry point) $[m]$;
- r is the radial distance coordinate, measured as the absolute distance from the s-axis $[m]$;
- s is the axial distance coordinate, measured as the penetration depth in jet direction from the impact point $[m]$.

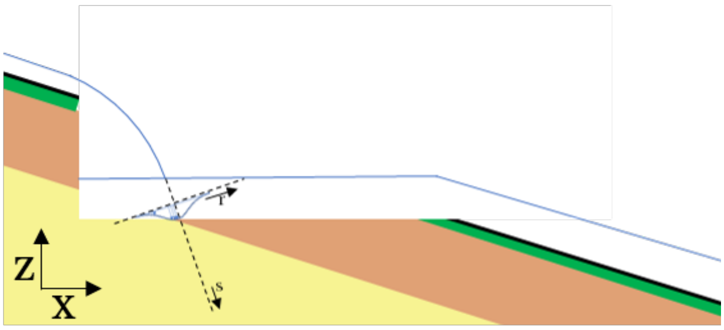

Figure 4.18: (r,s) coordinate system in scour pits

The value of C_j has been experimentally determined in JET tests by various researchers and results have been presented between values of between 50 and 108 (sometimes defined as negative numbers if the exponent in Equation 4.22 is defined as a positive number). Various reports apply two different values for C_j, fitting both the root and the exponential part of Equation 4.22 to experimental data (Albertson et al., 1948, Nobel, 2013, Rajaratnam, 1976). This yields a loss in momentum in s-direction, whereas the rate of widening of the normally distributed flow velocity is based on a momentum conservation. Therefore, this research adopts the value advised by Nobel (2013) ($C_j = 77$) and applies this constant in both the root and exponential part of Equation 4.22, based on a combination of experimental results and the principle of conservation of momentum.

To describe the flow along the bed, the conservation of momentum is applied on infinitesimal sections of the bed, through the method posed by Riteco (2017). Each section is exposed to a normal stress K due to the bending of the jet from one section to the next.

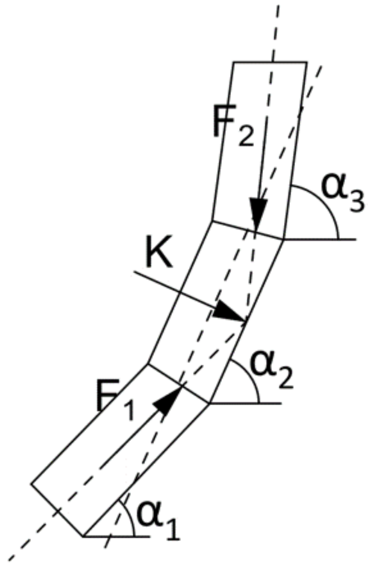

Figure 4.19: Infinitesimal sections of the upward flowing jet (After: Riteco (2017)

The flow in and out of each section can be determined through a volume flux balance and momentum balance per unit width, assuming the initial inflow on point 4 in figure 4.17 to travel at the jet velocity at the bottom of the scour hole and to have a thickness equal to half the jet diameter. Equations 4.23a and 4.23b are solved in an iterative manner to determine the flow velocity and boundary layer thickness along the slope.

$$u_i \cdot A_i + 0.1\overline{u} = u_{i+1} \cdot A_{i+1} \tag{4.23a}$$

$$\rho u_i^2 A_i + \rho (0.1\overline{u})^2 A_{add} = \rho u_{i+1}^2 A_{i+1} - A_{add}\tau \tag{4.23b}$$

The description of the flow along each slice can then be used to determine the stabilising pressure K on the infinitesimal slice, as the shear stresses on the neighbouring slices and steepness of the bed at each slice is known. The stabilising force is given in Equation 4.24a and the depth of failure d_f follows in Equation 4.24c. As long as the depth of failure is smaller than zero, the scour pit is stable. If the depth of failure becomes positive, a wedge of soil with a height equal to the depth of failure is sheared slides to the deepest section of the scour pit.

$$K = F_1 \sin(\beta_1) + F_2 \sin\beta_2 \tag{4.24a}$$

$$(\beta_1 = \alpha_i - \alpha_{i-1}, \beta_1 = \alpha_{i+1} - \alpha_i) \tag{4.24b}$$

$$\sum F = \tan(\phi)\left(\frac{1}{2}\gamma_s \cos(\alpha) d_f^2 + \sigma_0' d_f\right) - \tau_0 d_f + \frac{1}{2}\gamma_s \sin(\alpha) d_f^2 \tag{4.24c}$$

The curvature of the bed level in the scour hole results in curved streamlines, indicating an additional pressure gradient, causing more friction along the bed. Therefore, the existing (empirical) relations to assess the energy loss in a friction coefficient C_f (which are based on steady flow without curvature in its streamlines) underestimate the friction losses in this particular flow regime (Nitsche et al., 1985, Prandtl, 1925). Riteco (2017) estimated the friction coefficient to be equal to 0.0173, based on erosion measurements on 24 JETs on non-cohesive soil, whereas a calculation based on the seventh-power law by Prandtl (1925) (see Equation 4.25 below) indicates a value of only 0.0044 in equal flow conditions. The suggested value by Riteco (2017) is adopted in the breach formation model.

$$C_f = \frac{0.027}{Re_x^{\frac{1}{7}}} \tag{4.25}$$

Using this value for the coefficient of friction, and calculating the flow velocities along the bed of the scour hole using Equation 4.23b, the shear stress along the bed can be calculated, applying Equation 2.1b.

4.5.4. Adopted jet flow description

Current methods describing jet flow are mostly applied in dredging processes and are thus based on submerged jets with high pressures (in excess of 1.0 MPa), whereas the pressures under the cascading headcut jets are relatively low. The low pressures result in entrainment of water at relatively short distances from the water surface, rather than a cutting or undrained failure process of the soil (Miedema, 1987, Nobel, 2013, Rajaratnam, 1976, van Rhee, 2010). The assumption of an initial water depth downstream of the headcut equal to the critical depth and the separation of the jet into two bed-parallel flows based on the conservation of momentum makes it possible to describe the jet flow as a function of the position in the scour pit.

The only situation in which the assumption is formally incorrect, is during the initial moment of scour hole development, where no standing water is present on the exposed sand. Due to the short duration of this period and the fact that the shear stress reduces with scour depth, the resulting error in estimated time-to-failure of a headcut face is considered negligible.

The application of a rotated coordinate system shows a reduction in shear stresses of up to 20%, depending on the angle of the jet. This difference is quite significant for the erosion velocity. Furthermore, the application of a finer coordinate system than applied on the dike as a whole is required to accurately model the shape of the scour pit. The method used to determine the bed shear stresses is validated in combination with the sand scour erosion methods in Section 4.6

4.6. Sand scour

The entrainment of non-cohesive, granular dike material has been described by a wide range of formulas, but their validity is often limited to low Shields' parameters, resulting in a significant overestimation of the erosion in high flow velocities, which occur during breaching. This section compares three methods to determine the erosion velocity, specifically developed for non-cohesive material in high flow velocities, each based on different equations, as posed by van Rhee (2010), Bisschop (2018) and van Damme (2019), respectively.

4.6.1. Existing erosion models

The method posed by van Rhee (2010) was developed to adapt existing erosion relations (most commonly the empirical equation for the pick-up flux as posed by van Rijn (1984)) to be more suitable for high flow velocities, or more specifically: in flow conditions where the Shields' parameter (Θ) is larger than 1.0. The model was developed for use on a flat bed exposed to steady, uniform, turbulent flow.

The method poses an adapted critical Shields' parameter (Θ_c), which includes the effects of the slope angle and the hydraulic gradient due to dilation. Calculating the erosion velocity requires an iterative process, in which the erosion rate converges from an initial estimate (v_{e1}) to a stable value. The iteration process is shown in Equations 4.26a to 4.26d, using the pick-up flux, originally posed by van Rijn (1984). In this research, the assumption is made that the sediment concentration c_b can be neglected, due to the limited length of exposed erodible soil.

$$v_e(1) = v_{e1} \tag{4.26a}$$

$$\Theta_{cr}(i) = \Theta_{cr}\left(\frac{\sin(\phi-\beta)}{\sin(\phi)} + \frac{v_e}{k_l}\cdot\frac{\eta_l-\eta_0}{1-\eta_l}\frac{A}{\Delta}\right) \tag{4.26b}$$

$$\phi_p(i) = 0.00033\cdot D_*^{0.3}\cdot\left(\frac{\Theta-\Theta_{cr}}{\Theta_{cr}}\right)^{1.5} \tag{4.26c}$$

$$v_e(i+1) = \frac{1}{1-\eta_0-c_b}\left(\phi_p\sqrt{g\Delta D}-c_b w_s\right) \tag{4.26d}$$

The second method investigated was posed by Bisschop (2018), describing the pick-up flux of sand in high flow velocities as a function of turbulent 'bursts', which stir up the granular material of a (assumed to be flat) bed, enabling entrainment by the flow. These bursts are vortex-like rotational flows, impinging on the bottom with a velocity equal to half the mean flow velocity parallel to the bed. The bursts are assumed to affect the entire surface of the bed and occur periodically, with a mean period as given in Equation 4.27b. The additional pressure of such a burst dislodges a wedge of sans, which is then partially transported by the flow and partially re-sedimentated by a new burst. The process is shown in Figure 4.20 for a dense sand, showing dilative behaviour (Figure 4.20a) and a loose sand, showing contracting behaviour (Figure 4.20b).

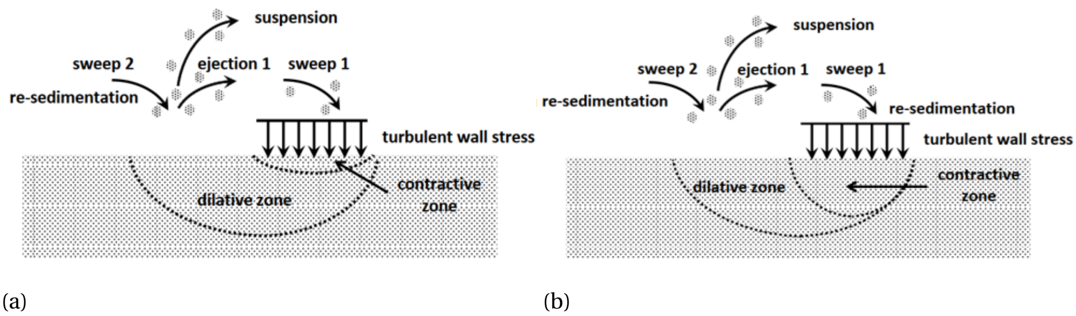

Figure 4.20: Erosion process as determined by ejections and sweeps in case of sand with a high relative density (a) and low relative density (b) (after: Bisschop (2018))

The implicit method describing the pick-up flux by Bisschop (2018) is presented in Equations 4.27a through 4.28e. Equations 4.27a through 4.27e can be used directly, whereas Equations 4.28a through 4.28e require iteration to find the implicit solution. Using an initial estimate for h_s in the order of 0.01 metres the method converges well.

$$\overline{u} = \sqrt{\frac{\tau_b}{C_f\rho_w}} \tag{4.27a}$$

$$T_b = 1.5\cdot\frac{d}{\overline{u}} \tag{4.27b}$$

$$a = \frac{\overline{u}}{T_b} \tag{4.27c}$$

$$w = 0.5\overline{u} \tag{4.27d}$$

$$p' = 0.5\rho_w w^2 \tag{4.27e}$$

The iteration in the method by Bisschop (2018) describes the erosion velocity as a function of the mean bursting period T_b and the eroded depth of a burst h_s, the latter requiring an implicit calculation schema as presented in Equations 4.28a through 4.28e.

$$v_e(i) = \frac{h_s(i)}{T_b} \tag{4.28a}$$

$$i(i) = \frac{v_e(i)}{k_l} \cdot \frac{\eta_l - \eta_0}{1-\eta_l} \tag{4.28b}$$

$$m \cdot A_{sw}(i) = \frac{h_s(i)}{2} \cdot \rho_s(1-\eta_0) \tag{4.28c}$$

$$\sigma'(i) = m \cdot A_{sw}(i) \cdot a \tag{4.28d}$$

$$h_s(i+1) = \frac{p' - \sigma'(i) \cdot \tan(45+\phi/2)}{(N_\gamma g(\rho_i - \rho_w + i(i)\rho_w)} \tag{4.28e}$$

Finally, the method posed by van Damme (2019) requires no empirical factors, but quantifies the erosion of the sand in a fully process-based method, based on the assumption that the erosion rate of the soil, given high shear stresses, is found for the stress balance situation for which the dilatancy induced inflow gives a maximum averaged shear resistance. Contrary to the previous methods, the equations by van Damme (2019) are explicit, however, an optimisation procedure (varying the boundary displacement rate c to maximise the effective normal stress $\overline{\sigma}'$ is required to find the erosion rate, thereby resulting in a similar computational effort. This erosion relation was originally developed for use on lateral erosion on (near)-vertical side slopes of a breach during breach growth.

$$c_z = 2k_{sand}\Delta\frac{1-\eta_l}{\eta_l - \eta_0}\frac{\cos\alpha}{\tan\phi - \sin\alpha} \tag{4.29a}$$

$$d = \frac{\tau_b - (c+c_z)\cdot\Big((1-\eta_0)\rho_s u_* + \eta_i \rho_w u_*\Big) - C}{\tan\phi(\gamma_s - \gamma_w)\cos\alpha + \tan\phi\frac{\gamma_w c}{2k_{sand}}\frac{\eta_l-\eta_0}{1-\eta_l}} \tag{4.29b}$$

$$\overline{\sigma}' = d\Big(\frac{\gamma_w c}{3k_{sand}}\frac{\eta_l - \eta_0}{1-\eta_l} + \frac{1}{2}(\gamma_s - \gamma_w)\sin\alpha\Big) \tag{4.29c}$$

$$v_e = c|_{\frac{\delta d}{\delta c}=0} \tag{4.29d}$$

4.6.2. Comparison of models

The high-velocity sand erosion formulas in the proposed breach formation model (BRAM) are applied in two phases: the scouring of material at the bottom of the headcut, and the lateral erosion of the breach sides by breach flow. Formally, none of the three erosion models suits the unsteady, non-uniform rotational flow in the scour pit and only one of the methods was derived for lateral erosion.

Using the system of equations presented in Subsection 4.5.3 to describe the flow in the jet as bottom-parallel flow over infinitesimal sections and to calculate the resulting bed shear stresses, the validity of each erosion formula can be assessed for the situation of jet scour at the bottom of a headcut. Each method is compared against the erosion observed in small-scale JET tests by Riteco (2017), and the results are shown for six of the tests in Figures 4.21 through 4.23.

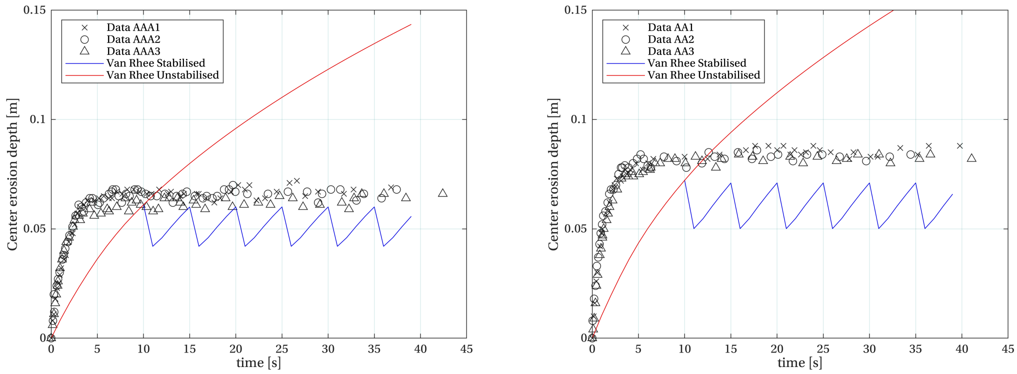

(a) Erosion tests AAA.1-3, $U_0 = 2.9 m/s$, $h_{nozzle} = 0.45 m$

(b) Erosion tests AA.1-3, $U_0 = 3.9 m/s$, $h_{nozzle} = 0.795 m$

Figure 4.21: Comparison of two sets of three erosion test measurements by Riteco (2017) and the erosion method by van Rhee (2010)

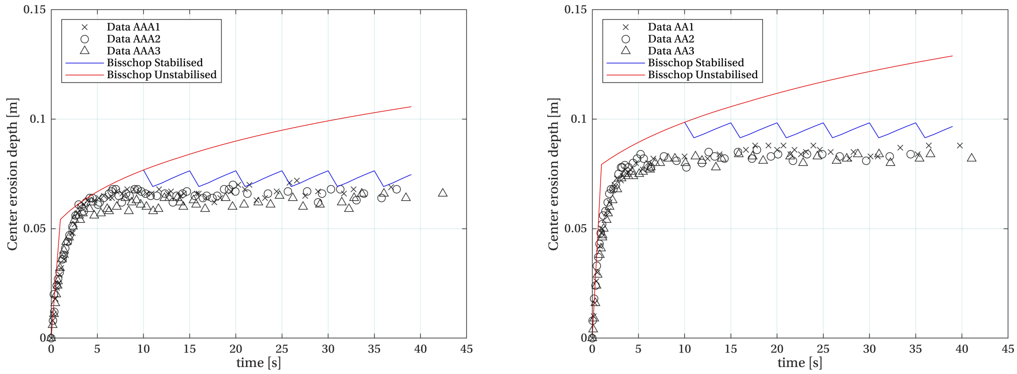

(a) Erosion tests AAA.1-3, $U_0 = 2.9 m/s$, $h_{nozzle} = 0.45 m$

(b) Erosion tests AA.1-3, $U_0 = 3.9 m/s$, $h_{nozzle} = 0.795 m$

Figure 4.22: Comparison of two sets of three erosion test measurements by Riteco (2017) and the erosion method by Bisschop (2018)

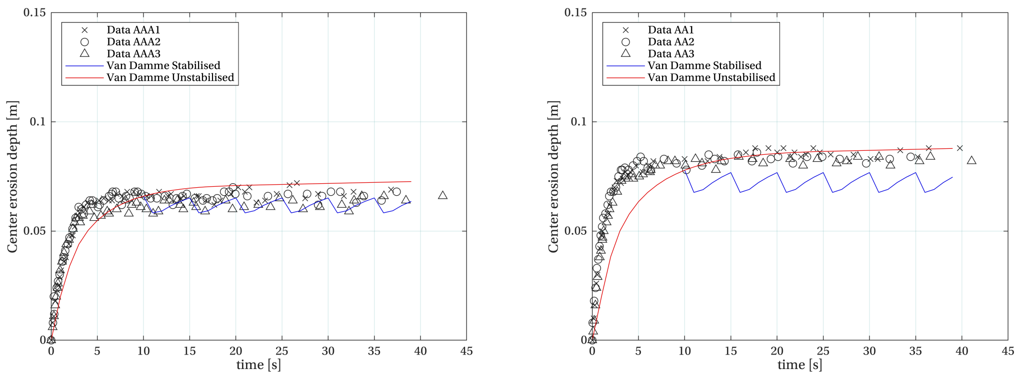

(a) Erosion tests AAA.1-3, $U_0 = 2.9 m/s$, $h_{nozzle} = 0.45 m$

(b) Erosion tests AA.1-3, $U_0 = 3.9 m/s$, $h_{nozzle} = 0.795 m$

Figure 4.23: Comparison of two sets of three erosion test measurements by Riteco (2017) and the erosion method by van Damme (2019)

The method posed by van Damme et al. (2016), applying the stability criterion posed by Riteco (2017) approximates the data quite well. For all models, the time interval between stability checks was set at 5 seconds. The use of a shorter interval leads to smaller variation in the stable situation, however, the first stability check must not be performed during the first seconds to prevent numerical instability. The scour hole shape differs between the erosion methods as well, as their respective sensitivities to shear stress changes is different. The scour profiles are plotted for the AA-series JET tests by Riteco (2017) in Figures 4.24 through 4.26.

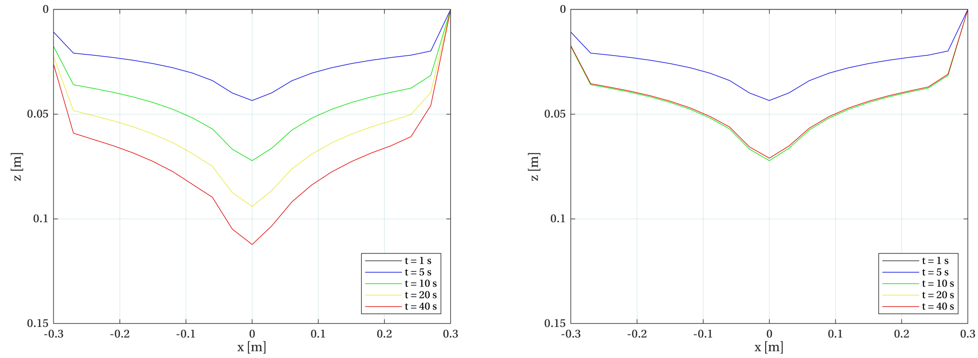

(a) Profile without applying stabilisation criterion (b) Profile applying stabilisation criterion

Figure 4.24: Predicted scour profile development for Riteco (2017) AA test, based on van Rhee (2010)

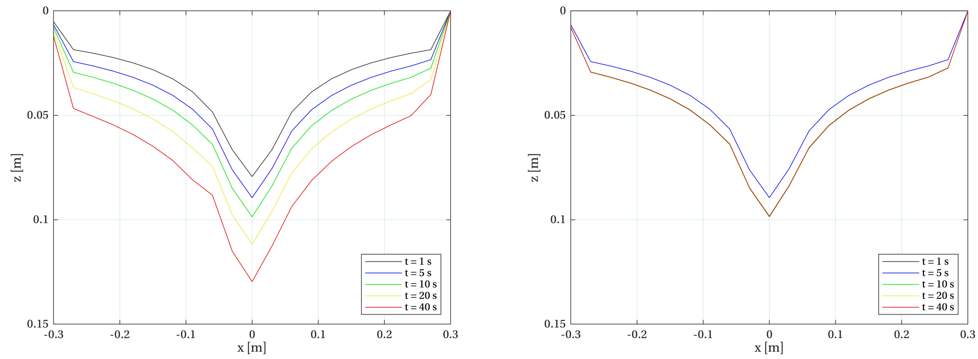

(a) Profile without applying stabilisation criterion (b) Profile applying stabilisation criterion

Figure 4.25: Predicted scour profile development for Riteco (2017) AA test, based on Bisschop (2018)

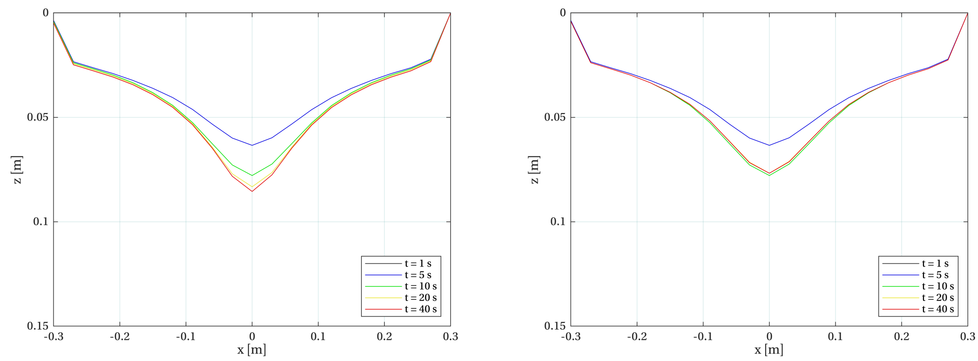

(a) Profile without applying stabilisation criterion (b) Profile applying stabilisation criterion

Figure 4.26: Predicted scour profile development for Riteco (2017) AA test, based on van Damme (2019)

From Figures 4.24 through 4.26, it becomes clear that the influence of the stability criterion on each of the methods is similar. The amplitude of the erosion is damped, and the maximum erosion depth is reached soon, leading to a coincidence of various profiles plotted for $t > 10$ seconds. This corresponds well with the time until the maximum scour depth is reached, as shown in Figures 4.21 through 4.23. Although the maximum depth of the scour pit as predicted by van Damme (2019) is a near perfect fit with the data, the shape of the profile as predicted by Bisschop (2018) resembles the profile observed and described by Riteco (2017) best, as the deepest part of the pit is narrower and steeper than for van Damme (2019). The method by van Rhee (2010) fits the data the poorest, grossly overestimating the data without stability criterion, and underestimating by up to 30% when the stability criterion is applied.

To validate the suitability and give an indication of the typical margin of error of the erosion formulas, all formulas are compared to the erosion measurements of horizontal beds in high flow velocities by Bisschop et al. (2016). The overestimation by the formula by van Rhee (2010) was still quite large, therefore, only the results of Bisschop (2018) and van Damme (2019) are plotted in Figure 4.27.

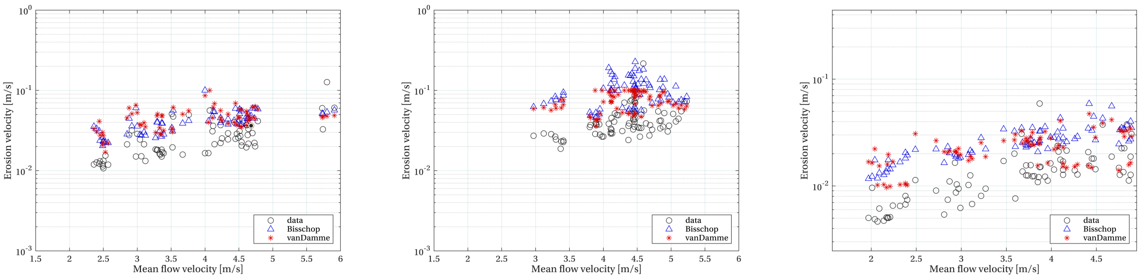

(a) $D_{50} = 125\mu m$ (b) $D_{50} = 262\mu m$ (c) $D_{50} = 594\mu m$

Figure 4.27: Comparison of the erosion methods by Van Damme and Bisschop against the test data by Bisschop et al. (2016)

It becomes clear that both methods approximate the data best for high flow velocities and small grain diameters. This can be explained by the fact that the effects of dilatancy-reduced erosion are strongest for this situation, as the hydraulic conductivity is lowest here.

4.6.3. Proposed jet scour erosion model

This Section described the performance of the models on estimating the jet scour erosion measured by Riteco (2017), the underlying assumptions on the processes at hand and the margins of error observed in a comparison of the methods with the erosion measurements by Bisschop (2018). The most promising models were the models posed by van Damme (2019) and Bisschop (2018). As the process-based description by van Damme (2019) was developed for flow along a (near-)vertical breach slope, this method is used to assess the lateral breach growth. The method by Bisschop (2018) is selected to model the scour pit erosion, as it approximates maximum values during the periodical (quasi-stable) state of the headcut best, and it provides a scour profile closest to the profile observed by Riteco (2017). A secondary benefit of applying this method over the method by van Damme (2019) lies in the fact that the optimisation procedure by van Damme (2019) requires extremely small steps in erosion rate estimates, as the erosion rate during scour is highly variable. The method by Bisschop (2018) converges faster and is more stable for application in this specific case.

4.7. Headcut stability

The scouring due to the impinging jet leads to a predominantly vertical erosion. At the headcut base, however, the upward flow in the scour pit has some residual flow velocity, leading to surface-normal, horizontal erosion of the sand at the bottom of the headcut face. This leads to a decrease in support of the steep headcut cliff, called undercutting, which causes the headcut to lose its stability, the cliff to tumble and the process to move towards the waterside slope. This process is shown in Figure 4.28. Once the headcut migrates past the crest of the dike, the invert height lowers, the overflow rate increases dramatically and the hinterland is flooded. The final part of the dike at the waterside does not erode, but is pushed away by the water pressure as soon as it exceeds the shear resistance of the remaining dike cross-section.

4.7.1. Existing stability models

Existing headcut stability models generally make one of three assumptions.

The simplest empirical models describe a headcut migration rate coefficient, basically linearising the horizontal motion of the headcut (Hanson et al., 2001). These simple models provide a quick order estimate of the migration rate of the headcut and thus of the time until a breach forms. The method posed by Hanson et al. (2005b) is presented in Equation 4.30a. The dimensional headcutting coefficient (C_h, dimensions $s^{\frac{-2}{3}}$) depends on an empirical relation to the erodibility coefficient k_e, given in Equation 4.30b. For non-cohesive soil, the value of K_e ranges between $1-10\frac{cm^3}{l}Ns$. Note that this (non-SI) unit is to be used in Equation 4.30b.

$$\frac{dx}{dt} = C_h(q \cdot H_h)^{\frac{1}{3}} \tag{4.30a}$$

$$C_h = 0.000246k_e \tag{4.30b}$$

More advanced models include an erodible or non-erodible bed and describe the undercutting erosion rate as a function of the jet flow, applying various empirical factors (Zhu, 2006). The rotational stability of the block of soil, which is being undercut provides a discretisation the motion into steps.

The most advanced models consider the vertical erosion downstream of the headcut to be spatially uniform (similar to a surface erosion) and find the horizontal undercutting erosion velocity by multiplying this with an empirical constant d'Eliso (2007). The mass of the soil block losing its support is used as a driving force causing shearing, loss of rotational stability or tensile failure of the clay layer, assuming the soil layers to have some degree of interaction. Figure 2.5 shows this principle.

4.7.2. Stability definition

The proposed model determines the erosion of the sand core of the dike, as described in Sections 4.5 through 4.6, applying a modified Bishop slip stability criterion on the headcut, in which a selection can be made between a linear (Figure 4.28a) and parabolic slip surface (Figure 4.28b).

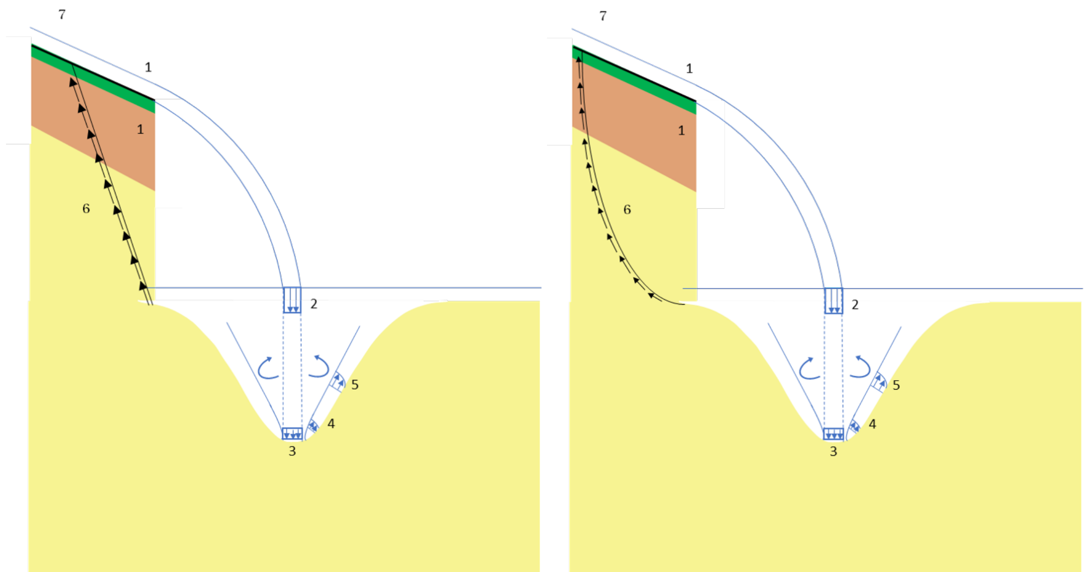

(a) Linear slip surface due to headcut undercutting (b) Parabolic slip surface due to headcut undercutting

Figure 4.28: Modes of slip failure of headcut due to undercutting

The modified Bishop method applies a method of slices, assuming the inter-slice shear forces to be zero. This simplification has been shown to lead to an error in estimating the factor of safety (FOS), representing the ratio between mobilising and stabilising forces, by a few percent (Bishop, 1955). By calculating the FOS for various sections on the slip surface, the representative safety of the entire slip surface can be calculated, through Equations 4.31a and 4.31b. Note that these equations provide an implicit set, as the factor of safety depends on ψ and vice versa, requiring iteration until convergence to a stable solution is found.

$$FOS = \frac{\sum_j \frac{C_c \cdot l_j + (W_j - u_j l_j) \tan\phi_j}{\psi_j}}{\sum_j W_j \sin\alpha_j} \tag{4.31a}$$

$$\psi_j = \cos\alpha + \frac{\sin\alpha_j \tan\phi}{FOS} \tag{4.31b}$$

In this specific application of Bishop's model, various predefined slip surfaces are checked during the undercut erosion of the headcut. The slip surfaces are assumed to start at the bottom of the undercut, and for the parabolic surface, this location is assumed to be the top of the parabola. Other possible slip surfaces would start further down into the scour pit, however, as the infiltration of water in this part of the slope is highly relevant to the stability of such a slip surface and water infiltration is not included in this model, these options were not evaluated. The stability of a range of parabolic and linear slip surfaces is tested, after which the minimal factor of safety can be returned.

4.7.3. Model calibration and sensitivity analysis

The headcut-scour interaction in the model requires a total of 39 input values, of which:

- 13 are fixed (empirical) parameters used in existing formulas, which are set to the advised values;
- 11 are computational parameters, for which a calibration has been done to balance accuracy and computational effort;
- 4 are I/O operators, which tell the model to neglect or account for various effects in the model;
- 18 are physical parameters, for which the user inputs a value, based on the case at hand.

For all empirical parameters used, validation of the respective formula has been done by their respective authors, and reference has been made to the appropriate citations. A level-I sensitivity analysis of the headcut erosion model for all other parameters and toggles has been performed. This means all parameters have been varied one by one. No combinations of parameter variations have been made.

First, the toggles have been used to in- and exclude the effects of a phreatic surface in the dike, to apply or neglect the effect of the jet pressure on scour pit stability (through the equations by Riteco (2017), to select a linear or parabolic slip surface and finally, to select an equation determining the erosion (as described in Section 4.6). It was observed that the model results match the headcut erosion tests best for the following settings:

- The phreatic surface is predefined in accordance with the Dutch standards in overflow conditions, running from the outside water level at the outside crest level of the dike, to 0.10 meters below the landside toe of the dike. Time-dependant variation of this level is not included, as it is assumed that the water level rises sufficiently slow for the dike to saturate up to this level.
- The stability criterion by Riteco (2017) is toggled on, and the stability of the scour pit is analysed every 10 time steps in the model. Higher frequencies of evaluation have been modelled, but have a negligible affect on the headcut erosion rate. (See Table 4.5)
- A linear slip plain is adopted. This resulted in a similar linearised erosion rate as the parabolic slip surface, however, the discretisation provides much smaller headcut lengths, which correspond better to data.
- As further motivated in Section 4.6, the erosion equation posed by Bisschop (2018) is adopted.

Based on these settings, the model was tested for a range of computational parameters. A balance between limited computation time and accurate results was sought after. Table 4.5 shows the selected values of each computational parameter in the final model to all computational parameters and the estimated error resulting from the advised value. The estimated error was calculated by increasing the parameter until the solution stabilised and then determining the percentage change.

Table 4.5: Model sensitivity against computational parameters

Parameter	**Symbol**	**Value**	**Estimated resulting error**
Number of grid points along dike profile	$N_{profile}$	400	10% [3]
Number of slip plane angles tested	$N_{slipangles}$	17	10% [4]
Iterations in determining FOS	N_{bishop}	3	2%
Number of gridpoints monitoring undercut erosion	$N_{undercut}$	20	5%
Time interval between stabilising scourpit	t_{stab}	10	0%
Number of scour profile calculations when scour pit is unstable	N_{stab}	5	0%
Time step size (calculating scour)	dt	10	5%
Number of grid points in secondary grid used for scour pit	$N_{scourpit}$	21	2%
Number of iterations solving the implicit erosion equation	$N_{bisschop}$	10	0%

A sensibility analysis on the time-averaged headcut migration velocity ($\frac{dX}{dt}$) was performed, assuming a basic set of parameters. The results are presented in Table 4.6. It should be noted that an error estimate of approximately 2% due to the discretisation of the grid in the model has been made. The parameters were varied independently. This does not correspond well to the variation of parameters in practice, as some of the parameters are related and can thus not be varied independently in practice.

[3] The sensitivity for the number of points on the profile is strongly related to the magnitude of the time step. The application of a smaller time step leads to no better results, if the number of grid points is not increased sufficiently. For reasonable convergence, it is advised to place grid points approximately 0.10 metres of horizontal distance apart

[4] The number of slip planes results in improved accuracy if the range is confined, requiring no increase of the number of iterations. The tested angles of the slip surface ranged from 5° to 85°, while the resulting failure angle consistently ranged between 60° and 75°

Table 4.6: Model sensitivity against computational parameters

Parameter	Symbol	Reference value	Effect -10% on headcut migration rate	Effect $+10\%$ on headcut migration rate
Mean grain size sand	$D_{50,s}$	$300 \cdot 10^{-6}$	+1%	+1%
Maximum porosity	η_{max}	0.47	−17%	−14%
Initial porosity	η_0	0.37	−7%	+1.5%
Thickness of clay cover	d_{cover}	0.50	+8%	−4%
Cohesion of clay cover	C_{clay}	$10 \cdot 10^3$	+9.5%	−7.3%
Specific discharge overflow	q	0.1	−24%	−29%
Headcut height	H_h	1.0	−37%	+19%
Slope angle	β	1 : 2.5	−16%	+39%
Bulk density of clay	ρ_c	1800	−4%	+5.8%
Friction angle of clay	ϕ_c	25	+6.9%	−5.0%
Friction angle of sand	ϕ_s	35	+2.1%	−1.0%

Some of the results of the sensitivity analysis are as expected, but the model shows some sensitivities that stand out. The sensitivity to the grain size is fairly limited, which can be explained by the principle of dilancy-reduced erosion, during which the bulk properties of the soil dominate the erosion process. The sensitivities to the properties of the clay cover are as expected as well, as the assumption that the clay layer contributes to the shear stress results in a longer time to headcut stability is lost. A less predictable effect lies in influence of the height of the headcut and overflow rate on the headcut erosion process. Increasing or decreasing the headcut height or overflow rate results in a lower horizontal movement of the headcut, compared to the applied reference values. The model shows that for larger headcut height or discharge over the dike, the jet lands so far away from the headcut that the undercut erosion is reduced, while a reduction of the headcut height or overflow rate results in a lower velocity of the jet, slowing the erosion process altogether. An optimum for the horizontal velocity of the headcut is found near the tested reference values.

The effect of the slope angle on the headcut process is similar. For a steep slope (assuming a constant upstream flow velocity, which is not necessarily realistic, as a steeper slope results in a higher velocity of the jet flow), the jet lands relatively close the the headcut, but lacks energy to erode the granular material, while a lower slope moves the impact point of the jet further away from the headcut, reducing the effect of the erosion on the headcut stability (as for higher overflow discharges). A combination of an increased initial velocity with the steeper slope showed an increase of erosion rate, as can be expected, but as a level II sensitivity analysis (testing combinations of parameter changes) for this model requires too many calculations (3^12 > 500.000 tests for only three values per parameter), only a qualitative assessment of these interactions has been made.

4.7.4. Validation of stability method

The stability of the linear slip surface method in combination with the description of the erosion process downstream of a headcut slip circle is tested against the headcut migration tests by Zhao (2013) (see Section 3.4) and Hanson et al. (2001), which are small-scale and large-scale headcut migration tests, respectively. Each of the series of tests was performed in a large flume. The tests by Hanson et al. (2001) consisted of overflowing a large embankment (data in Table 4.7) placed in the flume and observing its horizontal migration rate. An extensive summary of the tests performed by Zhao (2013) is given in Section 3.4.

Table 4.7: Reported test setup Hanson et al. (2001)

Parameter	Symbol	Value	Unit
Headcut height	H_h	1.2	m
Approach flow depth	$d_0 - H_{crest}$	0.2	m
Downstream flow depth	d_p	0	m
Bulk density sand	ρ_{sand}	1800	$\frac{kg}{m^3}$
(Derived) porosity	η_0	0.32	$[-]$
Erodibility coefficient	K_e	7	$\frac{cm^3}{Ns}$
Critical shear stress	τ_c	0.1	Pa

The time-averaged headcut migration rates of the two tests can be estimated from the data. Zhao (2013) reported the residual profiles over time of various tests, from which the movement of a point midway up the height of the cliff is used to determine the headcut migration rate. Only the tests on material with some cohesion can be approximated by the proposed model, as the stability method does not allow for steep stable slopes of sand. The tests by Hanson et al. (2001) report a distance the headcut has moved over time, providing direct data of the migration rate. The resulting graphs by either report are presented in Figure 4.29. Equation 16 in Figure 4.29a shows the linear empirical approximation of the headcut migration by Hanson.

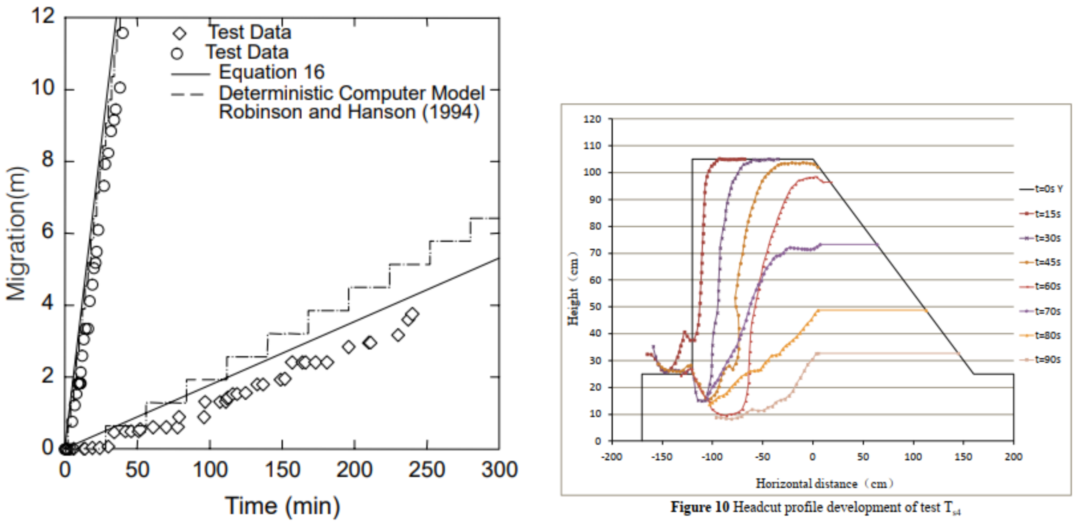

(a) Headcut migration as reported by Hanson et al. (2001)

(b) Residual headcut profiles on various times as presented by Zhao (2013)

Figure 4.29: Reference data on headcut migration experiments

Table 4.8 shows the observed time-averaged migration rates, as well as model results for both the empirical method posed by Hanson et al. (2001) and the proposed model in this research. Note that the method by Hanson et al. (2001) only describes a horizontal rate of movement, whereas the model proposed in this research discretises the process. This results in different time-to-failure estimates for the same dike width, even though the time-averaged erosion rate is similar.

Table 4.8: Modelling the headcut migration rate

Test	Observed migration rate [mm/s]	Migration rate [mm/s] Hanson et al. (2001)	Headcut width BRAM-model [m]	Time-to-failure headcut BRAM-model[s]	Time-averaged migration rate BRAM-model [mm/s]
Hanson et al. (2001)	4.8	5.0	5.0	120	42
Zhao (2013) T_{l1}	3.5 – 30 (average: 14)	1.6	2.2	180	12

4.7.5. Proposed headcut migration method

Applying the new headcut erosion model to the tests by Hanson et al. (2001) and Zhao (2013) shows mixed results. For the tests by Hanson, the erosion is significantly overestimated and the section sliding from the headcut is extremely large. This is likely to be a result of two factors: first, the headcut tested was constructed from sand and lacks the cohesive top layer this model assumes to be present. Second, the flow rate in the test was so large, that the jet flow was drowned and a weir flow developed, resulting in significantly higher shear stresses at the bottom of the headcut, resulting in a different flow regime. The empirical model by Hanson et al. (2001) provides a near-perfect estimate, as it was calibrated based on these tests.

For the test by Zhao (2013), (see Figure 3.22b), the model by Hanson underestimates the erosion by a factor 10. As the predicted erosion rate by the model is predominantly determined by the empirical erodibility coefficient, reported to be $2.2 \cdot 10^{-3}$ cm/s, a poor estimation of this parameter is more likely to be the the cause of estimation errors than the overflow rate and flow depth. The BRAM-model shows a reasonable assessment of the time-averaged migration rate, indicating that the erosion method is applicable, however, the stability criterion again results in a far too gentle slip surface angle, returning a large headcut step size. This again is a result of the assumption in the model that a clay layer is covering the non-cohesive core, which does not apply to this tests. Overall, the scour erosion seems to be accurately predicted by the proposed model, as long as the flow regime matches the jet flow modelled, however, the stability criterion could not be validated successfully, as no headcut experimental data on headcut migration in embankments suitable for the method are available.

5 Case study

In this Chapter, the breach formation model is applied to a case study and the sensitivity of the dike to flooding is discussed. The following case studies are investigated:

- Testcase 1: The Wieringermeerdijk (dike section 12-2) is situated in the area managed by the Water Board Hollands Noorderkwartier and forms the northwest boundary of the IJsselmeer, between Medemblik and Den Oever. Dike section 12 has a minimum safety level of $1:4000$, which means failure of the dike (due to any failure mechanism) may occur once in 4000 years.
- Testcase 2: The Oostvaardersdijk (dike section 8-2): a primary defence situated on the southwest of the province of Flevoland, which retains the water of the Markermeer, managed by Water Board Zuiderzeeland, with a minimum safety level of $1:10,000$.
- Testcase 3: Section 41-2 of the river dike along the Waal, between Deest and Afferden is managed by Water Board Rivierenland. To increase the storage capacity of the flood plains, a new dike section was constructed behind further landward, after which the original section was removed. The new dike now protects the hinterland at a minimum safety level of $1:3000$.

The location of each of the dike sections is shown in Figure 5.1.

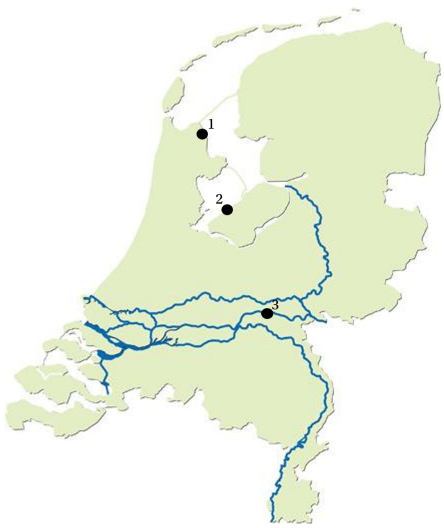

Figure 5.1: The location of each of the case studies, indicated by the numbering as above

In each of the case studies, an overflow rate over the dike of 100 l/m/s is assumed to be present. The return period corresponding this overflow rate is larger than the safety levels indicated for the case at the beginning of this Chapter. The reason for this is that the safety levels indicate the tolerated frequency of failure of the dike. This frequency thus indicates the failure of the dike through any failure mechanism, requiring even larger safety levels for each failure mechanism separately, such as overflow.

As the Dutch safety standards only allow extremely low probabilities of overflow, the modelled situations for all case studies have an extremely low probability of occurrence, but serve to illustrate the difference between the time-to-failures for different dike profiles. The cross-sections of all embankments in the case studies is composed of a grass cover, clay cover and granular core. The qualities of the materials and the shape of the cross-sections differ between the cases.

5.1. The Wieringermeerdijk - Simulating an extreme water level

The Wieringermeerdijk is a primary flood defence, situated between Medemblik and Den Oever. This dike section was last improved in 2014, when the cover of the outer slope of the dike was found to be insufficiently strong. Applying an innovative laser measurement method, the existing cover was scanned and a new cover layer, constructed in asphalt and stone was added over the original cover. The invert level of the dike and quality of the landside slope cover were evaluated and approved in 2011 (Witteveen+Bos). Figure 5.2 shows the cross-sectional profile of the dike and an impression of the state of the dike. The reference line in Figure 5.2a was drawn to represent the mean steepness of the slope (indicated in Table 5.1).

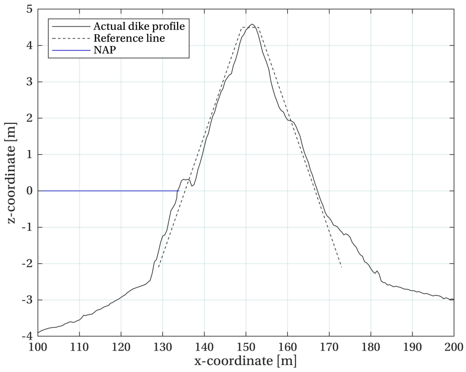

(a) Cross-section

(b) Impression

Figure 5.2: Wieringermeerdijk

5.1.1. Case description

To assess the time-to-failure of the Wieringermeerdijk, an overflow rate of 100 l/m/s is assumed. This corresponds to the overflow rate commonly assumed to lead to failure of a dike (Deltares).

5.1.2. Input data

The failure of the grass cover, clay cover and migration of the headcut to the waterside slope is modelled separately. The tables below indicate the input data used to calculate the time-to-failure for each of the layers.

Table 5.1 shows the input values used to model the grass cover failure process of the Wieringermeerdijk.

Table 5.1: Input values grass cover failure Wieringermeerdijk

Parameter	Symbol	Input value]	Unit
Overflow rate	q	0.1	$[m^3/m/s]$
Landside slope width	x	33	$[m]$
Sward length grass	L_s	0.15	$[m]$
Plasticity index clay	I_p	18	[%]
Landside slope steepness	i_b	1 : 4	$[\frac{m}{m}]$
75th percentile grain size clay	$D_{75,c}$	25	$[\mu m]$
Grass cover factor	C_f	0.6	$[-]$

Table 5.2 shows the input values used to model the failure of the clay cover of the Wieringermeerdijk. Most parameters were estimated, based on the erosion class of the cover and the Dutch tables for normative soil strength values (NEN-EN 1997 table 2b). However, the coefficient of consolidation was estimated from tests on similar material and the undrained shear strength was estimated by an empirical relation posed by Verruijt (2001).

Table 5.2: Input values clay cover failure Wieringermeerdijk

Parameter	Symbol	Input value	Unit
Clay cover thickness	d_{clay}	0.50	$[m]$
Failure depth grass	$H_{h,i}$	0.135	$[m]$
Coefficient of consolidation swell	$C_{v,sw}$	$1.1 \cdot 10^{-7}$	$[m^2/s]$
Undrained shear strength	S_u	10.6	$[kN/m^2]$
50th percentile grain size clay	$D_{50,c}$	2	$[\mu m]$
Clay content	$C_{\%}$	0.5	$[\frac{kg}{kg}]$

Table 5.3 shows the input values used to model the headcut erosion process of the Wieringermeerdijk. The initial headcut height is assumed to be equal to the clay cover thickness when the headcut migration phase starts. These input values were also used to model the lateral breach growth, applying the model by van Damme (2019).

Table 5.3: Input values headcut erosion Wieringermeerdijk

Parameter	Symbol	Input value]	Unit
Median grain size core material	$D_{50,s}$	300	$[\mu m]$
Porosity core material	η_s	0.30	$[-]$
Cohesion clay cover	C_c	10	$[kN/m^2]$
Friction angle sand	ϕ_s	35	[°]
Friction angle clay	ϕ_c	22.5	[°]
Surface area of the polder	A_p	60	$[km^2]$

5.1.3. Results

Table 5.4 shows the results of the case study, modelling the breaching process of the of the Wieringermeerdijk due to overflow. The time-to-failure for each modelled phase is presented. The lateral breach growth process is described by some characteristic values in Table 5.5 and is visualised in Figure 5.3.

Table 5.4: Results case Wieringermeerdijk

Phase	**Time-to-failure proposed model [h]**	**Time-to-failure d'Eliso (2007) [h]**
Grass cover failure	4.3	13.2
Clay cover failure	1.5	1.3
Headcut migration	0.74	0.50
Headcut migration rate [mm/s]	8.6	12.6
Total duration breach formation	6.5	15

The lateral breach growth of the dike was modelled by simulating the flow through from the bosom into the polder as two communicating vessels. Applying the lateral erosion model by van Damme (2019), the lateral breach growth process was describes. Table 5.5 shows the results of this simulation.

Table 5.5: Results lateral breach growth Wieringermeerdijk

Parameter	**Symbol**	**Value**
Peak flow rate $[\cdot 10^3 m^3/s]$	Q_p	11.9
Breach width at peak flow $[m]$	B_p	300
Final breach width $[m]$	B_p	873
Time until 90% of polder volume filled $[h]$	$t_{f,90}$	16
Maximum rise rate of polder level $[m/s]$	$v_{r,max}$	0.0278

Figure 5.3 shows the inflow rate, breach width, and polder water level as a function of time during the lateral breach growth of the Wieringermeerdijk.

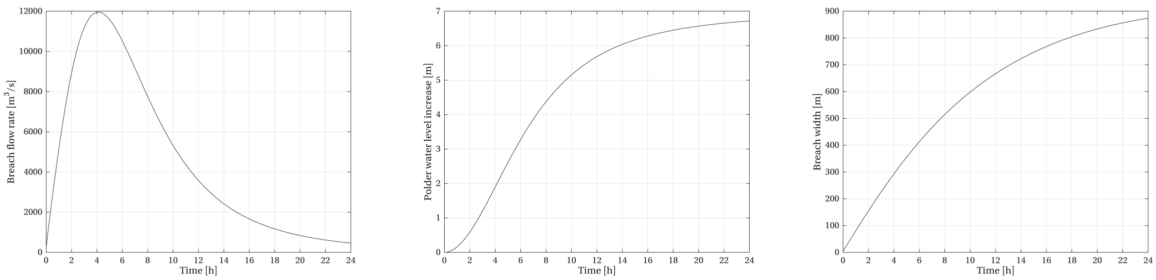

(a) Flow rate (b) Polder water level (c) Breach width

Figure 5.3: Visualisation of results during the lateral breach growth of the Wieringermeerdijk

5.1.4. Conclusion

The time-to-failure estimate for the Wieringermeerdijk by the proposed model is less than half the estimate given by the model by d'Eliso (2007). This is predominantly caused by the extremely large estimate of the time-to-failure of the grass cover by D'Eliso, which is a result of the empirical description of the flow applied by this model. The time-to-failure estimates of the clay cover and headcut migration phases by the two models are quite similar. For both models, the time-to-failure is similar to the typical duration of a storm in the Netherlands (approximately 24 hours, with a peak duration of approximately 2 hours and much shorter than a typical river flood wave (which typically lasts for several days).

5.2. The Oostvaardersdijk - Simulating a combination of failure mechanisms

The Oostvaardersdijk was proposed as a case study by the Water Board Zuiderzeeland for a comparison of the Dutch method of dike design against the method applied by the US Army Core of Engineers. During this case study, the safety of the dike when exposed to various combinations of failure mechanisms was studied, to assess if a probable combination of failure mechanisms could lead to failure of the dike. One of the suggested combinations was a macro-stability issue on the landside slope of the dike and wave overtopping. It was concluded that such a combination was unlikely to lead to failure for the current dike, as the required combination of events leading up to this form of embankment failure was much less probable than failure through a single failure mechanism.

5.2.1. Case description

As the model proposed in this research is posed for overflow, rather than wave overtopping, the time-to-failure of the dike is tested for both overflow and for the combined case, when overflow occurs after a slip circle has caused a headcut to form. The presence of a slip circle makes the case especially viable for this research, as the headcut can be assumed to be initiated by the slip surface rather than the overflow, significantly reducing the time-to-failure and requiring only the headcut-stability model to describe the breaching process. This also changes the input values of the case, as the headcut initiates further up the landside slope, requiring less headcut migration to lead to breaching.

Figure 5.4 shows the cross-sectional profile of the Oostvaardersdijk. The road on the crest of the dike is not taken into account in the stability calculations, however, the sand bed on which the road is placed is considered in the model. The reference line in Figure 5.4a was drawn to represent the mean steepness of the slope (indicated in Table 5.6).

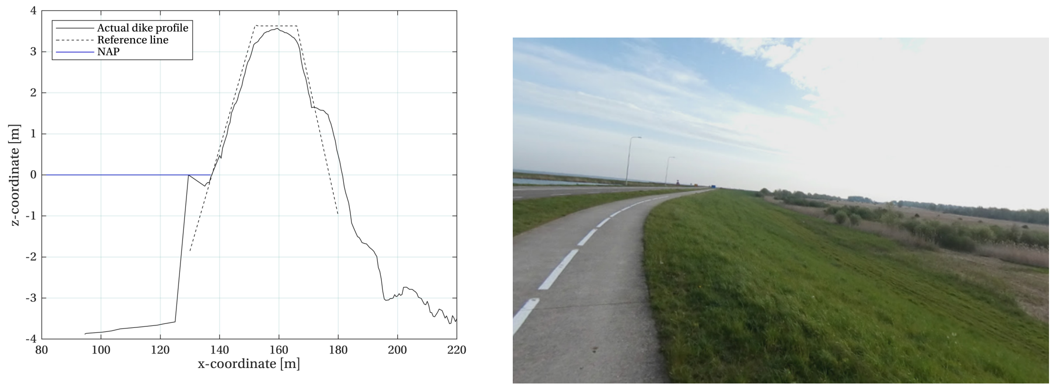

(a) Cross-section

(b) Impression

Figure 5.4: Oostvaardersdijk

5.2.2. Input data

The input parameters used to model the breaching by headcut erosion per phase of the Oostvaardersdijk are given in the following tables. Table 5.6 shows the input values used to model the grass cover failure process of the Oostvaardersdijk. The steepness of the land side slope in most locations is far more gentle than the indicated value, however, the steepest section found from data was selected as normative location.

Table 5.6: Input values grass cover failure Oostvaardersdijk

Parameter	Symbol	Input value]	Unit
Overflow rate	q	0.1	$[m^3/m/s]$
Landside slope width	x	15	$[m]$
Sward length grass	L_s	0.15	$[m]$
Plasticity index clay	I_p	18	[%]
Landside slope steepness	i_b	$1:1.5$	$[\frac{m}{m}]$
75$^{\text{th}}$ percentile grain size clay	$D_{75,c}$	40	$[\mu m]$
Grass cover factor	C_f	0.6	$[-]$

Table 5.7 shows the input values used to model the failure of the clay cover of the Oostvaardersdijk. These values were determined, using the same method as described in Subsection 5.1.2.

Table 5.7: Input values clay cover failure Oostvaardersdijk

Parameter	Symbol	Input value]	Unit
Clay cover thickness	d_{clay}	1.0	$[m]$
Failure depth grass	$H_{h,i}$	0.135	$[m]$
Coefficient of consolidation swelling	$C_{v,sw}$	$2.0 \cdot 10^{-7}$	$[m^2/s]$
Undrained shear strength	S_u	7.9	$[kN/m^2]$
Median grain size clay	$D_{50,c}$	10	$[\mu m]$
Clay content	$C_{\%}$	0.3	$[\frac{kg}{kg}]$

Table 5.8 shows the input values used to model the headcut erosion process of the Oostvaardersdijk. The initial headcut height is assumed to be equal to the clay cover thickness when the headcut migration phase starts. These input values were also used to model the lateral breach growth, applying the model by van Damme (2019).

Table 5.8: Input values headcut erosion Oostvaardersdijk

Parameter	Symbol	Input value]	Unit
Median grain size core material	$D_{50,s}$	300	$[\mu m]$
Porosity core material	$H_{h,i}$	0.35	$[-]$
Cohesion clay cover	C_c	7.5	$[kN/m^2]$
Friction angle sand	ϕ_s	30	[°]
Friction angle clay	ϕ_c	22.5	[°]
Surface area of the polder	A_p	900	$[km^2]$

5.2.3. Results

Table 5.9 shows the results of the case study, modelling the breaching process of the of the Oostvaardersdijk due to overflow. The time-to-failure for each modelled phase is presented. The lateral breach growth process is described by some characteristic values in Table 5.10 and is visualised in Figure 5.5.

Table 5.9: Results case Oostvaardersdijk

Phase	Time-to-failure proposed model [h]	Time-to-failure d'Eliso (2007) [h]
Grass cover failure	1.2	4.5
Clay cover failure	4.6	1.0
Headcut migration	1.3	0.81
Headcut migration rate [mm/s]	6.9	11.3
Total duration breach formation	7.1	6.3

Starting a prescribed headcut location (the assumed location of the slip circle), the headcut erosion model was applied. The average headcut migration rate predicted by the proposed model was approximately 6.9 millimetres per second, whereas the model by D'Eliso predicts almost double that rate, due to the simplified jet scour method. The resulting time-to-failure due to the combination of a slip circle and overflow is quite short, with D'Eliso predicting a time-to-failure of approximately 0.8 hours and the proposed model estimating a time-to-failure of 1.3 hours of the headcut erosion phase. In case no slip circle is assumed to occur, the grass and clay cover fail due to the overflow. This leads to a prediction of the time-to-failure by the models of 6.3 and 7.1 hours by the proposed model and D'Eliso, respectively.

The lateral breach growth of the dike was modelled by simulating the flow through from the bosom into the polder as two communicating vessels. Applying the lateral erosion model by van Damme (2019), the lateral breach growth process was describes. Table 5.10 shows the results of this simulation.

Table 5.10: Results lateral breach growth Oostvaardersdijk

Parameter	Symbol	Value
Peak flow rate [$\cdot 10^3 m^3/s$]	Q_p	48.8
Breach width at peak flow [m]	B_p	1226
Final breach width [m]	B_p	3093
Time until 90% of polder volume filled [h]	$t_{f,90}$	60
Maximum rise rate of polder level [m/s]	$v_{r,max}$	0.0257

Figure 5.5 shows the inflow rate, breach width, and polder water level as a function of time during the lateral breach growth of the Oostvaardersdijk.

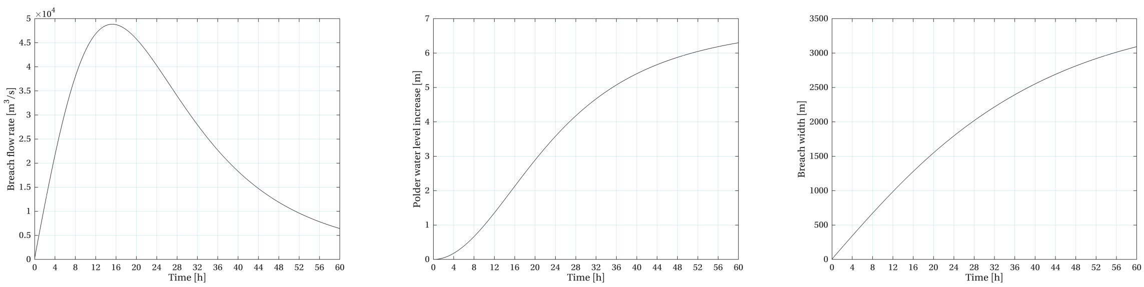

(a) Flow rate (b) Polder water level (c) Breach width

Figure 5.5: Visualisation of results during the lateral breach growth of the Oostvaardersdijk

5.2.4. Conclusion

Both the model by d'Eliso (2007) and the proposed model estimate the headcut migration rate to be in the order of 10^{-3} metres per second, however, the proposed model again estimates a somewhat larger time-to-failure. The main difference between the case of the Oostvaardersdijk and the case of the Wieringermeerdijk is the thickness of the clay cover (which in this case is a factor 2 larger) and the steepness of the landside slope (the Oostvaardersdijk has some steeper sections, which accelerate the flow and lead to failure on slope transitions). The difference between the time-to-failure estimates of the grass cover is smaller for this case, whereas the difference increases for the time-to-failure of the clay cover. This results in an almost equal total duration of the breach formation process between the proposed model and the D'Eliso model for this case.

5.3. The Waal river dike - Simulating a river flood wave

Dike Section 41-2 along the Waal was relocated as part of a flood safety scheme for the river. The project was completed in 1994. This dike section is one of the few areas along the river dike trajectory with a sand core, under a clay layer and grass cover, as dike profiles along this river are mostly constructed completely in clay. The layered structure of this section, makes it a perfect candidate for the proposed model.

5.3.1. Case description

The simulated case again comprises an overflow rate of 100 l/m/s, making the results comparable to the other case studies. In this case, the overflow rate would be caused by an extremely large river flood wave, for which a longer duration is to be expected than for the storms modelled in the other cases. Figure 5.6 shows the cross-section of the Waaldijk and an impression from the crest. The reference line in Figure 5.6a was drawn to represent the mean steepness of the slope (indicated in Table 5.11).

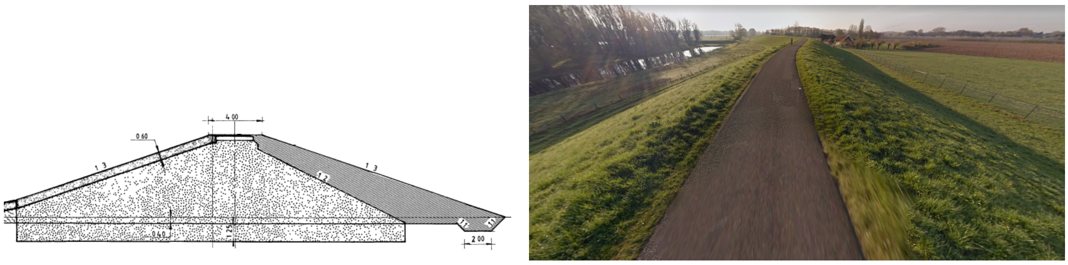

(a) Profile data of the Waal river dike

(b) Impression of the landside slope of the Waaldijk

Figure 5.6: Visualisations of the Waaldijk

5.3.2. Input data

The input parameters used to model the breaching by headcut erosion per phase of the Waaldijk are given in the following tables. Table 5.11 shows the input values used to model the grass cover failure process of the Waaldijk.

Table 5.11: Input values grass cover failure Waaldijk

Parameter	**Symbol**	**Input value]**	**Unit**
Overflow rate	q	0.1	$[m^3/m/s]$
Landside slope width	x	33	$[m]$
Sward length grass	L_s	0.15	$[m]$
Plasticity index clay	I_p	7	[%]
Landside slope steepness	i_b	1 : 3	$[\frac{m}{m}]$
75^{th} percentile grain size clay	$D_{75,c}$	56	$[\mu m]$
Grass cover factor	C_f	0.6	$[-]$

Table 5.12 shows the input values used to model the failure of the clay cover of the Waaldijk. These values were determined, using the same method as described in Subsection 5.1.2.

Table 5.12: Input values clay cover failure Waaldijk

Parameter	Symbol	Input value]	Unit
Clay cover thickness	d_{clay}	0.5	$[m]$
Failure depth grass	$H_{h,i}$	0.135	$[m]$
Coefficient of consolidation swelling	$C_{v,sw}$	$2.0 \cdot 10^{-6}$	$[m^2/s]$
Undrained shear strength	S_u	5.2	$[kN/m^2]$
Median grain size clay	$D_{50,c}$	25	$[\mu m]$
Clay content	$C_{\%}$	0.175	$[\frac{kg}{kg}]$

Table 5.13 shows the input values used to model the headcut erosion process of the Waaldijk. The initial headcut height is assumed to be equal to the clay cover thickness when the headcut migration phase starts. These input values were also used to model the lateral breach growth, applying the model by van Damme (2019).

Table 5.13: Input values headcut erosion Waaldijk

Parameter	Symbol	Input value]	Unit
Median grain size core material	$D_{50,s}$	300	$[\mu m]$
Porosity core material	η_s	0.3	$[-]$
Cohesion clay cover	C_c	5.0	$[kN/m^2]$
Friction angle sand	ϕ_s	35	[°]
Friction angle clay	ϕ_c	27.5	[°]
Surface area of the polder	A_p	268	$[km^2]$

5.3.3. Results

Table 5.14 shows the results of the case study, modelling the breaching process of the of the Waaldijk due to overflow. The time-to-failure for each modelled phase is presented. The lateral breach growth process is described by some characteristic values in Table 5.15 and is visualised in Figure 5.7.

Table 5.14: Results case Waaldijk

Phase	Time-to-failure proposed model [h]	Time-to-failure d'Eliso (2007) [h]
Grass cover failure	1.1	3.4
Clay cover failure	0.7	1.0
Headcut migration	1.1	0.73
Headcut migration rate [mm/s]	7.3	12.5
Total duration breach formation	2.9	5.1

For the grass cover failure and headcut migration phase, the same pattern as in the previous cases persists: the proposed model finds a significantly smaller time-to failure for the grass cover and a somewhat larger time-to-failure of the residual dike profile due to headcut migration. However, in this case, the proposed model predicts a smaller time-to-failure of the clay cover than the model by D'Eliso. This is a result of the lower plasticity index and coarser material of the clay layer, which cannot be modelled in the model by D'Eliso, but negatively affects the time-to-failure in the proposed model. Again, the headcut migration rate is slower in the proposed model by approximately 50%, but the difference in prediction between the models in the first phases is much larger.

The lateral breach growth of the dike was modelled by simulating the flow through from the bosom into the polder as two communicating vessels. Applying the lateral erosion model by van Damme (2019), the lateral breach growth process was describes. Table 5.15 shows the results of this simulation.

Table 5.15: Results lateral breach growth Waaldijk

Parameter	Symbol	Value
Peak flow rate $[\cdot 10^3 m^3/s]$	Q_p	25.2
Breach width at peak flow $[m]$	B_p	633
Final breach width $[m]$	B_p	1890
Time until 90% of polder volume filled $[h]$	$t_{f,90}$	32
Maximum rise rate of polder level $[m/s]$	$v_{r,max}$	0.0075

Figure 5.7 shows the inflow rate, breach width, and polder water level as a function of time during the lateral breach growth of the Waaldijk.

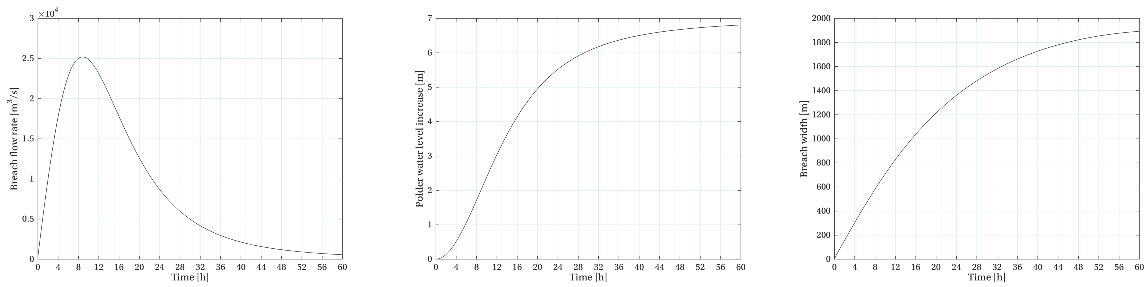

(a) Flow rate (b) Polder water level (c) Breach width

Figure 5.7: Visualisation of results during the lateral breach growth of the Waaldijk

5.3.4. Conclusion

The time-to-failure of the dike due to overflow is estimated to be shorter than for the other dikes by the proposed model, predominantly due to the high sand content of the clay in the cover. This means the particle size of this material is larger and results in a lower plasticity index than in other cases. Although an improvement of the cover material seems like an obvious choice to make the dike more breach-resistant, the use of such an intervention is limited. As the case models a river flood, the flood wave will have a duration of various days. As the time-to-failure of the dike is an order of magnitude lower, it is unlikely that the time-to-failure can be increased until it exceeds the duration of the flood wave. Investments in improving the strength of a river dike against overflow-induced breaching should thus be executed by increasing the invert level of the dike to prevent overflow altogether (as is common practice in the Netherlands).

5.4. Conclusions on case studies

The quality of the clay cover is affects the time-to-failure more significantly than predicted by existing models The results of the case studies show that the predicted duration of breach formation of the dike predicted by the proposed model is similar to the time-to-failure of predicted by D'Eliso. The time-to-failure per element of the dike differs largely. The proposed model assigns more of the residual strength of the dike to the clay cover and granular core material, and significantly less to the grass cover.

Breach formation in dikes with a non-cohesive core material is a brittle failure process in the expected loading conditions The duration of breach formation in all cases is smaller than the expected duration of a storm of approximately 24 hours and far below the typical duration of a river flood wave, which lasts multiple days. Dutch design standards assume the overflow discharge in a storm varies in a trapezoidal shape with a base of 24 and a top of 2 hours. The storm thus only reaching its peak overflow discharge for 2 hours, linearly increasing and decreasing before and after this peak (van Velzen et al., 2007).

The simulated constant overflow rate overestimates the actual load on a dike, but as the time-to-failure estimates by the proposed model are three to eight times shorter than the 24 hour storm duration, the dike is expected to fail during a storm and the failure of the dike can be categorised as brittle failure.

The time-to-failure of a dike in overflow-induced breaching is too short to implement measures before a breach has formed The expected time-to-failure of a dike, as predicted by the proposed model was found to be in the order of 5 – 6 hours (and may vary by an estimated 50%, based on parameter sensitivity analysis), which is insufficient time to find the location of the breach, mobilise equipment and implement measures to prevent breaching. Therefore, emergency measures are best focused on limiting breach growth, as it is unrealistic to assume that measures can be implemented earlier in the breaching process.

Critical design parameters can be identified for the time-to-failure of different dike components The sensitivity analysis of in the model equations in Chapter 3 also showed significant sensitivities of the model in the three modelled phases of breaching. The time-to-failure of the grass cover was affected most by the grass cover factor C_f and Manning's roughness n and n_c. This shows that the grass cover will last longer for a smoother profile and rougher grass, which covers more of the underlying soil. These effects can be physically explained by two physical phenomena. First, longer grass covers the underlying clay better, protecting it from the shear stress imposed by the flow. Second, the roughest part of the cross-section attracts the most shear stress, therefore grass with a higher Manning's roughness will also attract a higher load, thus unloading the cover material.

As the natural growth of grass results in large spatial variability of its strength, these sensitivities are interesting to assess the effect of a normative weak spot in the cover, but provide little means for design, as limited control over these parameters is applied, other than the selection of suitable grass species.

The time-to-failure of the clay cover is most severely influenced by the undrained shear strength of the clay (S_u), its swell coefficient ($C_{v,sw}$) and naturally, the cover thickness and landside slope steepness. The influence of the swelling and undrained shear strength of the clay is partly controllable, but subject to some variation. More manageable parameters are the thickness of the clay cover and slope steepness of the landside slope, a gentler slope and thicker clay cover significantly increasing the time-to-failure (see Chapter 4).

The model bases the breaching process on the assumption that a headcut is formed. For a slope steepness of 1 : 4 and more gradual, the time-to-failure of the cover layers increases rapidly and the variation in erosion velocities along the landside slope is reduced. This makes the initiation of a headcut less likely, as headcut erosion requires a steep slope to develop.

Even when grass cover failure is assumed to lead to headcut formation, headcut erosion is less likely in gradual (steepness 1 : 4 or lower) slopes, as the jet of water downstream of the damaged grass cover patch travels far away from the initiated headcut. Instead of creating a deep the scour hole right next to the headcut face, the jet forms a shallower pit further from the cliff. If the jet travels so far away from the slope that no undercut erosion is observed any more, headcut migration will not occur. (see also the effect for larger flow velocities in Figure 4.21.)

The presented model returns the headcut migration rate as a function of various input parameters. The applied erosion formulas applicable in high flow velocities are most sensitive to the porosity of the sand (or in general: the bulk properties of the sand) and less to the grain properties, to which grain-by-grain erosion formulas are sensitive. Design adaptations from this observation may include the mixing of finer material with the core material, to reduce initial void space and increase the inhibitory effect of dilatancy on the erosion process.

6 Conclusion and Recommendations

In this final Chapter, a conclusion is drawn regarding the research question posed in Section 1.5. In Section 6.1, this conclusion is motivated, followed by a discussion of the research findings and the lessons learned and recommendations on breach formation modelling in Section 6.2.

6.1. Conclusion

The main question this research set out to answer, was posed in Section 1.5 and is repeated below:

In what way does overflow-induced headcut erosion lead to the formation of a dike breach and subsequently to flooding?

The research question consists of two parts. The conclusions in this Section therefore follow the same structure. First, the conclusions regarding the modelling of headcut erosion and breach formation are presented. Second, the conclusions regarding flood risk are drawn. The following main conclusion about modelling dike breach formation by headcut erosion was drawn.

The time-to-failure of a dike due to overflow-induced headcut erosion was shown to be similar to estimates by the existing process-oriented model by d'Eliso (2007). However, the time-to-failure of the components of the dike separately was shown to differ significantly from current estimates. The core material of the dike, which is brought to failure by the headcutting process, was shown to be approximately 50% *larger than estimated by existing models. Due to the relatively small contribution of the core erosion to the total time-to-breaching, the total process duration remains dominated by the failure of the cover material, consisting of a grass cover and clay layer. The proposed model shows the clay cover has a higher time-to-failure of the dike than predicted by existing models, whereas the time-to-failure of the grass cover was predicted to be lower than previously estimated.*

Conclusions regarding breach formation modelling
The most notable progression with respect to the State-Of-The-Art in breach modelling presented in this research is the description of the headcut erosion as a process-oriented scour-stability interaction. The method provides a stress-based (two-dimensional), time-dependant erosion profile of the scour pit, without the need for an assumed ratio between horizontal and vertical erosion.

The process of breaching due to headcut erosion consists of the sequential failure of the grass cover and clay cover, followed by the headcut erosion process. The location of headcut initiation remains a key factor here, as it determines the horizontal distance the headcut migrates until it reduces the invert height to below the water level, leading to breach formation. This location is difficult to predict and is prescribed in the current model, as it is most dependant on the variability of soil strength parameters.

As described in Chapter 4, a wide range of soil parameters influence the time-to-failure of a dike due to head-cut erosion. The influence in porosity of the core material, the steepness of the landside slope angle and the height of the headcut (determined by the cover thickness) are the most relevant design parameters to the headcut migration process. The dependence of the headcut migration rate on these parameters is highly non-linear and is difficult to extrapolate without specifically running a model for the values of interest.

The final conclusion with regard to modelling dike breaching is the following. The presented headcut erosion model has been applied to overflow, but can be expanded to account for other effects, such as the time-varying discharge of wave overtopping eroding the core material. Due to the time-varying overtopping flow velocity, a large variability of the jet trajectory is observed. This subjects not only the core material, but also the grass cover to a jet. Strength definitions for the grass cover and clay cover under jetting need to be added to the model for further improvement of its accuracy.

Conclusions regarding flood risk due to breach formation
To reduce the flood risk in a polder, a more breach-resistant design of a dike can be made, slowing the breach formation process. The sensitivity analysis provided no normative value for design parameters, such as cover thickness or landside slope angle to prevent headcut erosion altogether. However, it becomes clear that a reduction in porosity or permeability of the core material (by mixing in fine material), thickening of the clay layer or, if space is available, a gentler landside slope significantly increases the time until a headcut has formed, thus increasing the time-to-failure of the dike. This provides increased warning time to inhabitants and mobilisation time for mitigative measures.

To determine whether a fully breach-resistant dike can be designed in a specific case, a comparison between the time-to-breaching and duration of the load is made. The horizontal migration velocity of the headcut, as predicted by the model, lies in the order of 10^{-3} to 10^{-2} meters per second. For a typical dike profile (width in the order of 10^{1} meters), this means the time between the initiation of a first headcut and the formation of a breach lies in the order of 10^{3} to 10^{4} seconds or between 0.3 and 3 hours. Adding the time-to-failure of the cover layers, (required to initiate a headcut), a breach-resistant dike design can be made for overflow discharge peaks with a duration up to a few hours.

Finally, assuming a breach forms, the time-to-breaching of a dike is too short to mobilise and implement mitigative measures before a breach has migrated through the crest of the dike. Therefore, mitigative measures must be focused on stopping the breach during the lateral breach growth phase and must therefore be flexible in their size, to fit the expanding breach.

6.2. Recommendations

This Section seeks to pose recommendations on further progressing the State-Of-The-Art in breach modelling. The proposed model makes various assumptions, which can be specified to more detail to improve the description of the breaching process.

The applied scour pit erosion model requires further validation, based on jet tests with an inclined jet
Modelling the scour erosion in the turbulent scour pit requires further improvement of existing erosion formulas and need validation, based on jet tests with an impinging jet under an angle (such as observed during headcut erosion). As the flow velocities in the scour pit (especially near the undercut, which determines the migration rate) reach a wide range of values (from a grain-by-grain pick-up to dilatancy-reduced erosion regime), the accuracy of the erosion method is limited, with measurement error estimates of the data by Bisschop (2018) between 30% and 80% for relatively low flow velocities, reducing to 5% and 30% for flow velocities larger than 4 meters per second. A second improvement to determining the dilatancy-reduced erosion can be made by developing explicit formulations, limiting computational effort, significantly increasing model performance.

The assumption on the headcut migration process must be validated or further detailed by experiments or modelling The modelling of the stability of the scour pit itself can also be optimised to a greater extent: when the headcut migrates, the current model 'resets' the bed level, assuming a new scour pit develops, whereas in reality, the existing scour pit partially collapses, as the jet pressure is moved after headcut failure, resulting in a slightly larger initial depth. As time goes on, the scour pit becomes longer and the supporting soil downstream finally slides, draining the scour pit, increasing the erosion depth and subsequently, the jet velocity due to an increased scour depth (see Figure 4.3).

The effects of water infiltration on the time-dependence stability of a headcut need to be included in modelling The effects of partial saturation and water infiltration can be incorporated in the model to improve the description of the headcut face stability. The inclusion of these effects makes it possible to model the partially saturated core material, which remains stable for steeper slopes than estimated in the proposed model. Infiltration later in the process leads to a smaller stable steepness of the headcut face and thus a loss of stability.

A more dependable method, describing cover failure is needed Finally, the definition of the grass cover failure and resulting location of initiation of the headcut remains a difficult, but relevant problem. The location of the headcut initiation determines the horizontal length over which the headcut must migrate, before breach formation occurs, thereby significantly effecting the time-to-failure of the residual profile during headcut erosion. A purely stress-based approach to defining cover failure would set the headcut location in case of overflow on the dike toe, but weak spots along the slope have shown initiation of headcuts as well and are (due to spatial and natural variability of the grass cover) nearly impossible to predict.

Bibliography

M.L. Albertson, Y.B. Dai, R.A. Jensen, and H. Rouse. Diffusion of submerged jets. In *ASCE, Trans. Paper No. 2409, pp. 639-664.*, 1948.

J. Bakker and R. Mom. Factual report overslagproef wijmeers 2. Technical report, "Flanders Hydraulics", 2015a.

Jan Bakker and Roy Mom. Draaiboek golfoverslagproeven schellebelle. Technical report, "Flanders Hydraulics", 2015b.

Alan W. Bishop. The use of the slip circle in the stability analysis of slopes. *Géotechnique*, 1955.

F. Bisschop and W.G.M. van Kesteren. Vastlegging bestaande kennis squeezingproces. Technical report, Delft Hydraulics, 1994.

Frederik Bisschop. *Erosion of sand at high flow velocities*. PhD thesis, Delft University of Technology, 2018.

Rik Bisschop, Sape A. Miedema, Paul J. Visser, Geert Keetels, and Cees van Rhee. Experiments on the pickup flux of sand at high flow velocities. *Journal of Hydraulic Engineering*, 2016.

H. Blasius. *Grenzschichten in Flüssigkeiten mit kleiner Reibung*, pages 1–37. "Z. Angew. Math. Phys.", 1908.

Astrid Blom. Non-steady flow, 2018.

M.G. Bos. *Long-throated flumes and broad-crested weirs*. "Martinus Nijhoff/Dr W. Junk Publishers", 1985.

Judith Bosboom and Marcel Stive. *Coastal Dynamics I, lecture notes*. "VSSD", 2015.

R.C.M Brekelmans, D. den Hertog, and C. Roos. "Computing safe dike heights: a prototype optimization algorithm". Technical report, CentER, 2009.

Dr.Eng. Stefan Cantre, Jan Olschewski, and Dr.Eng. Fokke Saathoff. Full-scale flume experiments to analyze the surface erosion resistance of dike embankments made of dredged materials. *J. Waterway, Port, Coastal, Ocean Eng.*, 2017.

A. Chézy. Thesis on the velocity of the flow in a given ditch. Technical report, Ecole des Ponts et Chaussées, 1775.

J. Cirkel, C. van Dam, E. van den Akker, and J.W. Nell. Technische eigenschappen van de steenzetting. Technical report, "Deltares", 2018.

Siemes GmbH & Co. Infoblad. Zeefanalyse zand, 2018.

C.F. Colebrook. Turbulent flow in pipes, with particular reference to the trainsition region between the smooth and rough pipe laws. In *Journal of the Institution of Civil Engineers*, 1939.

C.F. Colebrook and C.M. White. Experiments with fluid friction in roughened pipes. In *Proceedings of the Royal Society of London*, 1937.

J.R. Courivaud, F. Laugier, and M.W. Morris. Overflowing erosion modelling of embankment and concrete dams: state of the art and research needs. In *3rd international conference on Protection against Overtopping*, 2018.

Karin de Bruijn, Dennis Wagenaar, Kymo Slager, Mark de Bel, and Andreas Burzel. Updated and improved method for flood damage assessment: Ssm2015 (version 2). Technical report, Deltares, 2015.

A.J.C. Barré de Saint-Venant. Théorie du mouvement non permanent des eaux, avec application aux crues des rivières et a l'introduction de marées dans leurs lits. Technical report, "Comptes Rendus de l'Académie des Sciences", 1871.

Claudia d'Eliso. *Breaching of sea dikes initiated by wave overtopping*. PhD thesis, University of Braunschweig - Institue of Technology, 2007.

Deltares. Definities. http://v-web002.deltares.nl/sterktenoodmaatregelen/index.php/Definities, 2014.

Deltares. Deltadijk. www.stowa.nl/deltafacts/waterveiligheid/innovatieve-dijkconcepten/deltadijk, 2019.

R. García Díaz. Analysis of manning coefficient for small-depth flows on vegetated beds. Technical report, Hydrological Processes 19(16):3221 - 3233, 2005.

P. Dimitriadis, M. Liveri-Dalaveri, A. Kaldis, C. Kotsalos, G. Papacharalampous, and P. Papanicolaou. Zone of flow establishment in turbulent jets, 2012.

Matthijs Duits, Jarl Kind, and Carlijn Bak. "maatschappelijke kosten baten analyse waterveiligheid 21e eeuw". Technical report, Deltares, 2011.

Directive 2007/60/EC of the European Parliament and of the Council on the assessment and management of flood risks. European Union, 2007.

Grondslagen voor Hoogwaterbescherming. Expertisenetwerk Waterveiligheid, 2017.

D.M. Farrar and J.D. Coleman. The correlation of surface area with other properties of nineteen britisch clay soils. *"J. Soil. Sci."*, 1967.

C.B. Field, V.R. Barros, D.J. Dokken, K.J. Mach, M.D. Mastrandrea, T.E. Bilir, M. Chatterjee, K.L. Ebi, Y.O. Estrada, R.C. Genova, B. Girma, E.S. Kissel, A.N. Levy, S. MacCracken, P.R. Mastrandrea, and L.L. White. Climate change 2014: Impacts Adaptation and Vulnerability Part A: Global and Sectoral Aspects. Technical report, IPCC, 2014.

M. Fritz and W.H. Hager. Hydraulics of embankment weirs. *Journal of Hydraulic Engineering*, 1998.

D.C. Froehlich. Embankment dam breach parameters and their uncertainties. *Journal of Hydraulic Engineering*, 2008.

D.C. Froehlich. Predicting peak discharge from gradually breached embankment dam. *Journal of Hydraulic Engineering*, 2016a.

D.C. Froehlich. Empirical model of embankment dam breaching. In *International Conference on Fluvial Hydraulics*, 2016b.

Ph. Gauckler. Etudes théoriques et pratiques sur l'ecoulement et le mouvement des eaux. Technical report, Comptes Rendues de l'Académie des Sciences, 1867.

Peter Geisenhainer and Hocine Oumeraci. Large-scale experiments on dike breachin and breach growth. Technical report, Leichtweiß-Institut für Wasserbau, Technische Universität Braunschweig, 2009.

A. Gyr and W. Kinzelbach. *Sedimentation and sediment transport*, pages 211–220. "Kluwer Academic Publishers", 2003.

G. J. Hanson, K. M. Robinson, and K. R. Cook. "prediction of headcut migration using a deterministic approach". Technical report, "American Society of Agricultural Engineers", 2001.

G. J. Hanson, K. R. Cook, and S. L. Britton. Observed erosion processes during embankment overtopping tests. Technical report, American Society of Agricultural and Biological Engineers, 2003.

G.J. Hanson, K.R. Cook, and S.L. Hunt. Physical modelling of overtopping erosion and breach formation of cohesive embankments. In *Transactions of the American Society of Agricultural Engineers*, 2005a.

G.J. Hanson, D.M. Temple, W.M. Morris, M.A.A.M. Hassan, and K.R. Cook. Simplified breach analysis model. part ii: Parameter inputs and variable scale model comparisons. In *Proc. 25th Annual U.S. Society on Dams Conference Denver*, 2005b.

Oliver. Heijmeijer. High velocity erosion of sand. Master's thesis, Delft University of Technology, 2019.

H.W.M. Hewlett, L.A. Boorman, and M.E. Bramley. Rep r 116 design of reinforced grass waterways. Technical report, "CIRIA", 1987.

Y. Hirabayashi, R. Mahendran, S. Koirala, L. Konoshima, D. Yamazaki, S. Watanabe, H. Kim, and S. Kanae. Global flood risk under climate change. *Nature climate change*, 2013.

HKV and Deltares. Instrumentarium meerlaagsveiligheid, methode, software en toepassing. Technical report, HKV and Deltares, 1956.

Gijs Hoffmans, Gert Jan Akkerman, Henk Verheij, Andre van Hoven, and Jentsje van der Meer. The erodibility of grassed inner dike slopes against wave overtopping. Technical report, Deltares, 2008.

Gijs Hoffmans, Andre van Hoven, Gosse Jan Steendam, and Jentsje van der Meer. Summary of research work about erodibility of grass revetments on dikes. In *3rd International Conference on Protection against Overtopping*, 2018.

B.E. Jones. A method of correcting river discharge for a changing stage. Technical report, "US Geological Survey Water Supply", 1916.

R.J. De Jong. Stroombestendigheid grasmat. Technical report, Waterloopkundig laboratorium, 1970.

Ruben Jongejan and Bob Maaskant. The use of quantitative risk analysis for prioritizing flood risk management actions in the netherlands. In *Congres annual 2013 d l'ACB*, 2013.

S.N. Jonkman. Schattingen groepsrisico's t.b.v. advies deltacommissie. Indicatie omvang groepsrisico's dijkringen Nederland, 2008.

Jarl Kind, Johan Gauderis, Matthijs Duits, and Carlijn Bak. "economisch optimale niveaus voor de bescherming van dijkringen tegen grootschalige overstromingen". Technical report, Deltares, 2011.

F.H. Kulhawy and P.W. Mayne. *Manual on Estimating Soil Properties for Foundation Design*. "Cornell University, Ithaca New York", 1990.

E.W. Lane. Design of stable channels. Technical report, Trans. Amer. Soc. Civ. Engr. Vol. 120, 1955.

R. Manning. On the flow of water in open channels and pipes. Technical report, The institution of civil engineers in Ireland, 1891.

A.G. Mar, V.J.P. De Blocq van Kuffeler, W.J.H. Harmsen, P. Ph. Jansen, G.P. Nijhoff, Th. Thijsse, R. Verloren van Themaat, J.W. De Vries, and L.T. Van der Wal. Rapport deltacommissie. Technical report, De Deltacommissie, 1953.

R. Marsooli and W. Wu. 3-d finite-volume model of dam-break flow over uneven beds based on vof method. *Advances in Water Resources*, 2014.

Kerry Anne Mazurek. *Scour of clay by jets*. PhD thesis, University of Alberta, 2001.

S.A. Miedema. *The Calculation of the Cutting Forces when Cutting Water Saturated Sand*. PhD thesis, Delft University of Technology, 1987.

Voorschrift Toetsen Veiligheid. Ministerie van Verkeer en Waterstaat, 2007.

James K. Mitchell and Kenichi Soga. *Fundamentals of Soil Behavior, third edition*. "John Wiley and Sons, Inc.", 2005.

Mark Morris. Levee breach modeling the hr breach, areba and embrea breach prediction models. USSD Oakland levee workshop, 2015.

Mark Morris, Andreas Kortenhaus, and Paul Visser. "modelling breach initiation and growth ". Technical report, "HR Wallingford", 2009.

M.W. Morris. *Breaching of Earth Embankments and Dams*. PhD thesis, The Open University, England, 2011.

J.A. Muis. Grasmat als Dijkbekleding. Technical report, Technische Adviescommissie voor de Waterkeringen, 1999.

Joannes Mulder. Groepsrisico bij hogedruk aardgasleidingen. https://slideplayer.nl/slide/1982810/, 2009.

W. Nitsche, R. Thünker, and C. Haberland. *Turbulent shear flows*, pages 261–276. Springer-Verlag Berlin Heidelberg New York, 1985.

A.J. Nobel. *On the excavation process of a moving vertical jet in cohesive soil*. PhD thesis, Delft University of Technology, 2013.

N. Pieterse, J. Knoop, K. Nabielek, L. Pols, and J. Tennekes. Overstromingsrisicozonering in nederland. Technical report, Planbureau voor de Leefomgeving, 2009.

L. Ponsioen. Failure processes on the landside slope of a dike. Master's thesis, Delft University of Technology, 2016.

L. Prandtl. Bericht uber untersuchungen zur ausgebildeten turbulenz. *Zeitschrift fur angew. Math. u. Mechanik*, 1925.

B. C. Van Prooijen and J. C. Winterwerp. A stochastic formulation for erosion of cohesive sediments. *Journal of Geophysics*, 2010.

N. Rajaratnam. *Developments in Water Science, volume 5*, pages 1–304. "Elsevier Science Ltd", 1976.

Bart Reeze, Alphons van Winden, Jaap Postma, Roelf Pot, Jochem Hop, and Wendy Liefveld. Watersysteemrapportage Rijntakken 1990-2015. Technical report, Rijkswaterstaat Oost-Nederland, 2017.

Rijksmuseum. https://www.rijksmuseum.nl/nl/pers/persberichten/de-dijkdoorbraak-van-jan-asselijn-te-zien-in-het-rijksmuseum, April 2015.

Rijksoverheid. Organisatie en planning van het implementatieproces ror. https://www.helpdeskwater.nl/onderwerpen/wetgeving-beleid/eu-richtlijn/organisatie-planning, 2018.

Rijkswaterstaat. Dijken. https://www.rijkswaterstaat.nl/water/waterbeheer/bescherming-tege n-het-water/waterkeringen/dijken/index, 2019.

J. Riteco. Effects of water infiltration on soil erodibility. Master's thesis, Delft University of Technology, 2017.

Gerrit Jan Schiereck and Henk Jan Verhagen. *Introduction to Bed, bank and shore protection*. "VSSD", 2016.

H. Schuttrumpf and H. Oumeraci. Layer thickness and velocities of wave overtopping flow at seadikes. *Coastal Engineering*, 2005.

E.T. Smerdon and R.P. Beasley. Tractive force theory applied to stability of open channels in cohesive soils. Technical report, University of Missouri, 1959.

C. Somers. Meetverslag bresgroeiproef zwin, 7 oktober: de trillometingen. Technical report, "Delft University of Technology", 1995.

Grzegorz Stanczak, Hocine Oumeraci, and Andreas Kortenhaus. Laboratory tests on the erosion of clay revetment of sea dike with and without a grass cover induced by breaking wave impact. Technical report, HR Wallingford UK, 2007.

Grzegorz Stanczak, Hocine Oumeraci, and Andreas Kortenhaus. Breaching of sea dikes initiated from the seaside – preliminary model. Technical report, HR Wallingford UK, 2008.

Technische Adviescommissie voor de Waterkeringen. Technisch rapport klei voor dijken. Technical report, Technische Adviescommissie voor de Waterkeringen, 1996.

D. Temple and J. Moore. Headcut advance prediction for earth spillways. Technical report, American Society of Agricultural and Biological Engineers, 1997.

D.M. Temple and G.J. Hanson. Headcut development in vegetated earth spillways. Technical report, Applied Engineering in Agriculture, 1994.

D.M. Temple and G.J. Hanson. Overtopping of grassed embankments. In *Proceedings of the 1998 Annual Conference Association of State Dam Safety Officials, Las Vegas, Nevada, USA*, 1998.

D.M. Temple, K.M Robinson, R.M Ahring, and A.G Davis. Stability design of grass-lined open channels. Technical report, USDA Agricultural handbook, No. 667, 1987.

D.M. Temple, G.J. Hanson, M.L. Neilsen, and K.R. Cook. Simplified breach analysis model for homogeneous embankments: Part i: Background and model components. In *Proc. 25th Annual U.S. Society on Dams Conference Denver*, 2005.

D.M. Temple, G.J. Hanson, M.L. Neilsen, and K.R. Cook. Windam – analysis of overtopped earth embankment dams. In *Proc. American Society of Agricultural and Biological Engineers Annual Int. Meeting St. Joseph MI*, 2006.

T. Terpstra, B. Kolen, and N. Asselman. "investeren in evacueren" wat kost het, wat levert het op?". Technical report, HKV lijn in water and Deltares, 2016.

K. Terzaghi. *Theoretical soil mechanics.* "John Wiley and Sons", 1943.

Le Hai Trung. *Overtopping on grass covered dikes.* PhD thesis, Delft University of Technology, 2014.

Le Hai Trung, Henk Jan Verhagen, and Jentsje van der Meer. Wave overtopping resistance of grassed slopes in viet nam. In *5th annyal Short Conference on Applied Coastal Research*, 2015.

"Operation Manual KSAT". "UMS GmbH", 2012.

USACE. Video material relief breach mississippi. Acquired through Deltares, 2011.

A. Valk. Wave overtopping impact of water jets on grassed inner slope transitions. Master's thesis, Delft University of Technology, 2009.

M. van Damme. A process-based method for predicting lateral erosion rates. Technical report, Delft University of Technology, 2019.

M. van Damme, M. Morris, and M. Hassan. Wp4.4: Rapidly assessing breach driven embankment failures. Technical report, "Flood Risk Management Research Consortium", 2012.

M. van Damme, L. Ponsioen, M. Herrero Huerta, and P. Peeters. Comparing overflow and wave-overtopping induced breach initiation mechanisms in an embankment breach experiment. In *Flood Risk 2016*, 2016.

D. van Dantzig. Economic decision problems for flood prevention. Technical report, Mathematisch Centrum, Amsterdam, 1956.

C. van Rhee. Sediment entrainment at high flow velocity. *Journal of Hydraulic Engineering*, 2010.

L.C. van Rijn. Sediment pick-up functions. *Journal of Hydraulic Engineering*, 1984.

E.H. van Velzen, D. Beyer, H. Berger, C.Greese, and H. Schelfhout. Technisch rapport ontwerpbelastingen voor het rivierengebied. Technical report, "Rijkswaterstaat", 2007.

Dr P. J. Vardanega and Dr. S. K. Haigh. The undrained strength – liquidity index relationship. *Canadian Geotechnical Journal*, 2014.

C.P. Veerman, I.M. Bakker, J.J. van Duijn, L.O. Fresco A.P. Heidema, P. Kabat, T. Metz, Jac.G. van Oord, M.J.F. Stive, and B.W.A.H. Parmet. Samen werken met water. Technical report, De Deltacommissie, 2008.

H.R. Verheij. Technisch rapport erosiebestendigheid van grasland als dijkbekleding. Technical report, Technische Adviescommissie voor de Waterkeringen, 1998.

M. Verlaan, 1993.

N.J. Vermeulen. The composition and state of gold tailings, 2001.

Arnold Verruijt. *Soil Mechanics*. "Delft University of Technology", 2001.

P.J. Visser. *Breach growth in sand dikes*. PhD thesis, Delft University of Technology, 1998.

P.J. Visser, M.J Smit, and D.W. Snip. Zwin'94 experiment: Meetopstelling en overzicht van alle meetresultaten. Technical report, "Delft University of Technology", 1996.

P. Wang, R. Kahawita, D. Mokhtari, T.M. Phat, and T.T Quach. Overflowing erosion modelling of embankment and concrete dams: state of the art and research needs. In *ICOLD Conference, Barcelona, Spain*, 2006.

Charles S. Wasson. *System Engineering Analysis, Design and Development*. "John Wiley and Sons, Inc.", 2016.

M. West, M. Morris, and M. Hassan. A guide to breach prediction. Technical report, "HR Wallingford", 2018.

E. Whitehead, W. Bull, and M. Schiele. A guide to the use of grass in hydraulic engineering practice. Technical report, "HR Wallingford", 1976.

R.J.S. Whitehouse, R. Soulsby, W. Roberts, and H.J. Mitchener. *Dynamics of Estuarine Muds—A Manual for Practical Applications*. Thomas Telford, London, 2000.

J.C. Winterwerp and W.G.M. van Kesteren. *Introduction to the physics of cohesive sediment in the marine environment*. "Elsevier", 2004.

Witteveen+Bos. "projectplan wieringermeerdijk en omgelegde stonteldijk", 2011.

Weiming Wu. Introduction to dlbreach – a simplified physically-based dam/levee breach model. Technical report, "Clarkson University", 2016.

Ir. Junji Yagisawa. Plan of large scale erosion experiment due to overflowing at flood proof holland. Presentation, 2019a.

Ir. Junji Yagisawa. Verification of a predictive formula for critical shear stress with a large scale levee erosion experiment. Preliminary version, 2019b.

J.Y Zhang, Y. Li, and G.X. Xuan. Overtopping breaching of cohesive homogeneous earth dam with different cohesive strength. *Science in China series E: Technological Science*, 2009.

G. Zhao. Experimental observations of headcut erosion during embankment breaching. Technical report, "Delft University of Technology", 2013.

Gensheng Zhao. *Breach Growth in Cohesive Embankments due to Overtopping*. PhD thesis, Delft University of Technology, 2016.

Q. Zhong, S. Chen, and Z. Deng. Numerical model for homogeneous cohesive dam breaching due to overtopping failure. *Journal of Mountain Science*, 2017.

Yong Hui Zhu, P.J. Visser, J.K. Vrijling, and G.Q. Wang. Experimental investigation on breaching of embankments. *Science China - Technological Sciences, January 2011 Vol.54 No.1: p148–155*, 2010.

Yonghui Zhu. *Breach growth in clay dikes*. PhD thesis, Delft University of Technology, 2006.

Glossary

B | C | D | E | F | H | I | J | L | M | O | P | R | S | T | U

B

BRAM Breach Resistance Assessment Model. v, vii, 9, 10, 23, 49, 66, 72, 80, 81

breach formation The erosion process between initial damage to the dike cover and the presence of a breach, which lowers the invert level of the dike to below the MWL. 5, 15, 23

breach initiation The increase of the hydraulic load on a dike, until the first damage to the dike cover can be observed. 5

breaching The process consisting of breach initiation, breach formation and lateral breach growth. 1, 5

C

CBS Centraal Bureau voor de Statistiek. 4, 105

D

dimensionality The number of spatial dimensions used in a model, ranging from zero (no spatial dependence) to three (spatial dependence of phenomena and parameters considered in x,y,z-direction. 20

E

empirical A term used to describe models or (sets of) equations, which are not derived from elementary balance equations, but are based on observations and measurements of (scale) tests. Empirical relations must only be used in situations without significant differences to the situations from which the relations have been derived, as the applicability and margin of error outside these situations cannot be estimated properly. 4, 20, 22

EU European Union. 1

F

failure mechanism The loss of the water retaining function of the dike due to a form of loading exceeding the relevant form of resistance. 2, 4

flooding The inflow of a volume of water into the polder equals the surface area of the polder multiplied by a water depth of 0.20 metres. Only the breach flow is accounted for in calculation, excluding other effects, such as precipitation. This definition is based on the Dutch standard definition of flooding, but more generally applicable.
The Dutch standard definition of flooding states: The unplanned presence of an average water depth of 0.20 metres in the hinterland in at least one area of equal four-digit postal code (based on the zones identified by the Dutch Central Bureau for Statistics (CBS))(Exp, 2017). 4

FPH Flood Proof Holland. 30

H

HE High erodibility. 21

hydraulic jump A transition of turbulent. 15

I

IDM Integral Design and Management. 127

IPCC Intergovernmental Panel on Climate Change. 1

J

JET Jet Erosion Test. 39, 68, 69, 72, 74

jetting The introduction of a water pressure jet to a clay layer. The water pressure penetrates the cracks in the clay layer. 18

L

lateral breach growth The phase following breach formation, in which the breach grows mainly in width. 6, 23
LE Low erodibility. 21
LIR Local Individual Risk. 2

M
ME Medium erodibility. 21
MWL Mean Water Level. 5, 6, 105

O
OT Overtopping. 21

P
P Piping. 21
process-based A term used to describe models or (sets of) equations, which are commonly derived from elementary balance equations and are applicable (in a certain conditions) without the need for empirical fit parameters, based on clear and concise assumptions. Input and output of a process-based model can be physically measured and validated and the formula used try to represent the physical processes as precisely as possible.. 4, 20, 22, 50
process-oriented A term used to describe models or (sets of) equations, which are derived from or based on elementary balance equations and are fitted to observations using minimal empirical fit parameters. Process-oriented models do not necessarily follow the exact processes observed in reality, but try to approximate these (often on larger scales) using simplified formulae.. 9, 20, 22

R
RANS Reynolds-averaged Navier-Stokes. 22, 23, 51
resistance The counteracting force a structure provides during solicitation. 2
rhizomatic Rhizomatic grass forms roots as rhizomes. 17
risk aversion Behaviour of people to lower uncertainty. 2
RWS Rijkswaterstaat. 16

S
SE Systems Engineering. 127, 128
solicitation The load applied to a structure. 2
stolonic Stolonic grass forms roots in the shape of stolons. 17

T
TAW Technische Adviescommissie Waterkeringen. 4, 17

U
USCS Unified Soil Classification System. 26

A

Appendix A - Geotechnical labwork

This appendix describes the results of lab tests conducted on the soil samples taken from the dike section in Flood Proof Holland, studied during overflow conditions. Each section corresponds to a certain test procedure and describes the samples tested, test setup, observations and results and finally the parameters determined, estimated margin of error and the physical meaning of the parameters.

A.1. Samples and storage

All samples were taken from the test section of the Flood Proof Holland levee testing facility, on the locations indicated in Figure A.1. The samples have subsequently been sealed, weighed and stored.

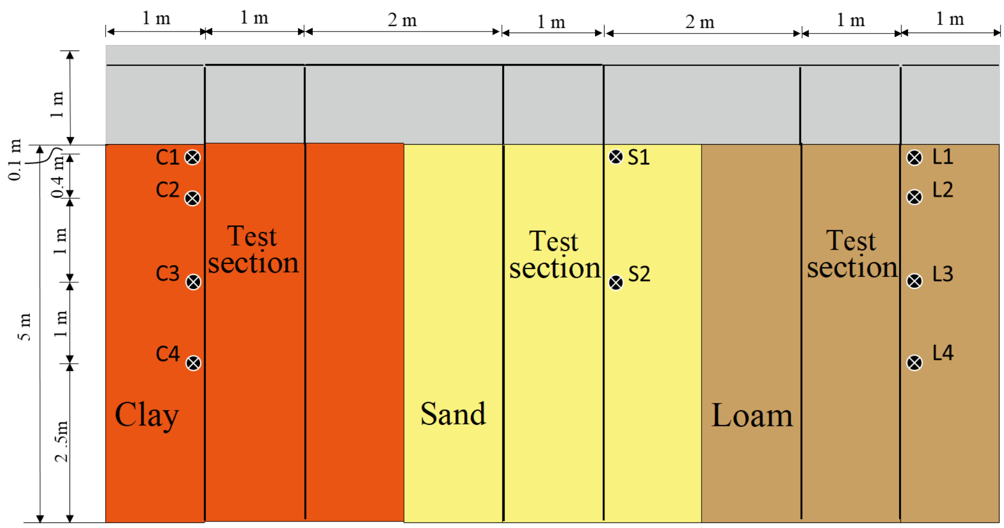

Figure A.1: Locations of samples taken

As the lab facilities of TU Delft were unavailable for two months, the samples were sealed in a double layer of plastic film and stored in a storage bin, which was also sealed by plastic film. The bin was subsequently placed in a basement storage unit, where the environment temperature is fairly constant at around 14 °C. The samples in storage are depicted in Figure A.2.

(a) Sealed samples and bin

(b) Covered bin with temperature measurement

Figure A.2: Storage of the soil samples

To be able to determine the effects of the long duration of storage on the water content of the samples, the samples were weighed before and after storage. It was found that the weigth of the samples had not reduced in any case by more than 0.5 percent during storage and that in some samples the weight had even increased. It is expected that this is the result of measurement errors due to deviations in the exact weight of the packaging, as a representative value was used to calculate the net weight of the sample. A weighing of the empty packaging after testing the soil revealed the weight of the packaging to differ approximately the same as the observed weight increase of the samples. Correcting for this measurement error, all samples showed a small loss of weight, still in no case exceeding 0.5 percent, or, expressed in absolute mass, 5 grams. The in situ water content was determined for a selection of the samples during lab testing. The resulting values are rounded off to the nearest percent and given in Table A.1

Table A.1: Water contents soil samples

Sample	**Gravimetric water content** W_g $[g/g]$	**Volumetric water content** W_c $[m^3/m^3]$
C1	0.28	0.47
C2	0.33	0.56
Average lean clay	0.31	0.52
L1	0.20	0.33
L2	0.18	0.30
Average silt	0.19	0.31
S1	0.15	0.25
S2	0.13	0.22
Average sand	0.14	0.23

A.2. Grain size distributions

To determine the grain size distributions of the different soil samples, the sand was sieved dry and the fine material was sieved wet. The remaining fraction of the lean clay samples with grain diameter < 63μm was subsequently tested in the hydrometer. British standards BS1377: PART 2:1990 were used as a guideline for all three test procedures.

A.2.1. Samples and setup

Three samples of sand (taken from location S1 and S2, and a mixture of the two) were tested. The mesh diameter of the sieves ranged from 63 microns to 1.18 mm (1180 microns). The sieves were enclosed between watertight lids with water in- and outflow hoses and placed on a shaker table, as shown in Figure A.3.

One representative lean clay sample was taken from an even weight of all lean clay samples (C1 through C4) and was used for wet sieving and hydrometer testing to determine the quantities of both the coarse and fine fraction material.

Figure A.3: Wet/dry sieves on shaker table

A.2.2. Test procedure

The dry sieving test for sand was conducted by sieving the material on the shaker table for ten minutes, after which the weight of the sand on each sieve was determined, as well as the weight of lost material. The same method was used for the wet sieving method of the lean clay, but now the water intake was opened to aid the finer particles through the sieves. The resulting separated grain sizes for a sand sample are shown in Figure A.4.

Figure A.4: Separated grain sizes from fine to coarse

One lean clay sample was separated in two parts, based on grain size. All material that passed the 63 micron sieve was dried, all coarse material was sieved in the same sieve stack as used in the dry sieve setup. As no finer sieves were available than 63 micron, all material that passed the 63 micron sieve was lost. According to the standards, this lost material should be noted for sand samples, whereas for lean clay samples, the material should be added to the settling tube for the hydrometer test. To account for the lost mass of the remaining fine fraction in the lean clay sieving, the lost mass was determined and the hydrometer results were scaled to represent all fine material. The results of the grain distribution of the lean clay are therefore based on the assumption of a uniform distribution of the fines through the sample. The fine material was subsequently suspended in demineralised water and the quantity of dike construction material in suspension was measured over time using a calibrated hydrometer. Assuming spherical grains in a viscous fluid, the percentage of the material smaller than any grain size was determined, based on Stokes' Law.

A.2.3. Results and observations

The average grain size distribution for the sand resulting from the three tests was determined. The grain size distribution of the sand is plotted and compared against the grain size distributions given by the inspection of the material in Figure A.5.

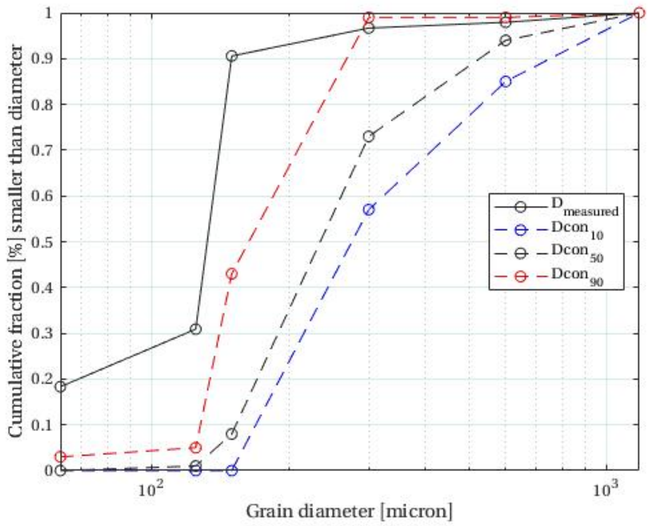

Figure A.5: Grain size distribution sand

The grain size distribution of the lean clay was determined, based on wet sieving and a hydrometer test, in which the fine material (d < 63 micron) settled in demineralised water, preventing flocculation. The suspension is shown in Figure A.6.

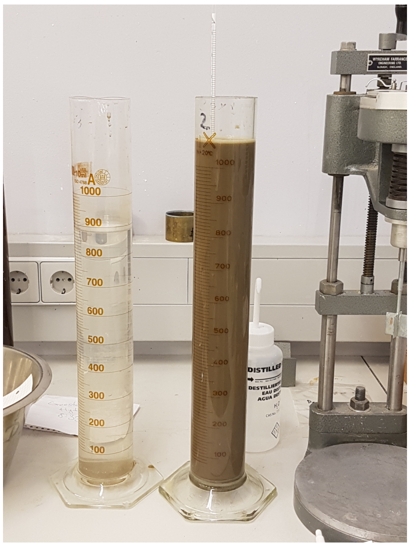

Figure A.6: Suspended lean clay in settling tube

The combination of the wet sieving and hydrometer test results in the grain size distribution given in Figure A.7.

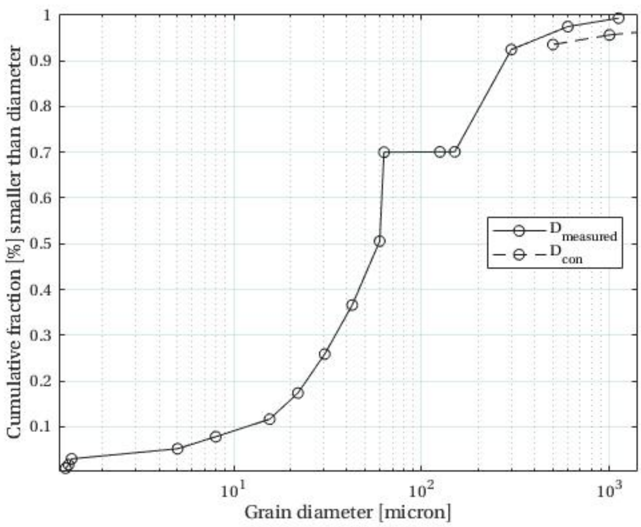

Figure A.7: Grain size distribution lean clay

The silt used in the dike was reported to be a uniform mixture, of equal weight parts lean clay and sand. Yagisawa (2019a) Therefore, the grain size distribution of the silt was found by taking the weighted average of the grain size distributions for each of these materials. The resulting distribution is plotted in Figure A.8

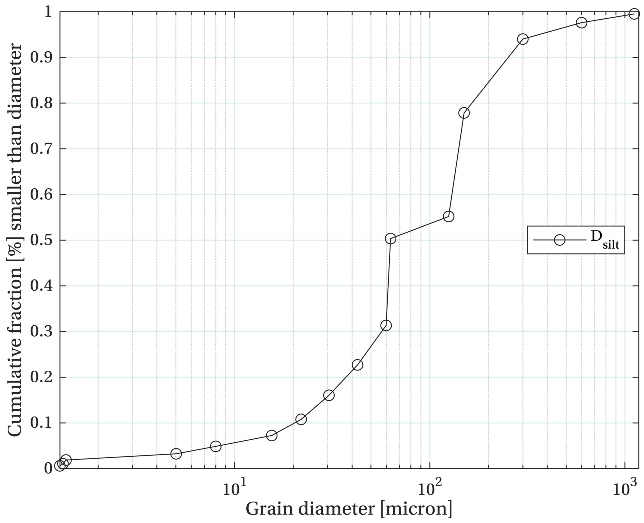

Figure A.8: Grain size distribution silt

A.2.4. Analysis

Various characteristic grain sizes can be used to determine the stability of the grains or to estimate the permeability of a soil. Table A.2 shows these typical grain sizes and ratios for the three soils tested.

Table A.2: Grain sizes

Parameter	**Unit**	**Sand**	**Silt**	**Lean clay**
D_{10}	$[\mu m]$	108	21	7.4
D_{50}	$[\mu m]$	198	119	37
D_{60}	$[\mu m]$	223	130	58
$\frac{D_{60}}{D_{10}}$	$[\frac{g}{g}]$	2.1	6.4	7.8
Fraction $D < 63\mu m$	$[\frac{g}{g}]$	0.0079	0.43	0.68
Fraction $D < 2\mu m$	$[\frac{g}{g}]$	-	0.021	0.034

A.2.5. Conclusion

The observed grain sizes of the sand are significantly smaller than reported by the inspection. Two possible causes have been identified. 1) the material has been sorted during transport or placement at the site, which would cause the larger particles to be placed deeper, not showing up in the samples, which were taken at depths less than 0.5 meters. 2) The grain sizes have been overestimated by the inspection, as the sieve analysis was performed using less different sieve diameters. The poor grading of the soil ($\frac{D_{60}}{D_{10}} < 4$) is likely to result in large void ratios and large permeability.

The grain sizes of the silt and lean clay are as expected. According to Skempton and Bishop (1985), a minimum clay content of approximately 15% prevents inter-particle contact, resulting in a clay-dominated behaviour. The clay contents of both cohesive materials are far smaller. The small fraction of clay particles in the silt (2.1% of mass) and the lean clay (3.4% of mass) indicate that these soils are not dominated by clay behaviour, but exhibit behaviour of granular material as well. As the cohesive soils are well-graded, their permeability is expected to be significantly lower. (see Section A.5.

A.3. Void ratios (sand)

The void ratio of a soil is defined as the ratio between the volume of voids and the volume of solids, as given in Equation A.1.

$$e = \frac{V_v}{V_s} \tag{A.1}$$

A.3.1. Samples and setup

To assess the maximum void ratio, oven-dry sand was dumped in a standardised mold from the specified height. The procedure was repeated for various samples, taken from locations S1 and S2. To determine the minimum void ratio, the same sand samples were dumped in the mold and compacted.

A.3.2. Test procedure

The minimum and maximum void ratios of the sand were determined, following BS1377 part 4 - 1990. Based on the poor grading of the sand, both the minimum and maximum void ratio were expected to be quite large.

A.3.3. Results and observations

The minimum and maximum void ratio were each tested five times. The number of compaction blows was increased to 100 blows (compared to the 40 blows indicated by the standards), as preliminary tests indicated significant further compaction after the prescribed procedure (a further void ratio reduction from 0.77 to 0.66), meaning that the sample had not been compacted to its minimum void ratio.

Table A.3 indicates the observed minimum and maximum void ratio measurements.

Table A.3: Minimum and maximum void ratios of FPH sand

Void ratio type	**Measured void ratios** [V_v/V_s]	**Average void ratio** [V_v/V_s]
Minimum void ratio	1.10, 1.06, 1.09, 1.08, 1.09	1.08
Maximum void ratio	0.66, 0.65, 0.65, 0.66, 0.66	0.66

A.3.4. Analysis

The void ratio can be converted to a porosity. The resulting minimum void ratio of 0.66 (corresponding to a porosity $n = 0.40$) is rather large, as is the resulting maximum void ratio of 1.08 (corresponding to a porosity of 0.52).

A.3.5. Conclusion

Due to the poor grading of the sand (high uniformity of the grain sizes), both the minimum and maximum porosity of the sand are quite large for a sand. This is the result of a lack of finer particles, which fill a part of the void space, when mixed properly. Due to a shortage of these particles and the presence of many sand particles of approximately equal size ($100 > D150\mu$m), the void space between the grains remains quite large, even when compacted. As a result of this open space the sand is likely to have a relatively large hydraulic conductivity and a low volumetric weight, making it susceptible to seepage and liquefaction.

A.4. Atterberg limit tests

The plastic limit (L_p) and liquid limit (L_l) were determined through a crumble test and fall-cone test, respectively. The exact procedures followed can be found in ISO/TS 17892-6: 2004.

A.4.1. Samples and setup

Three series of tests were performed, one in which only the fine fraction was used ($< 63\mu$m) and two others on a lean clay and silt sample, respectively.

In preparation of the Atterberg limit tests on the fine fraction, a lean clay sample was sieved to acquire only the particles with a diameter smaller than 63μm. Half of this sample was subsequently used to determine the liquid limit (L_l) of the clay in a fall-cone test, the other half of the sample was used to perform a crumble test, determining the plastic limit (L_p).

A.4.2. Test procedure

The fall-cone test was performed by evenly saturating the soil sample and dropping a cone with a weight of 80 grams into the sample from the fall-cone setup. After five seconds, the cone was fixed in place, after which the displacement was measured. The test setup is depicted in Figure A.9.

Figure A.9: Liquid limit test setup

The plastic limit was determined through the crumble test, during which thin threads of material were rolled, until crumbling occurred. Figure A.10a shows the initial thread with a thickness of 6.0 mm. Figure A.10b depicts the thread of 3.0 mm at the moment of crumbling.

(a) 6 mm thread before rolling (b) 3 mm thread crumbling

Figure A.10: Execution of the Plastic limit test

A.4.3. Results and observations

The fall-cone test results are shown in Figure A.11. The liquid limit (L_l), expressed as a percentage of total mass of the saturated fines, is found at $31m\%$ water content for the. Converted to volumetric water content, the liquid limit lies at $51V\%$. No post-sinking of the cone was observed during the test.

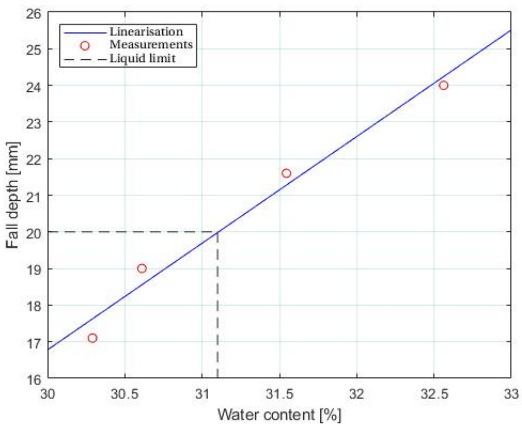

Figure A.11: Determination of the Liquid limit of the fine fraction

An overview of the crumble test results is given in Table A.4. The plastic limit (L_p), expressed as a percentage of total mass of the saturated fines, is found at $22m\%$ water content. Converted to volumetric water content, the plastic limit lies at $37V\%$.

Table A.4: Example of test results from Plastic limit test (performed on the fine fraction)

Clay sample	Subset no.	Wet weight $[g]$	Dry weight $[g]$	Plastic limit $[m\%]$	Plastic limit $[V\%]$
C1	1	8.81	6.83	22.47	37.1
C1	2	9.12	7.02	23.03	38.0
C3	3	9.59	7.49	21.9	36.1
C3	4	9.61	7.52	21.7	35.9
Average	all			22	37

The quantity of fine particles present in the sample significantly affect the plastic and liquid limits of the soil in its in situ composition. Table A.5 gives an overview of the plastic and liquid limits for the fine fraction and for the in situ samples.

Table A.5: Overview of resulting Atterberg limits

Material	Liquid limit $[m\%]$	Plastic limit$[m\%]$	Plasticity index$[m\%]$
Fines	31	22	9
Lean clay	28	20	8
Silt	23	18	5

A.4.4. Analysis

Using Equation A.2, the plasticity indices of the samples were determined. The resulting plasticity indices are presented in Table A.5. The clay used during the overflow test can be classified as a medium-plastic clay ($7 < I_p < 17$), whereas the silt has a low plasticity ($I_p < 7$).

$$I_p = L_l - L_p \tag{A.2}$$

From the plasticity index of the fine fraction, the activity of the clay particles (A_c) can be derived, using Equation A.3. In this equation, C_c stands for the fraction $[-]$ of the particles smaller than $2\mu m$ (lutum fraction). For the tested samples, which only contain the material passing the 63μm sieve, this fraction is approximately 0.16, resulting in an activity of the clay of 0.9.

$$A_c = \frac{I_p}{C_c * 100} \tag{A.3}$$

Based on the observed grain diameters in the hydrometer test and the Atterberg limits determined in these tests, the clay particles in the soil are predominantly Kaolinite, characterised by a low activity and low Atterberg limits. The activity of Kaolinite is low (0.5), whereas the activity found for the clay sample is somewhat higher. This indicates the presence of a smaller fraction with a large activity, likely to be Montmorillonite, which is a common mineral with higher activity. Mitchell and Soga (2005).

The in-situ state of the erosion test sections can be described by the consistency index, a normalisation of the state of the soil, in which a zero (or negative) value indicates the soil has liquefied, and a value of one indicates the soil behaves completely plastic. Equation A.4 presents the formula used to determine the consistency index.

$$I_c = \frac{L_l - W_{g,i}}{I_p} \tag{A.4}$$

In which:

- I_c is the (nondimensional) consistency index
- $W_{g,i}$ is the gravimetric water content in situ

Using the water contents as given in Table A.1 and the Atterberg limits presented in Table A.5, this results in the consistency indices for each of the materials on the test sections shown in Table A.6.

Table A.6: Overview of resulting Atterberg limits

Material	**Liquid limit** [m%]	**Water content**[m%]	**Plasticity index**[m%]	**Consistency index**
Lean clay	28	31	8	−0.375
Silt	23	19	5	0.8

A.4.5. Conclusion

The lean clay can be categorised as a medium-plastic clay, whereas the silt only has a low plasticity. Due to the precipitation, the some sections of the clay had already liquefied, resulting in the negative averaged value of the consistency index. The samples showed a variation in consistency index between (0.125) and (−0.625), indicating that the entire surface of the section was quite close to liquefaction. As the samples were all taken a depths smaller than 0.3 metres (the thickness of the cover) and rain was frequent before and during the overflow tests, this corresponds well to visual observations and the expected state of the slope.

A.5. Permeability tests

To assess whether the influence of seepage is significant for the dike sections, the hydraulic conductivity is measured.

A.5.1. Samples and setup

A total of five samples has been tested in a falling head setup. Two samples contained undisturbed silt, two samples contained undisturbed clay and the final sample was a reconstructed sand sample at in situ porosity. All samples have been tested in a falling head test. Two reconstructed sand samples at a low and a high density (corresponding to the densities used in the shear tests) were tested using a constant head method. The water used during the test was demineralised, which is likely to result in an overestimation of the hydraulic conductivity, as the absence of minerals in the water reduces binding effects of the mineral content of the clay, allowing water to flow through the soil more easily.

A.5.2. Test procedure

All samples were saturated, placed between two fine filter plates, and placed in the falling head test setup, after which the water column was opened and the falling head was monitored by the computer. The test was performed multiple times per sample, to assess the magnitude of measurement errors, and the K_{sat} values from each material were determined. As no ISO regulations or British Standards for this test procedure have been developed, the test is conducted following general accepted practice as described in the operation manual of the test setup."UM (2012)

A.5.3. Results and observations

The resulting K_{sat} values for each sample are presented in Table A.7. The samples locations, number of test on this specific sample and the resulting hydraulic conductivity are given for each test, as well as an averaged value for each material.

Table A.7: Permeability test results

Sample	**Test No.**	K_{sat} $[m/s]$
L3	1	$2.19 * 10^{-6}$
L3	2	$1.69 * 10^{-6}$
L3	3	$1.72 * 10^{-6}$
L4	1	$3.63 * 10^{-5}$
L4	2	$3.71 * 10^{-5}$
L4	3	$3.71 * 10^{-5}$
C3	1	$1.88 * 10^{-5}$
C3	2	$2.05 * 10^{-5}$
C4	1	$3.24 * 10^{-5}$
C4	2	$2.23 * 10^{-5}$
Sr	1	$4.84 * 10^{-5}$
Sr	2	$5.04 * 10^{-5}$
Sr	3	$5.26 * 10^{-5}$
Sand	Average	$5.05 * 10^{-5}$
Silt	Average	$1.87 * 10^{-6}$
Lean clay	Average	$2.35 * 10^{-5}$

The results show some unexpected variation. The hydraulic conductivity of fine sand is often in the order of

$10^{-5}ms^{-1}$, which corresponds well to the test results. However, the values for the silt and lean clay samples range from $10^{-6}ms^{-1}$ to $10^{-5}ms^{-1}$ as well, where one would expect these values to lie at 10^{-7} and 10^{-10} or even lower. For modelling, the rule of thumb values are assumed correct.

A.5.4. Analysis

After the tests were completed, the samples were dried, removed from the rings in which they were tested and studied to find the cause of the large observed permeabilities. No irregularities were observed in the sand samples, which was to be expected, as these samples had been reconstructed from oven dried sand. In sample L3, some vertical (flow-parallel) cracks were observed, however, none of these ran through the full length of the sample. As the permeability of a sample is strongly increased if a preferential path can be distinguished, it is likely the actual permeability of the soil is somewhat lower than the observed value. More severe disturbances were observed in samples L4, C3 and C4. These samples contained some course material, with a diameter of up to 20 mm, around which various preferential paths had formed, severely increasing the permeability of the sample.

The permeability of all soils was observed to be in the order of 10^{-5}, however, in the cohesive samples, the presence of coarse material and the influence of the remolding process severely increased the permeabilities. Based on the empirical relation posed by Hazen, the permeability (in cm/s) can be estimated through equation A.5.

$$K_{sat} = C \cdot D_{10}^2 \tag{A.5}$$

Assuming the mean used value of C of 1.0, the theoretical hydraulic conductivity of the lean clay should be $5.5 * 10^{-6}$ and the theoretical hydraulic conductivity of the silt should be $4.2 * 10^{-7}$, neglecting the water-binding effects of the clay, which would reduce the permeability even further.

A.5.5. Conclusion

The observed permeability of the sand is assumed correct and representative for dense sand, as the tested sample had a porosity of 0.41. The observed permeabilities of the lean clay and silt are overestimated, due to the disturbances of the sample.

A.6. Direct Shear Tests

A direct shear test (DS) was conducted to determine the friction angle ϕ and cohesion C' of each soil. The soil was initially assumed to be spatially uniform, allowing for the use of multiple samples on different locations for the determination of the parameters. The tests were conducted following British standard BS 1377: part 7 1990.

A.6.1. Samples

A total of 16 shear tests were performed. Four undisturbed samples of each of the in-situ state soil were tested (lean clay, silt and sand) and one series of remolded, densified sand were tested under varying vertical stresses. All samples were circular and had a diameter of 63 mm. The samples were taken from different locations on the dike. Figure A.12 shows two samples used in the shear tests.

(a) Sand sample before shear testing

(b) Silt sample before shear testing

Figure A.12: Mohr-coulomb failure envelopes of all soil samples

A.6.2. Test procedure

In preparation of each test, a soil sample was cut from the container, disturbing the soil state as little as possible. No rubble material ($d > 10$ mm) was allowed in the samples, as this would cause the shear planes and thus the surface area contributing to the shear strength to vary.

The soil samples were placed between filter plates in the shear box setup, after which the box was sealed and submerged with demineralised water, to represent a high ground water table in a dike. The shear plane of the sample was below the water surface for all tests.

The samples were then consolidated under vertical loads ranging from 5 to 50 kPa, to represent the in-situ compression at a depth of approximately 0.25 to 2.5 meters below the surface of the landside slope of the dike. To ensure comparable sets of measurements were taken, consolidation times and shear strain rates were fixed for each type of sample. Consolidation times were chosen in accordance with British standard BS 1377: part 7 1990, allowing only negligible compression after starting the test. As the high-speed shearing of soil during headcut erosion is an undrained process, the shear strain rates were set high to minimise the effect of drainage on the pore strength. Strain rates and consolidation times per sample set are presented in Table A.8.

Table A.8: Test parameters direct shear tests

Sample set	**Shear strain rate** $[mm/min]$	**Consolidation time** $[h]$
Lean clay	0.25	12
Silt	0.25	2
Sand	1.2	0.25
Sand (densified)	1.2	0.25

When failure of the sample was observed, the shear stress on the sample at failure was calculated from the shear force through equation A.6 and plotted for each sample.

$$\tau = \frac{F_{shear}(t)}{A_{shear}(t)} \tag{A.6}$$

Both the shear force $F(t)_{shear}$ and the surface of the shear plane $A(t)_{shear}$ are time-dependant. For the force, the time dependant follows from the imposed strain on the soil, resulting in an increasing resisting force mobilised by the soil. The surface of the shear plane decreases monotonically, due to the displacement of the top half of the sample. The remaining shear surface after a displacement dx of the top half of the sample is visualised in Figure A.13.

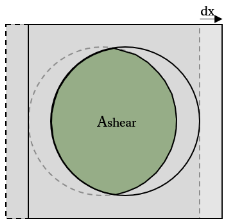

Figure A.13: Shear surface of a strained sample

A.6.3. Results and observations

Figure A.14 shows the resulting maximum shear strength for each of the samples, plotted against the vertical stress.

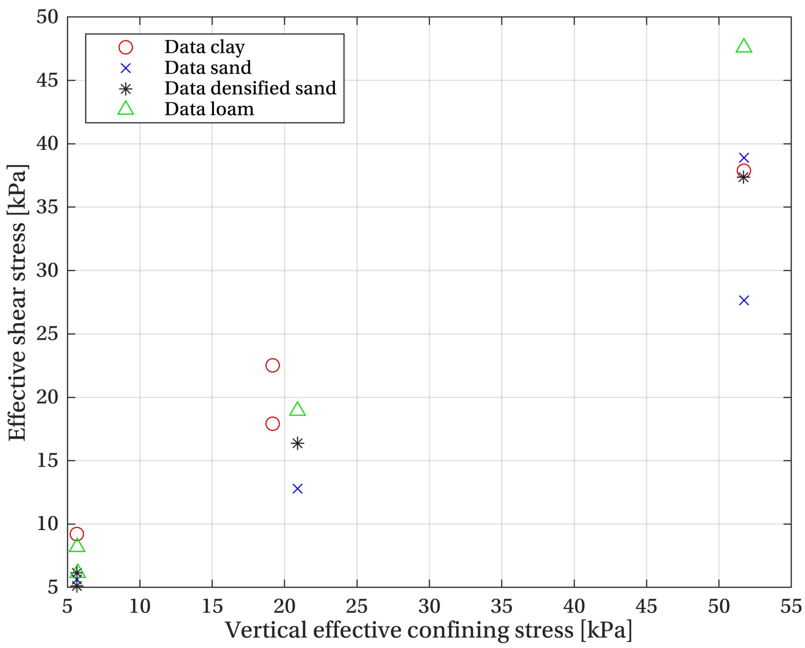

Figure A.14: Results direct shear tests

The following graphs show the observed best-fit estimates of the Mohr-Coulomb failure envelope for the different materials.

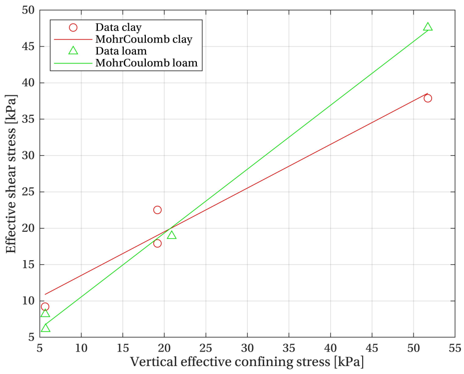

(a) Lean clay and Silt DSS results

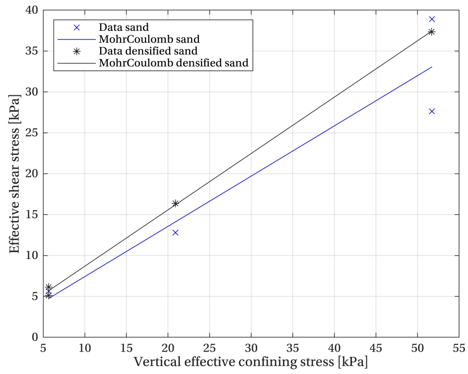

(b) Sand and densified sand DSS results

Figure A.15: Mohr-coulomb failure envelopes of all soil samples

A.6.4. Analysis

After testing the samples, all samples were dried, their volumetric water contents were determined, and the cohesion and internal friction angle of each soil type was determined. Table A.9 shows the resulting strength parameters for each sample and indicates the range of water contents of the samples.

Table A.9: Soil strength parameters

Sample set	**Friction angle** [°]	**Cohesion** [kPa]	**Volumetric water content** [%]
Lean clay	31.0	7.5	53 – 63
Silt	41.3	1.8	35 – 48
Sand	31.6	1.3	48 – 53
Sand (densified)	34.6	1.8	42 – 45

Cohesive samples

The variation in water content after performing the tests was significantly larger for the cohesive samples than for the non-cohesive samples. No clear relation between the water content and the shear strength was observed from the results of the lean clay shear tests: a higher water content does not necessarily lead to a higher or lower shear strength. As the water content for all lean clay samples was above the liquid limit (see Section A.4), this was to be expected. The liquid limit indicates the minimum water content at which the soil starts to exhibit liquid behaviour. It is clear that due to the small increase of the water content above the liquid limit, the soil does not yet completely behave as a liquid, as it is still able to sustain shear stress.

The water contents of the silt samples range from just under the liquid limit to just above the plastic limit. Therefore, the silt samples were expected to show more variation in maximum shear stress, as the behaviour of the sample tested at 20 kPa and one of the samples tested at 5 kPa (confining pressure) was expected to be liquid, whereas the other two samples were expected to behave more plastic. The effect seems to show a little in Figure A.15a: the samples with a higher water content and thus liquid behaviour show a somewhat smaller shear strength, whereas the samples with a lower water content show a higher shear strength. This effect is rather small (1 – 2 kPa variation in shear strength) and due to the small number of tests, not significantly clear to establish a relation.

Non-cohesive samples

The parameters found for loosely packed sand were corrected by excluding one of the test at 50 kPa. This sample showed a remarkable increase in shear strength, compared to the other loose sand samples. The strength even exceeded the shear strength of densely packed sand. After drying and breaking the tested sample, the reason for this became clear: various pieces of rubble ($D \sim 10 - 20mm$) were found on the shear plane of the sample, resulting in an additional surface area where shear stresses can be sustained, increasing the strength of the sample by over 50 %.

The removal of this sample from the tests results in a relatively small friction angle and a large cohesion. The observed cohesion is expected to be overestimated, due to measurement error. Some cohesion was expected due to the small fraction of mineral and organic content as reported during inspection of the material. For calculation, equal cohesion as measured in the dense sand samples is assumed. Co. (2018).

The effect of the packing is significant. When remolded into a dense packing, the friction angle of the sand increased significantly, to approximately 43 degrees. For both the dense and loose sand samples, it is expected that the shear tests have not been successfully conducted in undrained conditions, as the high permeability of the sand resulted in pore pressure dissipation at the set shear strain rate.

(Un)drained behaviour

The behaviour of the soil during the direct shear tests is strongly affected by whether the load is applied in a drained or undrained manner. Bisschop and van Kesteren (1994) define a parameter ξ, analogous to the Péclet number for heat diffusion, which describes how much, if any, pore water transport occurs during loading, in this case shearing, of the soil. For $\xi > 10$, the behaviour of the soil is considered undrained, and for $\xi < 1$, the behaviour is considered drained. The parameter is determined using Equation A.7.

$$\xi = \frac{v_s l_d}{C} \tag{A.7}$$

In which:

- v_s is the velocity at which the sample is sheared in m/s
- l_d is the length of the drainage path in m (equal to half the sample height)
- C is the applicable coefficient of consolidation for the (un)loading case in m^2/s

Using the consolidation coefficients as indicated in Table 3.2 and an estimate of order 10^{-6} metres per second for sand (Vermeulen, 2001); a drainage path length of 1.04 centimetres and shear velocities of $4.2 \cdot 10^{-6}$ metres per second (cohesive samples) and $2.0 \cdot 10^{-5}$ meters per second (non-cohesive samples), the values for parameter ξ are as displayed in Table A.10.

Table A.10: Drainage parameters shear tests

Test material	ξ	**Loading type**
Lean Clay	0.87	Drained
Silt	0.12	Drained
Fine sand (dense)	0.21	Drained
Fine sand (in-situ state)	0.21	Drained

A.6.5. Conclusion

The soil strength parameters were successfully determined for all three soil samples in drained loading conditions. An attempt was made to model the undrained behaviour of the cohesive samples, but due to the relatively small sample sizes and limited shear rate; the ξ remained smaller than one, indicating drained loading.

The presence of fine particles resulted in a significant cohesion of the lean clay samples, but barely affected the shear strength of the silt and sand, as the fraction of fines was too small.

The friction angle (ϕ) of the sand increased by approximately 9.6% by compaction (reducing the porosity by 12%). Normally, compaction of the sand would result in a decrease in cohesion. In this case, a small increase of the cohesion was observed, most likely caused by the fact that the densified samples were reconstructed from oven-dry sand, with a water content far below the optimum moisture content, whereas the in-situ state water content was above the optimum moisture content. The inflow of water at low moisture content lower (for the densified sand) resulted in a small inward pressure gradient and some additional shear resistance, appearing as a cohesive effect.

A.7. Consolidation tests

A total of four consolidation tests were performed on two silt and two lean clay samples. The procedure followed was in accordance with British standards BS 1377: Part 5: 1990.

A.7.1. Samples and setup

Two lean clay and two silt samples, taken from sample locations C1, C3, L1 and L3 were used during the consolidation tests. Each sample was submerged in demineralised water and installed in an oedometer. Three loading steps, each with a duration of 24 hours were performed, during which loads of 0.5, 1.0 and 0.5 meters of lean clay overburden (9,18,9 kPa) were simulated, to represent the consolidation of a lean clay cover on a dike.

A.7.2. Test procedure

The consolidation tests were performed in accordance with British Standards BS 1377: Part 5: 1990.

A.7.3. Results and observations

Using the log-time method, the one-dimensional consolidation coefficient C_v was determined for each of the samples. An overview of the observed consolidation coefficients for each of the samples through the two loading and a final unloading step is given in Table A.11. For each sample, the initial and final volumetric water contents (W_c) are given. As the values are measured per sample, they are only given in the first test of the sample

Table A.11: Coefficients of consolidation

Sample	**Stage**	$\overline{sigma}$ **[kPa]**	C_v [$\cdot 10^{-4} cm^2/s$]	W_c **pre-test** [-]	W_c **post-test** [-]
C1	1	9.0	4.6	0.48	0.68
C1	2	18.0	3.5		
C1	3	9.0	72		
C3	1	8.6	7.6	0.47	0.66
C3	2	17.2	4.1		
C3	3	8.6	83		
L1	1	9.0	54	0.29	0.38
L1	2	18.0	265		
L1	3	9.0	177		
L3	1	8.6	153	0.25	0.35
L3	2	17.4	212		
L3	3	8.6	179		

A.7.4. Analysis

The resulting coefficients of consolidation of the oedometer tests show some variation between the samples. Table A.12 shows the ratios of the determined C_v values between the samples of the same material.

Table A.12: Coefficients of consolidation

Sample ratio	**Stage**	**Ratio** C_v/C_v [-]
C1/C3	1	0.60
C1/C3	2	0.84
C1/C3	3	0.87
L1/L3	1	0.35
L1/L3	2	1.25
L1/L3	3	0.99

The soil samples were not completely saturated at the start of the test, which can be seen by the increase in water content during the tests. As the porosity of the sample decreases during compression, the water content would drop if samples were saturated.

The largest difference in C_v is observed between samples L1 and L3. This is most likely the result of the significant water content difference. The lower water content in sample L3 results in a higher C_v, as the air flows out of the pores easier than the water, and the air is also able to compress, whereas water is not. All other ratios between the samples are relatively close to 1.0. The variations here are expected to be caused by the spatial variability of the materials and small disturbances caused by the remoulding of the sample.

The variation in water content between the samples has two causes. Either the in situ water content varies spatially, or the water content varies in the samples due to downward water seepage during storage. It is most likely that, due to the long duration of storage of the samples (approximately two months), the higher permeability of the silt samples allowed the water to collect in the bottom of the sample. As sample L3 was taken from the highest section of the sample and sample L1 was taken from the lowest section of the sample, water contents and thus consolidation behaviour varied. The same effect can be observed for the lean clay samples. Due to the low permeability, the effect is somewhat less significant here.

A.7.5. Conclusion

The coefficient of consolidation is known to differ between loading and unloading conditions. The averaged value of the first two phases is used as the C_v for initial loading, and the average value of the final unloading stage is used as the C_{ur}, applicable to unloading and reloading. The resulting values are given in Table A.13.

Table A.13: Coefficients of consolidation

Material	C_v [$\cdot 10^{-4} cm^2/s$]	$C_u r$ [$\cdot 10^{-4} cm^2/s$]
Lean clay	5.0	78
Silt	171	178

B

Appendix B - Application of IDM-related engineering methods

The Breach Resistance Assessment Model proposed in this research was developed "to quantitatively assess dike breach formation and to determine the relevance to flood risk mitigation", as stated in Section 1.5. This Appendix describes the design process and highlights the Integral Design and Management (IDM) methods applied, in partial fulfilment of the IDM-annotation. This annotation is meant to combine technical knowledge with engineering management skills, to prepare students for roles in multidisciplinary projects.

One of the IDM-methods taught as part of the IDM-programme at Delft University of Technology is Systems Engineering (SE). SE is applied to analyse, design and develop systems and select applicable systems to an engineering problem based on the following criteria: the level of risk in the solution, fulfilment of user operational needs and life cycle costs (Wasson, 2016). The breach Model is used for scenario analysis of complex multidisciplinary processes (involving both hydraulics and geotechnical processes) and serves to find an optimal dike design, making SE a suitable method.

The Model development process in this research project can be summarised in four steps. First, the objective of the research was based on a performance gap analysis of the existing breach formation Models, identifying their deficiencies and the requirements of Dutch Water Boards. Second, a set of viable equations was verified trough analysis and testing against data from physical tests and third, the Model sensitivity was used to find design parameters for which the user operational needs were optimised. Final, a preliminary validation of the Model as a whole was performed (Wasson, 2016). Section B.1 describes the results from each of these four steps.

B.1. System development

The state-of-the-art description in Sections 2.3 and 2.4 identified the deficiencies of existing breach Models: Many existing Models apply oversimplified empirical equations and no Model describes the entire headcut erosion process, assumed in this research to be the main cause of breach formation. These Models therefore are unsuitable for sensitivity analysis or design of a breach-resistant dike, as the empirical relations incorrectly represent or omit the effects of varying design parameters.

From an analysis of alternatives, the Model phasing in the breach formation Model by d'Eliso (2007) was adopted, as this phasing described the process as a sequential failure of the grass and clay cover, followed by the headcut erosion process, as described in Section 2.2. Once breach formation is complete (a breach has formed over the complete height of the dike) the breach attracts a large flow rate, resulting in lateral growth of the breach. This process-based description of dike breaching made it possible to express the strength of each layer as a time-to-failure in scenario analysis (varying the cross-sectional composition of the dike and the bosom water level). Most other Models lack this possibility, as the failure of dike components is not considered separately.

The Breach Resistance Assessment Model addresses headcut erosion (identified as the critical technical issue) in this research, applying a process-oriented set of equations. All parameters used in the Model can be directly determined from lab tests on the construction material of the dike. This makes the Model suitable for sensitivity analysis and designing breach-resistant dikes for predefined loads, as opposed to existing Models. These loads include water level variations and overflow rates, such as typically used for peak river discharges and storm conditions. The verification and validation of the final Model is discussed in Section B.2

B.2. System and Model Verification and Validation

Model verification of the Breach Resistance Assessment Model was performed through continuous evaluation of the research questions posed in Section 1.5. A selection of existing equations was made, based on the compliance of their theoretical basis with the situation Modelled in the breach formation process. From the analysis of the existing equations (see Chapter 4), the exact mathematical formulation of the Breach Resistance Analysis Model was derived. The description of the breaching process as a sequence of sub-Models made it possible to validate each Model phase separately, as well as validate the Model as a whole (as in common SE-practice).

This preliminary selection of equations was validated against the data of physical tests, to assess whether the phases chosen in the Model represent the physical processes. The applied method of full Model validation is limited, as no physical tests on the complete breach formation process have ever been performed. The data against which the Model was checked thus only represents the phases in the breach formation process separately, proving the applicability of the applied equations, but leaving the assumptions regarding phase transitions (now assumed to be instantaneous) untested.

B.2.1. System testing

The performance of the system as a whole was validated in three case analyses. This lead to a conclusion on the applicability of the Model, and recommendations on breach-resistant dike design based on similarity with the only comparable Model, posed by d'Eliso (2007).

As no large-scale breach formation test has ever been performed, the testing is based on hypothetical cases. It is recommended that a large-scale breach formation test, comprising a dike with all Modelled layers (grass and clay cover and sand core) is performed to validate the Model as a whole. The case studies in this research showed times-to-failure for the Model to be similar to those found by d'Eliso (2007): ranging from a few hours up to a day, although the time-to-failure of the grass cover is estimated far higher by d'Eliso (2007), whereas the proposed Model finds a larger time-to-failure for the clay cover and sand core (eroded through the headcut erosion process).

Finally, a sensitivity analysis of the dike breaching process was performed, to find the most influential parameters of the breach formation process. Section 4.7.3 showed that the steepness of the landside slope, the thickness and quality of the clay cover and the porosity of the core material have the most significant influence on the time-to-failure of the dike. A high grass cover quality can also significantly increase the time-to-failure of the dike, but is extremely difficult to guarantee, as the natural spatial variability always leads to weaker spots. Two conclusions can be drawn from these results: natural variability of these parameters poses an additional risk of dike breaching, compared to design values, but these parameters can also be used in designing a breach-resistant or breach-retardant dike. Variation of parameters resulted in the following design conclusion:

A dike with a clay layer of 1.0 to 1.5 metres thick, constructed in EC2 (or EC1) class clay, with a slope steepness of 1 : 4 results in slow headcut formation, significantly delaying and in most cases preventing dike breach formation (for tested overflow rates of 100 l/m/s) due to overflow in storms (with a typical duration up to 24 hours). Breaching cannot be prevented by these measures if the overflow is a result of a river discharge peak, which typically last for days.

B.3. Reflection on the application of IDM-methods

The application of Systems Engineering to the development of a dike breach Model made it possible to structure the breaching process into various phases and to find the relevance of different design parameters of a dike. The separation of the Model into phases significantly reduces the complexity of the Model, as a dominant hydraulic load and geotechnical failure mechanism is selected for each phase. After verification of each of the phases, the entire Model was validated as a whole. The design process follows a coarse-to-fine approach, with verification on different levels of detail and validation of the Model as a whole.

The case studies showed the relative importance of each phase, by assigning a time-to-failure to each layer of the dike. However, the definition of a start and stop criterion for each phase in the breaching scenario also leads to assumptions, most notably: the assumption of instantaneous phase transitions. Assuming instant transitions between failure of the grass cover and erosion of the clay layer results in an underestimation of the time-to-failure, as in practice, these transitions are not instant.

In conclusion, the application of Systems Engineering to develop a dike breach Model allows for better sensitivity analysis, enabling users of the Model to adapt dike design to improve breach resistance. The assumption of sequential failure of the dike components leads to an estimate of the minimum time-to-failure, as the scenario phasing assumes the complex phase transitions to be instantaneous, where in reality, these are more gradual.